AFRL-RX-WP-TR-2020-0110

ADVANCED MATERIAL CHARACTERIZATION & STRUCTURAL CERTIFICATION - (AMCSC)

Volume 2 of 2

K.H. Hoos and H.K. Adluru
University of Texas at Arlington Research Institute

B. Van der Vossen, A.V Makeev, and E.V. Iarve
University of Texas at Arlington, Mechanical and Aerospace Engineering,

Wichita State University, Office of Research and Sponsored Programs

17 December 2020
Final Report

AIR FORCE RESEARCH LABORATORY
MATERIALS AND MANUFACTURING DIRECTORATE
WRIGHT-PATTERSON AIR FORCE BASE, OH 45433-7750
AIR FORCE MATERIEL COMMAND
UNITED STATES AIR FORCE

NOTICE AND SIGNATURE PAGE

Using Government drawings, specifications, or other data included in this document for any purpose other than Government procurement does not in any way obligate the U.S. Government. The fact that the Government formulated or supplied the drawings, specifications, or other data does not license the holder or any other person or corporation; or convey any rights or permission to manufacture, use, or sell any patented invention that may relate to them.

This report is the result of contracted fundamental research deemed exempt from public affairs security and policy review in accordance with SAF/AQR memorandum dated 10 Dec 08 and AFRL/CA policy clarification memorandum dated 16 Jan 09. This report is available to the general public, including foreign nationals.

Copies may be obtained from the Defense Technical Information Center (DTIC) (http://discover.dtic.mil).

AFRL-RX-WP-TR-2020-0110 HAS BEEN REVIEWED AND IS APPROVED FOR PUBLICATION IN ACCORDANCE WITH ASSIGNED DISTRIBUTION STATEMENT.

MOLLENHAUER.DAVID.H.1230181590
Digitally signed by MOLLENHAUER.DAVID.H.1230181590
Date: 2021.05.21 13:04:59 -04'00'

DAVID MOLLENHAUER
Program Manager
Composites Branch
Structural Materials Division
Materials and Manufacturing Directorate

ROGERS.BRET.ZACHARY.1265647924
Digitally signed by ROGERS.BRET.ZACHARY.1265647924
Date: 2021.05.21 17:56:52 -04'00'

BRET ROGERS
Section Chief
Composites Branch
Structural Materials Division
Materials and Manufacturing Directorate

This report is published in the interest of scientific and technical information exchange and its publication does not constitute the Government's approval or disapproval of its ideas or findings

NOTICE AND SIGNATURE PAGE

Using Government drawings, specifications, or other data included in this document for any purpose other than Government procurement does not in any way obligate the U.S. Government. The fact that the Government formulated or supplied the drawings, specifications, or other data does not license the holder or any other person or corporation; or convey any rights or permission to manufacture, use, or sell any patented invention that may relate to them.

This report is the result of contracted fundamental research deemed exempt from public affairs security and policy review in accordance with SAF/AQR memorandum dated 10 Dec 08 and AFRL/CA policy clarification memorandum dated 16 Jan 09. This report is available to the general public, including foreign nationals.

Copies may be obtained from the Defense Technical Information Center (DTIC) (http://discover.dtic.mil).

AFRL-RX-WP-TR-2017-0110 HAS BEEN REVIEWED AND IS APPROVED FOR PUBLICATION IN ACCORDANCE WITH ASSIGNED DISTRIBUTION STATEMENT.

//Signature//	//Signature//
DAVID MOLLENHAUER	BRET ROGERS
Program Manager	Section Chief
Composites Branch	Composites Branch
Structural Materials Division	Structural Materials Division
Materials and Manufacturing Directorate	Materials and Manufacturing Directorate

This report is published in the interest of scientific and technical information exchange and its publication does not constitute the Government's approval or disapproval of its ideas or findings

REPORT DOCUMENTATION PAGE

Form Approved
OMB No. 0704-0188

1. REPORT DATE *(DD-MM-YY)*	2. REPORT TYPE	3. DATES COVERED *(From - To)*
17 December 2020	Final	23 January 2018 – 17 November 2020

4. TITLE AND SUBTITLE
Advanced Material Characterization & Structural Certification - (AMCSC)
Volume 2 of 2

5a. CONTRACT NUMBER
FA8650-18-C-5289

5b. GRANT NUMBER

5c. PROGRAM ELEMENT NUMBER
62102F

6. AUTHOR(S)
K.H. Hoos and H.K. Adluru, Univ of Texas at Arlington Research Institute
B. Van der Vossen, A.V Makeev, andE.V. Iarve – Univ. Of Texas at Alrington, Mechanical & Aerospace Engineering

5d. PROJECT NUMBER
4347

5e. TASK NUMBER

5f. WORK UNIT NUMBER
X1EJ

7. PERFORMING ORGANIZATION NAME(S) AND ADDRESS(ES)
University of Texas at Arlington
Office Of Research Administration
400 S Corn St
Arlington, TX 76019-0001

8. PERFORMING ORGANIZATION REPORT NUMBER

9. SPONSORING/MONITORING AGENCY NAME(S) AND ADDRESS(ES)
Air Force Research Laboratory
Materials and Manufacturing Directorate
Wright Patterson Air Force Base, OH 45433-7750
Air Force Materiel Command
United States Air Force

10. SPONSORING/MONITORING AGENCY ACRONYM(S)
AFRL/RXCC

11. SPONSORING/MONITORING AGENCY REPORT NUMBER(S)
AFRL-RX-WP-TR-2020-0110

12. DISTRIBUTION/AVAILABILITY STATEMENT
DISTRIBUTION STATEMENT A. Approved for public release: distribution is unlimited.

13. SUPPLEMENTARY NOTES
This is Volume 2 of 2. Report contains color.

14. ABSTRACT ***(Maximum 200 words)***

Regularized Extended Finite Element Methodology (Rx- FEM), is currently implemented in the BSAM software including the framework required for geometrically nonlinear analysis. The input data requirements for Discrete Damage Modeling (DDM) including the fatigue material characteristics for DDM models in this work have been addressed at the University of Texas Arlington Advanced Materials and Structures Lab (AMSL). Namely, experimental apparatus was designed, manufactured and applied to transverse and in-plane shear S-N curve determination in fully revisable fatigue R=-1 regime as well as measurement of delamination growth rate at R=-1. BSAM was extended for progressive failure analysis with spatially random strength and fracture properties The stochastic property distributions lead to realistic strength prediction and appear to account for the volume scaling of strength.. Kink band formation and effective fiber direction fracture toughness were investigated. A 4 point bend (4PB) test of notched unidirectional composite was utilized by AMLS. The test underwent significant evolution during the resulting in a 2ply thick specimen with Plexiglas unbuckling guides designed by AMLS. These 4PB specimens were simulated by using BSAM. It was found that the best correlation with experiment in terms of failure loads and kink band formation was obtained by using geometrically nonlinear formulation with the nonlinear shear properties independently characterized by AMLS. This finding was counter to initial expectation of using continuum damage mechanics (CDM) approach, which had difficulty in failure localization within realistic range of material property values.

15. SUBJECT TERMS
Fatigue of composites, X-ray CT inspections, Finite element, Stochastic properties, Crack modeling

16. SECURITY CLASSIFICATION OF:			17. LIMITATION OF ABSTRACT:	18. NUMBER OF PAGES	19a. NAME OF RESPONSIBLE PERSON (Monitor)
a. REPORT	b. ABSTRACT	c. THIS PAGE			David Mollenhauer
Unclassified	Unclassified	Unclassified	SAR	93	19b. TELEPHONE NUMBER *(Include Area Code)* (937) 904-4394

TABLE OF CONTENTS

Section **Page**

LIST OF FIGURES

LIST OF TABLES

Table **Page**

Summary

This is Volume 2 of 2.

The proposed Discrete Damage Modeling (DDM) technology is based on Regularized Extended Finite Element Methodology (Rx- FEM), which is currently implemented in the BSAM software including the framework required for geometrically nonlinear analysis. Verification and validation (V&V) exercises were performed on various failure modes and laminate configurations including static and fatigue loading. While the static framework showed a significant degree of maturity, the fatigue capabilities were further developed by including constitutive models for variable load ratio R and arbitrary block loading. While basic models for predicting complex fatigue behavior are now in place, the validity of the assumptions, which are made to account for variation of fatigue regimes require further experimental validation. The input data requirements for Discrete Damage Modeling (DDM) including the fatigue material characteristics for DDM models in this work have been addressed at the University of Texas Arlington Advanced Materials and Structures Lab (AMSL). Namely, experimental apparatus was designed, manufactured and applied to transverse and in-plane shear S-N curve determination in fully revisable fatigue R=-1 regime as well as measurement of delamination growth rate at R=-1. In both cases the measured data does not fall on the trend lines predicted by common approaches.

Significant amount of work was devoted to measurement and characterization of variation of basic stiffness and strength properties of tape composites, and in-situ transverse tensile strength in particular. While the mechanism and interplay of strength controlled initiation and fracture mechanics controlled propagation as a function of ply thickness are well understood, these concepts have not been applied to progressive damage analysis (PDA) within the DDM framework by using spatially random strength and fracture properties. Recently performed studies by the authors of failure initiation and propagation in Clamped Tapered Beam (CTB) specimens showed good agreement with experimental data in terms of failure location and average failure loads in the matrix dominated failure regime. In the present project stochastic distribution of fiber direction strength was introduces in the PDA and previous experimental data on open hole strength revisited. The stochastic property distributions lead to realistic strength prediction and appear to account for the volume scaling of strength.

While the stochastic strength property distribution addresses the initiation controlled failure phenomena an additional set of properties is required for realistic PDA in the propagation regime. Namely the kink band formation and effective fiber direction fracture toughness were investigated in the present project. A 4 point bend (4PB) test of notched unidirectional composite was utilized by AMLS. The test underwent significant evolution during the study starting with 0.25 inch thick specimen suggested by literature sources and evolved into a 2ply thick specimen with Plexiglas unbuckling guides designed by AMLS. Micro-X-Ray Computed Tomography (μCT) and Digital Image Correlation (DIC) was used to characterize the kink band formation.

These 4PB specimens were then simulated using the DDM software BSAM. It was fund that the best correlation with experiment in terms of failure loads and kink band formation was obtained by using geometrically nonlinear formulation with the nonlinear shear properties independently characterized by AMLS. This finding was counter to initial expectation of using continuum damage mechanics (CDM) approach, which had difficulty in failure localization within realistic range of material property values.

1. Introduction

Laminated composite materials are used in a variety of aerospace, automotive, and sports equipment applications. In designing these parts, coupon tests are performed to determine the material properties to be used in the design. However, manufacturing and material variation cause significant strength variations within a single part in all three material directions. Significant amount of work was devoted to measurement and characterization of variation of basic stiffness and strength properties of tape composites, and in-situ transverse tensile strength in particular. The subject literature is very extensive and the reader is referred to recent experimental work [1] including references. While the mechanism and interlay of strength-controlled initiation and fracture mechanics controlled propagation as a function of ply thickness are well understood, it is pointed out that additional brittle strength scaling concepts are required to explain the entire spectrum of results.

Understanding the implications of input property variation and scaling is also critical to application of progressive damage analysis (PDA) to design and certification of composite structures. Thus recently performed simulations of failure initiation and propagation in Clamped Tapered Beam (CTB) specimens [2] showed good agreement with experimental data for ply level transverse strength parameter obtained by using 3 point bend (3PB) test method [3] whereas the results obtained by using an almost two times lower value resulting from tensile testing of 90° coupons [4] resulted in 30% underprediction of the peak load. The goal of the present work is to introduce spatial scatter of transverse strength parameters into simulations and attempt to predict the strength of all categories of coupons. i.e. 90° tension, 3PB and CTB specimens with a single set of input parameters.

The Discrete Damage Modeling (DDM) method utilizing Regularized Extended Finite Element Method (Rx-FEM)), Ref. [5], was used for simulation [6], [7]. Two aspects of this mesh independent cracking methodology are affected by random distribution of transverse strength. One is the randomization of the crack initiation location, and second is the cohesive zone methodology based propagation with nonuniform variation of release pressure. The fracture toughness in the mode I and II were not varied in the present study. The cohesive zone model response with random seeding of initiation strength was theoretically investigated first and showed that a finite physical dimension based seeding is required to reproduce the Weibull type weak link failure load scaling with the nonuniform field of initiation strength. Namely if the initiation strength is seeded based on the integration point the global behavior is not brittle.

In the present work this methodology is extended for fiber failure. The discrete damage modeling (DDM) technology based on Regularized Extended Finite Element Methodology (Rx-FEM) utilizes two methods for predicting fiber fracture in unidirectional composites: critical failure volume (CFV) and a continuum damage modeling (CDM) based progressive damage modeling approach as described [6]. The CFV technique has been shown to provide accurate predictions of macro-level fiber failure initiation, which can in-turn be used for predicting final failure in

certain circumstances. However, this method is not a progressive damage technique and is problematic when the expected failure mode is compression. The CDM approach readily models progressive damage in tensile and compressive loading, but this approach has characteristically had a diffuse failure in tension and predicts initiation at relatively low applied loads. The newly implemented stochastic seeding of CDM properties will be exercised to overcome these shortcomings.

A common difficulty in application CDM and PDA to fiber failure are the gradient properties such as effective fracture toughness required. These values describe the propagation of fiber failure and the volumetric scaling of strength. For both of these properties, experimentally-derived properties have been developed using non-standardized test methods, and these methods are far from being standardized. As part of this effort, AMSL worked to address some of these issues. To address some of the issues with the so-called fiber-direction fracture toughness, four-point bend (4PB) specimens and tests were developed and performed. Using micro-X-Ray Computed Tomography (μCT) and Digital Image Correlation (DIC), AMSL attempted to characterize fiber failure on the ply-level. These 4PB specimens were then simulated using the DDM software BSAM by researchers.

The fatigue simulation within DDM framework and Rx-FEM formulation has been demonstrated in Ref. [8], [9]. While the kinematic Rx-FEM framework requires no modification the constitutive relationships allowing for fatigue crack insertion and propagation criteria were developed. The proposed methodology was verified on quasi 2D examples in [8] and validated on open hole tension-tension examples [9]. All of the analysis was performed under constant amplitude loading. Analytical and experimental development to extend and V&V the methodologies under spectrum loading fatigue and block loading sequences in particular was performed. The analytical development modified the current combination of the Event and Cycle based modeling approach towards cycle based approach allowing to predict the material changes under relatively small and *a priori* defined number of cycles and take into account load sequencing effects. However, the effect of load sequencing on behavior of matrix and fiber dominated modes is not thoroughly understood. The initial stages of this work are reported below and addressed fully reversible loading response of the shear failure mode as well as looked at the delamination growth rate in mode II and the reverse loading conditions. The input parameters and material characterization guidelines required for modeling were addressed at the University of Texas Arlington Advanced Materials and Structures Lab (AMSL).

The Task 1 section of the report will be organized in the order milestone sequence and will begin with overall description of the experimental work followed by fatigue analysis and related experiments. We will then describe the analysis results with stochastic variation of fiber properties and conclude with experimental and numerical results on compression kink band formation.

2. Experimental program

Recent advances in Digital Image Correlation (DIC) and Computed Tomography (CT) motivated the development and verification of material characterization methods driven by DIC and CT data to capture physics of the deformation and failure of composites. One of the strengths of AMSL has been successful development and verification of fundamental composite material characterization methods driven by DIC and CT data to capture physics of the investigated phenomena including stress-strain response, strength/fatigue and toughness material characteristics, and increase our confidence in material allowables for composites [10]–[15]. Such methods have been further developed.

Due to material heterogeneity and consideration of multiple length scales, the development of the material model and the characterization of its properties are major challenges. The measurement of some of these properties, such as linear modulus and tensile strength, are industry (ASTM) standard. However, to fully characterize the range of (non)linear responses can be cost prohibitive. Instead, some of these properties may be approximated or assumed during analysis [16]. Inaccurate input properties may lead to considerable error in prediction models, and this project aims to measure some of the material behaviors that have historically been hard to measure:

- Generating shear fatigue material properties at various load ratios
- Ply interface cohesive laws and in-situ material properties
- Input parameters governing fiber failure progression

The purpose of measuring these material properties is meaningful to address gaps in DDM input parameters. During the program, specimens from IM7/8552 carbon fiber epoxy were produced and tested to generate input parameters. Note that some tests measure bulk material behavior in shear and bending, while other tests measure fracture behavior under compression and at the ply interface. Shear strength and fracture toughness (mode II) are important for life predictions, but measurements need to include non-linear stress-strain behavior, as well as effects from the fatigue load ratio and fatigue sequencing [11]. Input parameters governing fiber failure progression also pose challenges, as fiber-compression ply cracking is a complex failure mode [17]. Lastly, cohesive laws are to be measured for use in Cohesive Zone Modeling (CZM), a powerful tool to model interface strength and damage progression [18].

The overall experimental matrix and specimen layout are described below

Table 1. Specimens for Characterization of IM7/8552 Epoxy Tape

Test	Geometry/Layup/ Orientation	Coupons IM7/8552
Short Beam Shear **Static, Fatigue** **ASTM D2344**	1.75 x 0.25 x 0.25 in. Unidirectional 1-2 Plane - Static - Fatigue R = 10 - Fatigue R = -1. 1-3 Plane - Static - Fatigue R = 10 - Fatigue R = -1.	6 9 9 6 9 9
3-Point Bend Long Beam **Static, Fatigue**	4.0 x 0.25 x 0.25 in. Unidirectional 1-2 Plane - Static - Fatigue R = 10	5 18
Notched 4-Point Bend **Static**	6.0 x 0.50 x 0.25 in. Unidirectional 1-2 Plane, notched	12
End Notch Flexure (ENF) **ASTM D7905** **Static, Fatigue**	$[0_8/3_2/\text{-}3_2/0_8]_T$, 6.4 x 1 x .15 in. - Static - Fatigue R = 10 - Fatigue R = -1.	3 4 4
Open Hole Compression with CT reconstructions **Static, Fatigue** **ASTM D6484**	$[0/90]_{2S}$ 12 x 1.5 x 0.06 in., D = 0.25 in. - Static - Fatigue R = 10	6 6

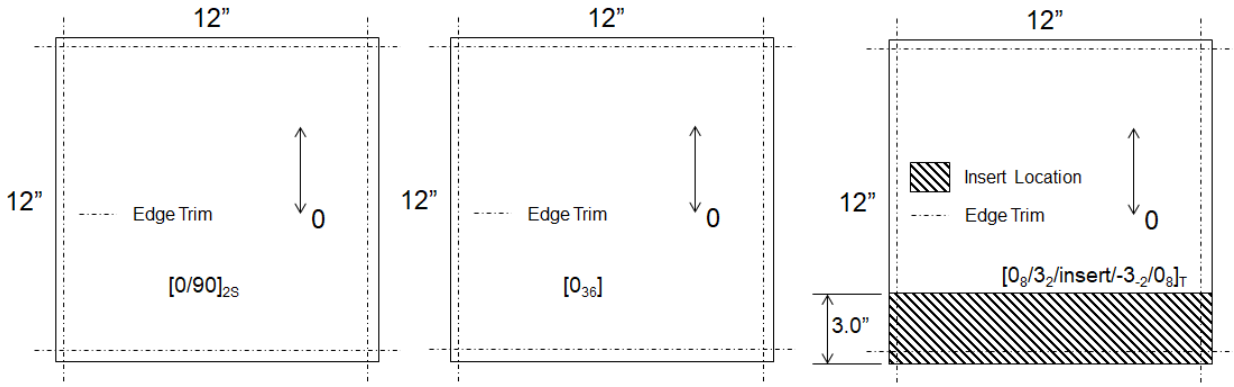

Figure 1: Composite Panels for Characterization of IM7/8552 Epoxy Tape

The material selected and tested is IM7 intermediate modulus carbon fiber in 8552 epoxy resin. The two candidate material systems discussed in July 2018 were IM7/5250-4 BMI Tape and IM7/5320-1 OOA Epoxy Tape. Available to us was only the IM7/8552 material as provided by

Bell Textron Inc. The tests and specimens chosen are shown in Table 1. Note that this report will highlight some legacy test results on Double Cantilever Beam (DCB), Thick Adherend (TA), Open Hole Compression (OHC), and Small Plate Twist (SPT) on the same material. For ASTM standards, please refer to references [19]–[24]. Basic nonlinear and fatigue properties including reversible shear fatigue for S-N characteristics/effects of the fatigue load ratio and fatigue sequencing can be measured by:

- Static uni SPT 1.5 x 1.5 x 0.25 in.
- Static, fatigue uni Short Beam Shear (SBS) D2344 1.75 x 0.25 x 0.25 in.
- Static, fatigue uni long beam 3 point bend 4 x 0.25 x 0.25 in.

Inter-Laminar Fracture Cohesive Laws may be measured by the following chosen tests

- Static, fatigue DCB ASTM D5528 $[0_{16}/3_2/\text{-}3_2/0_{16}]_T$
- Static ENF ASTM D7905 $[0_{16}/3_2/\text{-}3_2/0_{16}]_T$
- Static, fatigue TA Shear D5656 $[0_{16}/3_2/\text{-}3_2/0_{16}]_T$ 9 x 1 x 0.25 in.

Fiber compression ply cracking fracture toughness as measured by:

- Static, fatigue OHC $[0/90]_{2S}$ W 1.5 in. D 0.25 in.
- Static, fatigue OHC ASTM D6484 $[45/90/\text{-}45/0]_{3s}$ W 1.5 in. D 0.25 in.
- Static, notched four point bend test $[0]_{36}$ 0.25 x 0.5 x 6 in.

2.1. Specimens to characterize constitutive material parameters

Short Beam Shear (SBS) specimens allow for characterization of linear elastic moduli and shear nonlinear behavior of composite materials in 1-2 and 1-3 planes. Fatigue S-N curves for shear stress are to be characterized at several load ratios, including R = 10 and R = -1 (fully reversible). Data from 3-point bending of long beams is to be used to characterize compressive strength. SBS specimens have dimensions of 1.75 x 0.25 x 0.25 in.

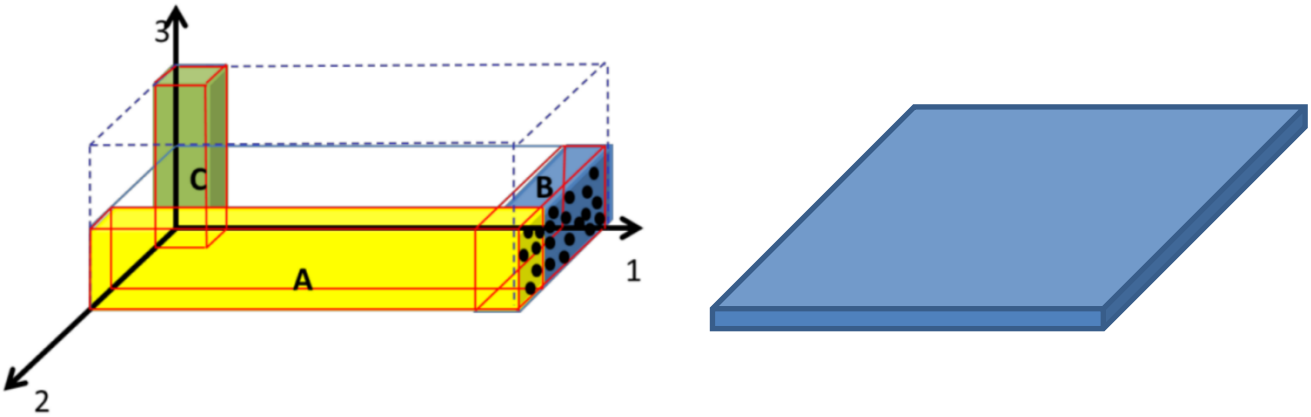

Figure 2: Left: Configurations for SBS specimens. Right: SPT Specimen

Small Plate Twist specimens are used to measure shear nonlinear curves in all three material planes in a single test. To characterize these properties, six specimens are to be tested. Unidirectional specimens are to be cut from the same panel as the SBS and long beam specimens 1.5 x 1.5 x 0.25 in.

Long beam specimens are used to capture flexural properties with higher fidelity and fail in fiber compression. Long beam specimens 4.0 x 0.25 x 0.25 in. are to be cut from the same panel as SBS specimens.

An adaptation of the long beam with a notch is used to define the fracture toughness in fiber compression. Long beam specimens are to be made 6.0 x 0.50 x 0.25 in. A notch was introduced in the specimen, with a notch radius of 125 μm or less. AMSL has taken responsibility for machining of the notch. The test is inspired by experimental work by Laffan et al [25].

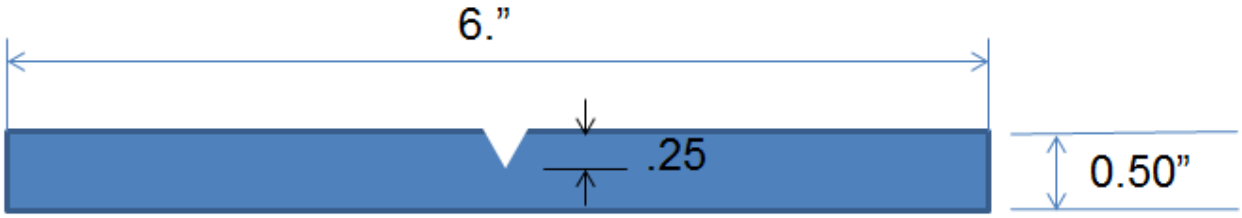

Figure 3: Long beam tested under 4-pt bending to determine energy release rate of fiber compressive failure

2.2. Specimens to characterize ILF properties

ASTM standard DCB and ENF specimens were tested to characterize mode I and mode II fracture properties. Using high-resolution DIC, the fracture toughness as well as the cohesive zone may be characterized. Specimen blocks are available and can be attached by the AMSL lab.

Thick adherend (TA) specimen is a predominantly mode II fracture specimen with stable crack growth, making this a suitable specimen for fatigue testing under mode II fracture. Special care was taken that the channels/grooves milled from the specimens are half the thickness deep, with minimal milling damage to the material in the gauge section. An undamaged ply would transmit load directly, reducing the mode II energy.

The inserts, creating a seeded crack in the DCB and ENF test specimens, according to ASTM standard, but AMSL also followed procedure to grow a natural crack before testing.

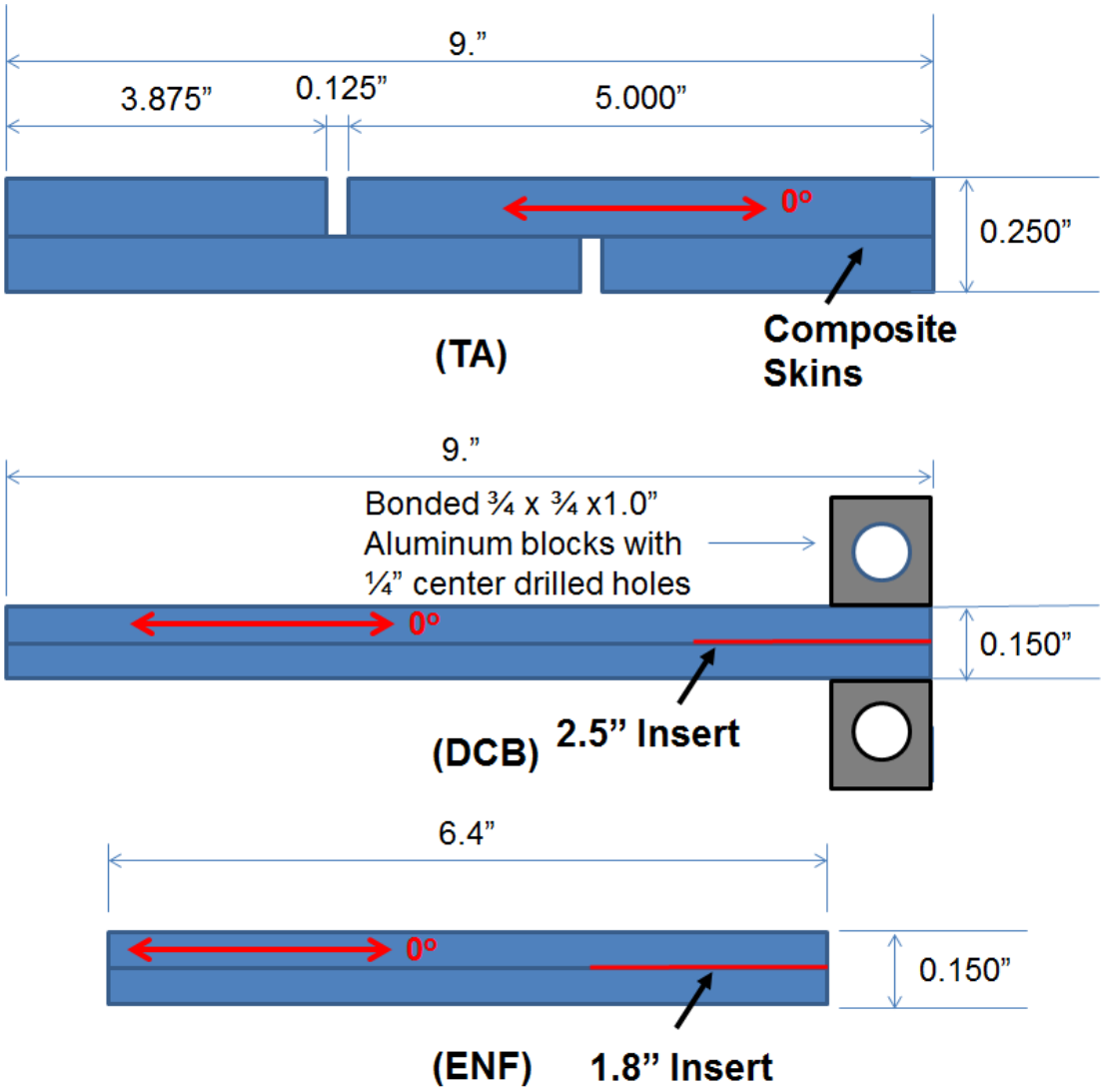

Figure 4: Fracture Specimens tested to measure ILF cohesive behavior. Red indicates manufactured pre-crack.

Open-hole compressive stress of multidirectional polymer matrix composites laminates is tested via the ASTM D6484 standard. Two laminates are chosen: $[0/90]_{2S}$, and $[45/90/-45/0]_{3s}$. Laminates are cut into specimens of 12 x 1.5 in. with hole diameter of D = 0.250 in.

A hole is drilled in the center of each specimen with diameter 0.25 in. Care was taken to minimize drilling damage of any holes in OHC specimens. At AMSL, holes are drilled with a Plexiglas backing and a milling bit. For consistency, AMSL was responsible for drilling of the holes.

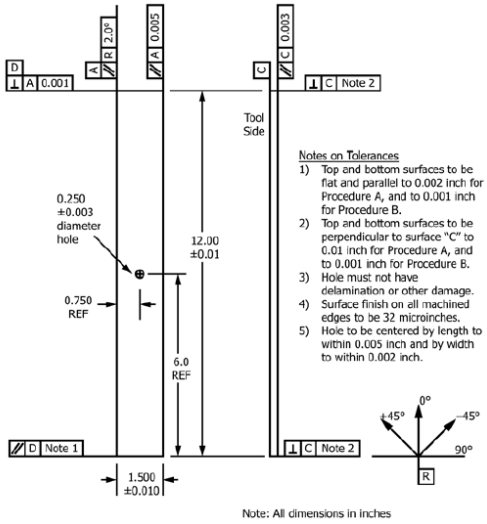

Figure 5: Geometry of OHC specimen per ASTM D6484

The results of experimental investigation will be separated in three groups. The first group will deal with basic static material property characterization and will be deferred to Appendix 1, the results of the fatigue property characterization will be described next and the fiber direction fracture toughness will be described in the last section.

3. Fatigue analysis and experimental characterization

The fatigue simulation within DDM framework and Rx-FEM formulation has been demonstrated in Ref. [8], [9]. While the kinematic Rx-FEM framework requires no modification the constitutive relationships allowing for fatigue crack insertion and propagation criteria were developed. The proposed methodology was verified on quasi 2D examples in [8] and validated on open hole tension-tension examples [9]. All of the analysis was performed under constant amplitude loading. We propose analytical and experimental development to extend and V&V the methodologies under spectrum loading fatigue and block loading sequences in particular. The analytical development will modify current combination of the Event and Cycle based modeling approach towards cycle based approach allowing to predict the material changes under relatively small and *a priori* defined number of cycles and take into account load sequencing effects.

Prior to describing the combined event and cycle based capability implemented in BSAM to address load sequencing a brief review of main relationships used for modeling fatigue response is given below.

Both the S-N curves for matrix dominated failure modes such as transfer tension and shear are required for analysis along with the propagation characterization, i.e. Paris law in the Mode I and II regimes.

Log-linear relationship is used for S-N curves is used

$$\frac{\sigma(N)}{\sigma_c} = 1 - s \log N \tag{1}$$

is used in BSAM, where *s* is a material constants and σ_c is the allowable static stress. The Paris Law in composites literature is often presented in the following form

$$\frac{da}{dN} = A_p (G_{max})^m \tag{2}$$

for both Mode I and II loading. A normalized relationship

$$\frac{da}{dN} = C \left(\frac{G_{max}}{G_c}\right)^m \tag{3}$$

is used in BSAM, where $C = A_p (G_c)^m$ and A_p, and m are material constants and and G_c is the critical value of the Energy Release Rate (ERR). Relationships (1), (2) hold for a single value of

the R ratio. In order to extend the analysis to different R ratio and rescaling of S-N parameters Goodman diagram relationship can be used analogous to Equation (6) in Ref. [26], specifies the endurance limit as

$$\sigma_{eR} = \frac{\sigma_c}{2 - R}$$

The S-N diagram is corrected further to account for the difference between axial and shear loading based on Equation (21-23) in [26] and [27]. The load correction factor for endurance limit suggested by [27] is

$$C_L = 1 - 0.42B,$$

where, B is the mode mixity equal to the ratio of Mode II energy release rate (ERR) to total ERR. For pure shear stress the endurance limit with load correction factor reduces to

$$\sigma_{eR} = 0.58 * \frac{\sigma_c}{2 - R}.$$

A 10^7 cycle count is then used to calculate revised coefficient *s* in the Eqn. (1) for required R-ratio.

Several methodologies for rescaling Paris Law coefficients were reviewed in Ref. [28]. The approach directly following the original formulation of Paris Law in the power form of the change in the crack stress intensity factor during a loading cycle is considered. The formula can be expressed in terms of the maximum and minimum values of the energy release rate (ERR) during a fatigue cycle as

$$\frac{da}{dN} = D\left(\sqrt{G_{max}} - \sqrt{G_{min}}\right)^{2m} \quad (4)$$

Introducing $R = \sqrt{G_{min}}/\sqrt{G_{max}}$ one can rewrite to

$$\frac{da}{dN} = D(1 - R)^{2m}(G_{max})^m \quad (5)$$

Comparing Eqn(4) and (2) one can readily recalculate the value of A_p in (2) for different R ratios if the coefficients A_p and m are known for a given R.

The Eqn. (1) and (2), which are used for prediction of fatigue response were originally established for monotonic cyclic loading. Their generalization application to load sequencing requires additional assumptions. It is important to recognize that while the S-N approach in the form of Eqn. (1) by itself is not applicable to account for such effects, the Paris law (2) is. Since it provides the rate of growth of crack or delamination length as a function of the loading amplitude it can be applied incrementally to calculate the total length of the latter as a function of arbitrary loading history. The key issue is the range of validity Eqn. (2) or Eqn. (4), representing the Paris law in its original form, with respect to the magnitude of $\sqrt{G_{max}} - \sqrt{G_{min}}$.

The S-N relationship Eqn. (1) on the other hand contains no information to account for any variability of the loading amplitude even if it accurately predicts the number of cycles to failure at a given load level. The common approach to overcome this difficulty is to utilize the Palmgren-Miner rule, which has been adopted in BSAM [9]. A history variable d_I was introduced such that its increment is defined as

$$\Delta d_I = \Delta N / N \tag{6}$$

where ΔN is the number of cycles the material point is seeing at a given constant amplitude σ and N – is the limit number of cycles at that load, which can be obtained from Eqn. (1). According to Palmgren-Miner rule the failure occurs when

$$d_I = \sum \Delta d_I = c \tag{7}$$

where without restriction of generality we will assume that *c=1*. This relationship significantly generalizes the S-N approach and answers a practically important question of residual strength after a certain number of cycles when $d_I < 1$. Namely, for any value of the d_I, which has been achieved, the residual strength σ_r can be defined as the load level at which the failure occurs in 1 cycle. Let the limit number of cycles at that load level be N_r then according the Palmgren-Miner rule one can write

$$d_I + \frac{1}{N_r} = 1 \tag{8}$$

The respective load level σ_r can be obtained by substituting N_r in Eqn. (1), which yields

$$\sigma_r = \sigma_c(1 + s \log(1 - d_I)) \tag{9}$$

It can be seen that if $d_I = 0$ then $\sigma_r = \sigma_c$, which is consistent with the S-N concept. An important observation is that Eqn. (9) defines a unique and monotonic relationship between the history variable d_I and residual strength σ_r. Note that the specific form of this relationship holds for the S-N curve in the form of Eqn. (1) and the linear accumulation rule (7). However, the uniqueness and monotonicity of such relationship is general and the residual strength can be used to track the history of loading, which is the approach taken in Ref. [28] and was termed "Residual Strength Tracking". Such approach is very attractive since the residual strength is a physical quantity meaningful and intuitive from the engineering stand point. The S-N curve in Eqn. (1) is only one form of such relationship and other forms, i.e. power law type

$$\frac{\sigma(N)}{\sigma_c} = A(\log N)^B$$

and other can be readily adopted. A particular relationship, which was utilized in Ref. [28] combines the damage accumulation law and S-N curve and was proposed by Sendeckyj [29]

$$\sigma_r = \sigma_c \left[\left(\frac{\sigma_r}{\sigma} \right)^{\frac{1}{S}} + (N-1)B \right]^S \tag{10}$$

Where the notations have been changed to match current notations and B and S are material parameters. If one sets $\sigma_r = \sigma$, i.e. the residual strength is equal to the load, which corresponds to the S-N curve we obtain

$$\sigma = \sigma_r = \sigma_c [1 + (N-1)B]^S, \tag{11}$$

which is the underlying power law S-N relationship. If one substitutes Eqn.(8) in (11) the following relationship between the linear history accumulation constant and residual stress can be found

$$\sigma_r' = \sigma_c [1 + d_I/(1-d_I)B]^S, \tag{12}$$

which results in a monotonic relationship between the history variable d_I and residual strength σ_r'. However, the residual strength computed by using Eqn. (10) and (12) is different, i.e. Eqn. (10) does not follow linear damage accumulation law. Note that it is not the difference between the logarithmic shape of S-N law Eqn. (1) and the power law relationship (11), it is instead the assumed relationship Eqn. (10), which is used instead of Palmgren-Miner rule. It is only natural to use the residual strength instead of the history variable for taking into account load sequencing effects in this case. The Eqn. (10) does not take into account the R ratio, however various generalizations can be found.

Three values of loading amplitude to static strength ratios of 0.8 (High load), 0.521 (Low load) and 0.64 (Medium load) have been chosen to construct fatigue loading sequences. The residual strength for the three cases and the S-N curves are shown on Figure 6.

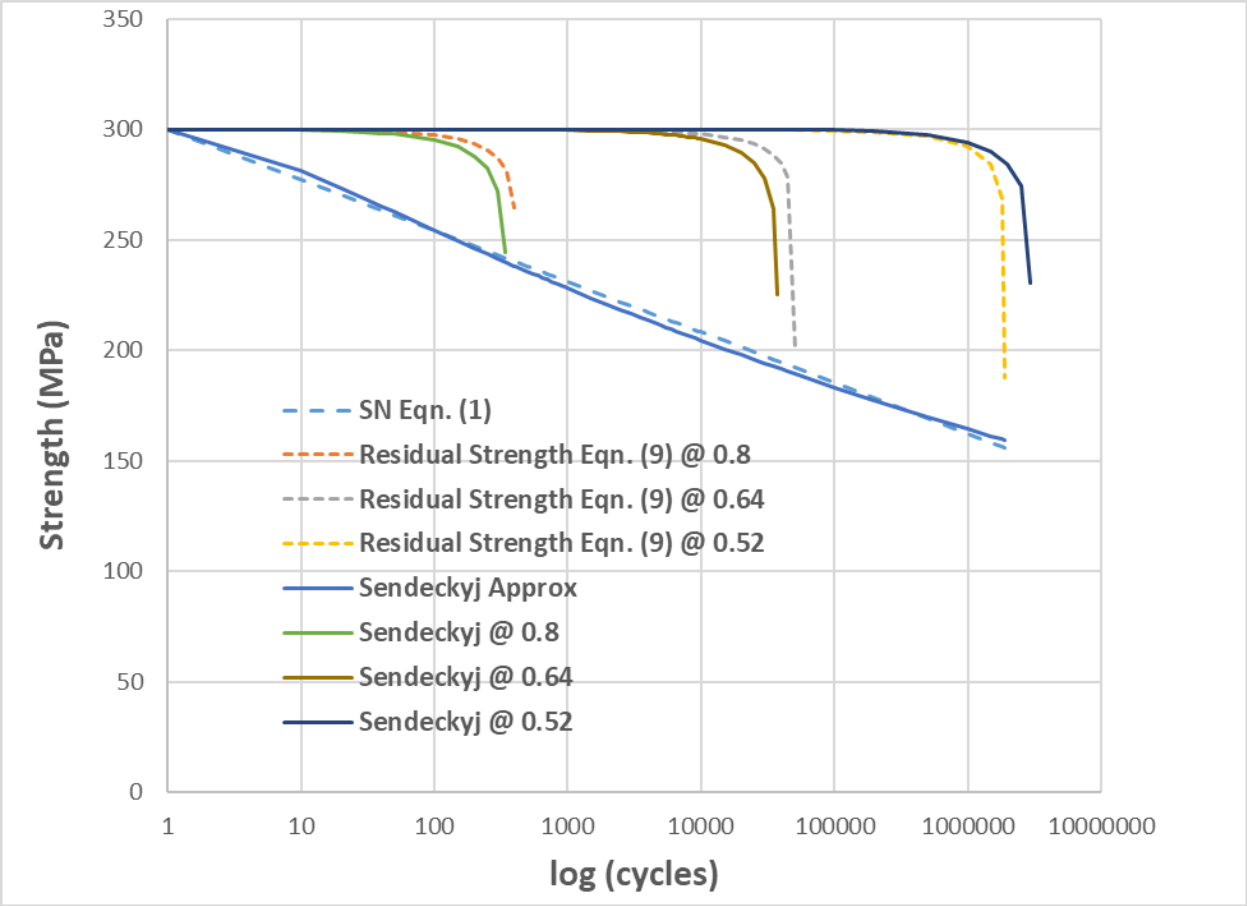

Figure 6. Different form of the S-N curve and block loading diagram.

Here and the next figures of this section the solid lines are reserved for Sendeckyj approach with strength tracking and the dashed lines for LOG approach with history variable Eqn.(1) and Eqn.(6)-(9). Two loading programs will be considered, each composed of 125 cycles at High load, 1875 cycles at low load and 4000 cycles at medium load. The residual strength and load amplitude as a function of cycles for repeating HLM sequence is shown in Figure 7. As one can see the two approaches result in a very close prediction of cycles to failure are 12020 in Sendeckyj and 12080 in LOG method.

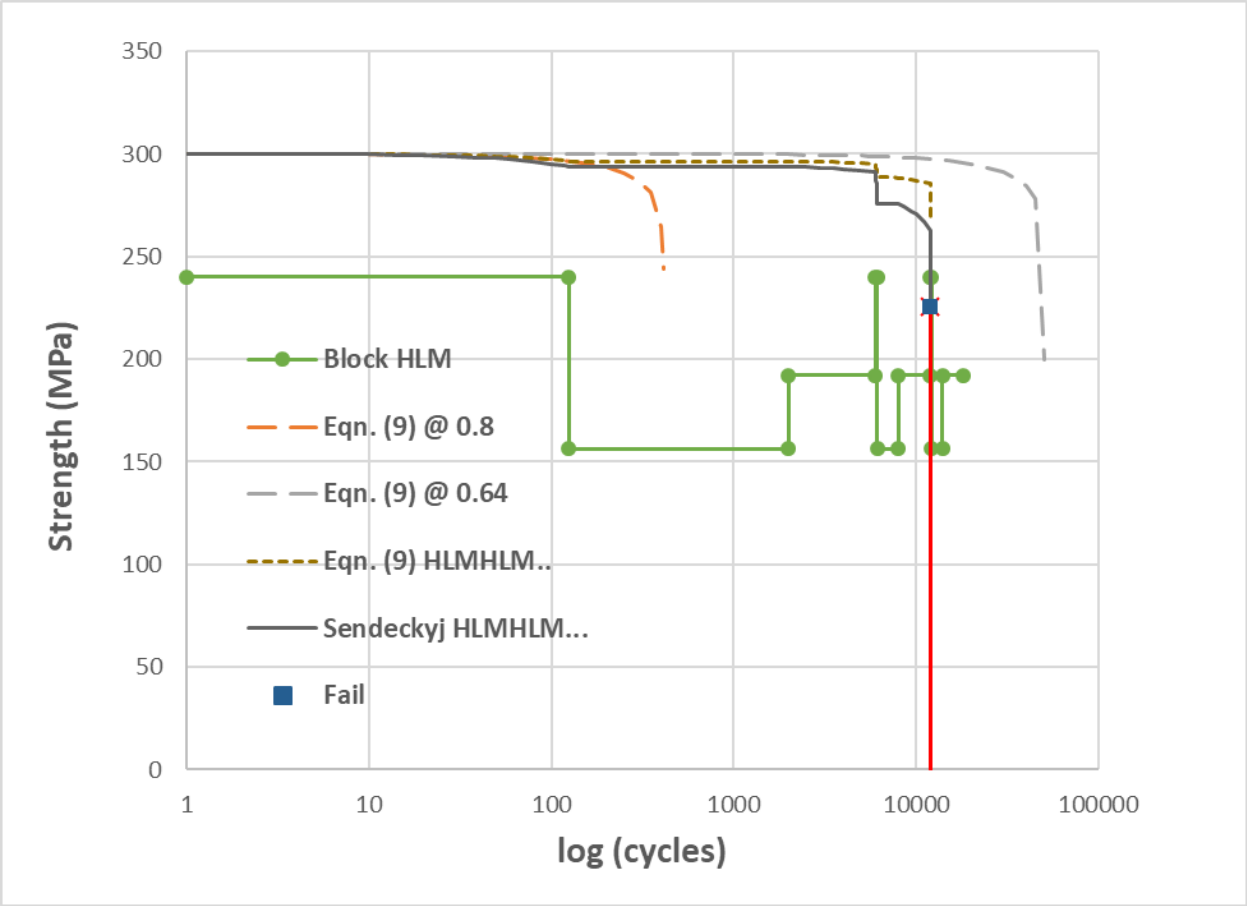

Figure 7. Loading amplitude and residual strength calculation by using Sendeckyj and LOG methods for HLM repeating block loading.

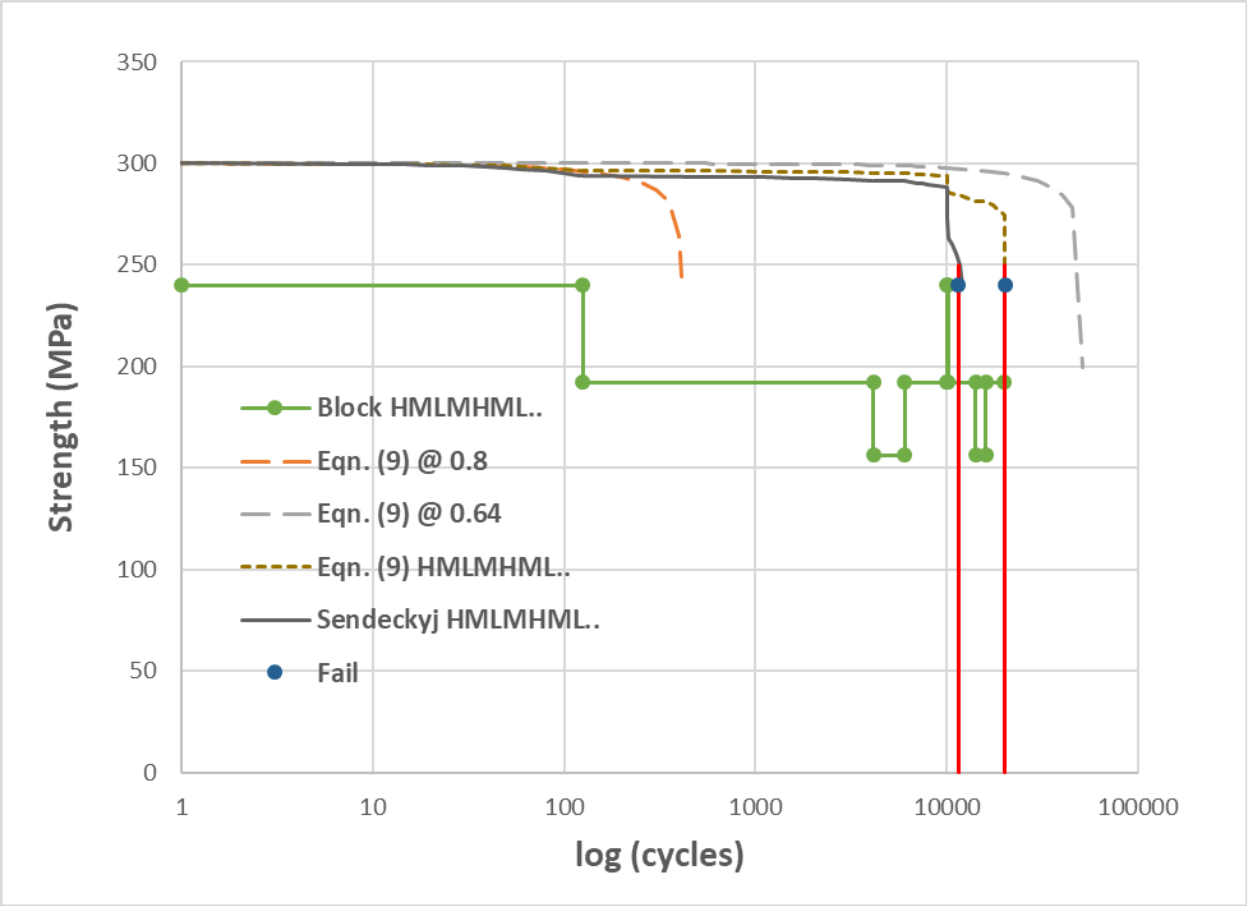

Figure 8. Loading amplitude and residual strength calculation by using Sendeckyj and LOG methods for HMLM repeating block loading.

However, a different loading sequence shown in Figure 8 displays that the two approaches can also result in significant difference in predicted cycles to failure values. The cycles to failure are approximately 12100 in Sendeckyj approach and approximately 20090 in LOG method.

The capability to prescribe loading amplitude as a function of step in arbitrary manner was a part of the BSAM setup and was used as the basis of changing the loading amplitude. However, to perform variable amplitude block loading in BSAM the fatigue loading algorithm underwent a significant change. The difficulty was to be able to match an exact or very close number of cycles to that prescribed in the block loading at each amplitude. An additional internal loop was introduced to achieve that and match the number of cycles required. The user input file control to activate this loop is very simple and consist of a single key word “block” following the keyword *time.

Example: Block loading 2000 cycles at 0.3 amplitude; 400 cycles at 0.2 and 500 at 0.5 amplitude

*time, block

0.1	0.1	0.1	0	0	-0.1	0	0	0.3	0
0	0	0	1000	1000	0	200	200	0	500

Where the load amplitude and cycle counts are placed in the table format for clarity. In this case 3 static loading step are performed to reach an amplitude of 0.3 at this amplitude two fatigue steps of 1000 cycles each are performed: then the amplitude is lowered to 0.2 and additional 2 fatigue steps of 200 cycles each are performed: followed by increasing the amplitude to 0.5 followed by 1 fatigue step with 500 cycles. The importance of subdividing a loading block is that the MIC insertion is only occurring at the end of the steps specified in the input file. Internally, however, the keyword "block" activates in loop which performs intermediate steps to achieve the prescribed number of cycles with a normally very small cycle increment dictated by the cohesive zone model, the mesh density and material parameters.

While basic models for predicting complex fatigue behavior are in place the validity of the assumptions, which are made to account for variation of fatigue regimes are often experimentally unsupported and require investigation.

3.1. Experimental evaluation of fully reversible fatigue properties

3.1.1. Short Beam Shear Fatigue Tests

Fatigue data for the Short Beam Shear specimens was generated by loading the specimens at a frequency of 10Hz and measuring number of cycles up to failure. Since crack growth is unstable, there is no damage progression. The fixture is shown in **Error! Reference source not found.**A-4. The goal of the design was to allow a fixed span of 1.2in., loading under 3-point bend, and one-sided visibility for DIC purposes. DIC data was gathered during the test but not used for analysis. The fixture has a top part which holds the specimen. The two jaws tighten and squeeze the specimen tight at the support locations. The loading rod contains a similar mechanism and tightens at the specimen in the middle. The bottom loading rod slides smoothly along two Teflon guides within the top fixture.

Note that the gripping function of this fixture slightly alters the loading state. Due to friction at the supports, the fixture is not allowed to freely rotate, so it is not strictly a three-point bend test. There is some amount of bending moment at the pin supports, which has caused a few specimens to fail under mixed-mode failure at the interface. Specimens that failed this way have been discarded; only specimens that have a pure tension failure have been accepted for analysis. In theory, the shear behavior is uncoupled from bending-related tension/compression stresses. Since shear behavior is still in the linear regime, further analysis assumes the loading state is equivalent to a proper three-point bend test.

Test results are shown in Figure 9 for specimens tested at a common R = 10 loading ratio, where maximum compressive load is 10x minimum compressive load. The second chosen loading ratio is fully reversible R = -1, where the loading rod both pushes and pulls at the specimen with equal magnitude. Other loading ratios have been considered but rejected due to limited resources.

$$1-2\ Plane, R=10, y=1.3959x^{-0.383}$$

$$1-2\ Plane, R=-1, y=0.8946x^{-0.447}$$

$$1-3\ Plane, R=10, y=1.2397x^{-0.373}$$

$$1-3\ Plane, R=-1, y=1.0905x^{-0.594}$$

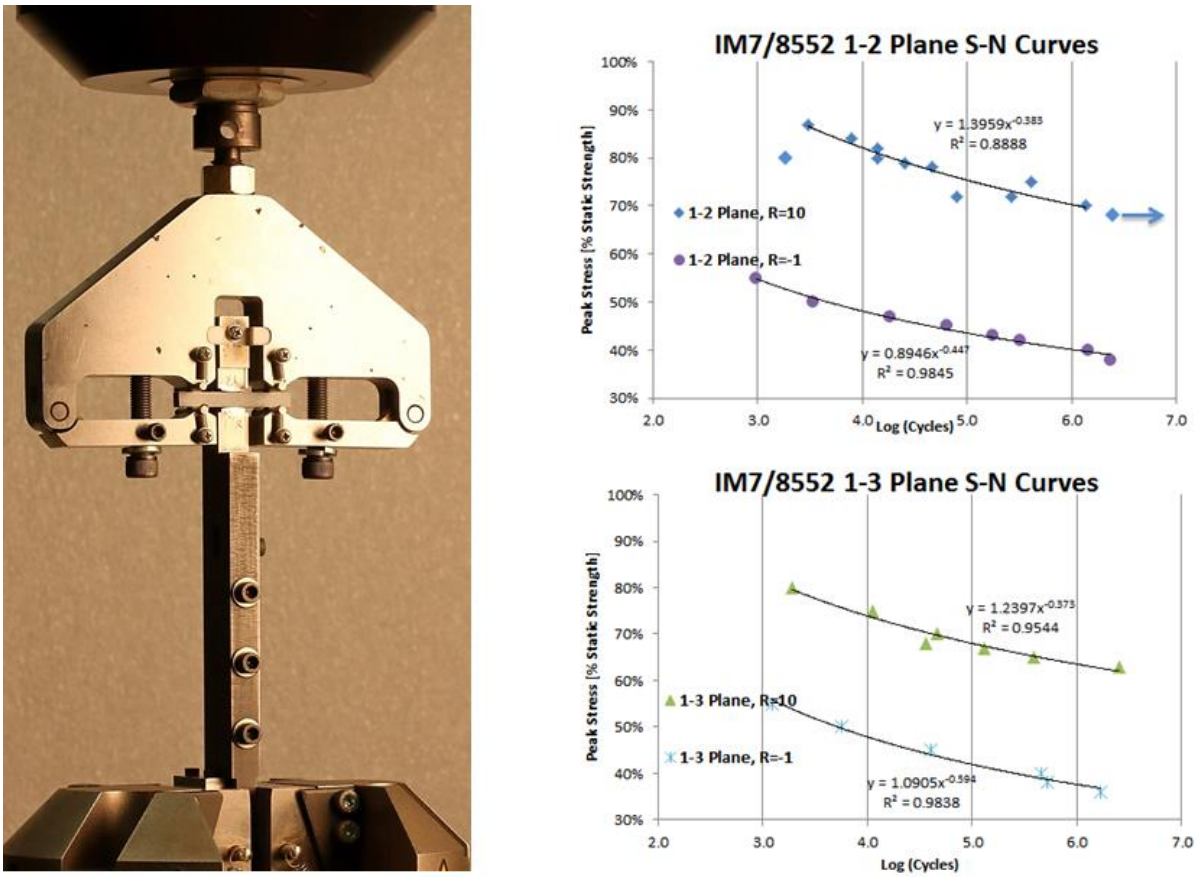

Figure 9. Custom 3-Point Bend Fixture for Measuring Reversible Fatigue Shear Data

Some significant observations in the data must be highlighted. First, the fatigue data is considerably different between the 1-2 and 1-3 material planes, which means the assumption of transverse isotropy is not accurate. Second, the effect of fully reversing the applied stress is very

large. Early thoughts were that every cycle fully reversed would be equal to two cycles from max to zero load. However, test data clearly shows that applied stress must be much lower at R = -1. It appears stress amplitude is a very important measure to consider. Therefore, consider Figure 10, which plots the fatigue data points against the modified Goodman line and the Gerber Parabola. Note that shear failure was either under positive or negative shear, without bias to either side. Therefore, consider the chart to be symmetric with respect to the y-axis (negative shear = positive shear).

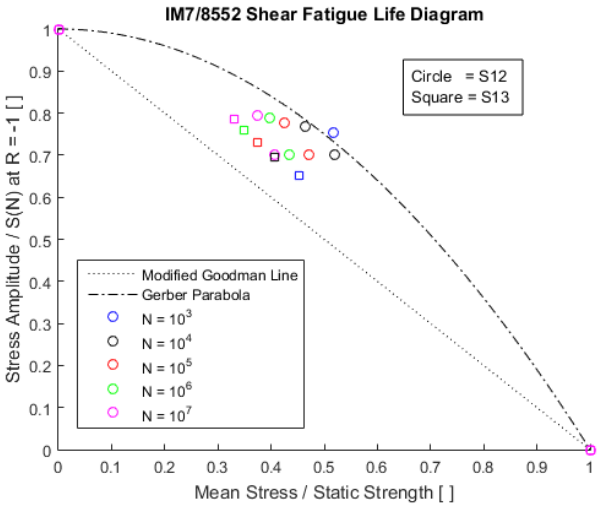

Figure 10. Fatigue data versus Goodman and Gerber lines.

3.1.2. Long Beam Three-Point Bend Tests

The three-point bend test lends itself very well to measure multiple failure modes. Long beams tend to fail in the region under the loading nose, where compressive stresses are very high. Consider the setup shown in Figure 11.

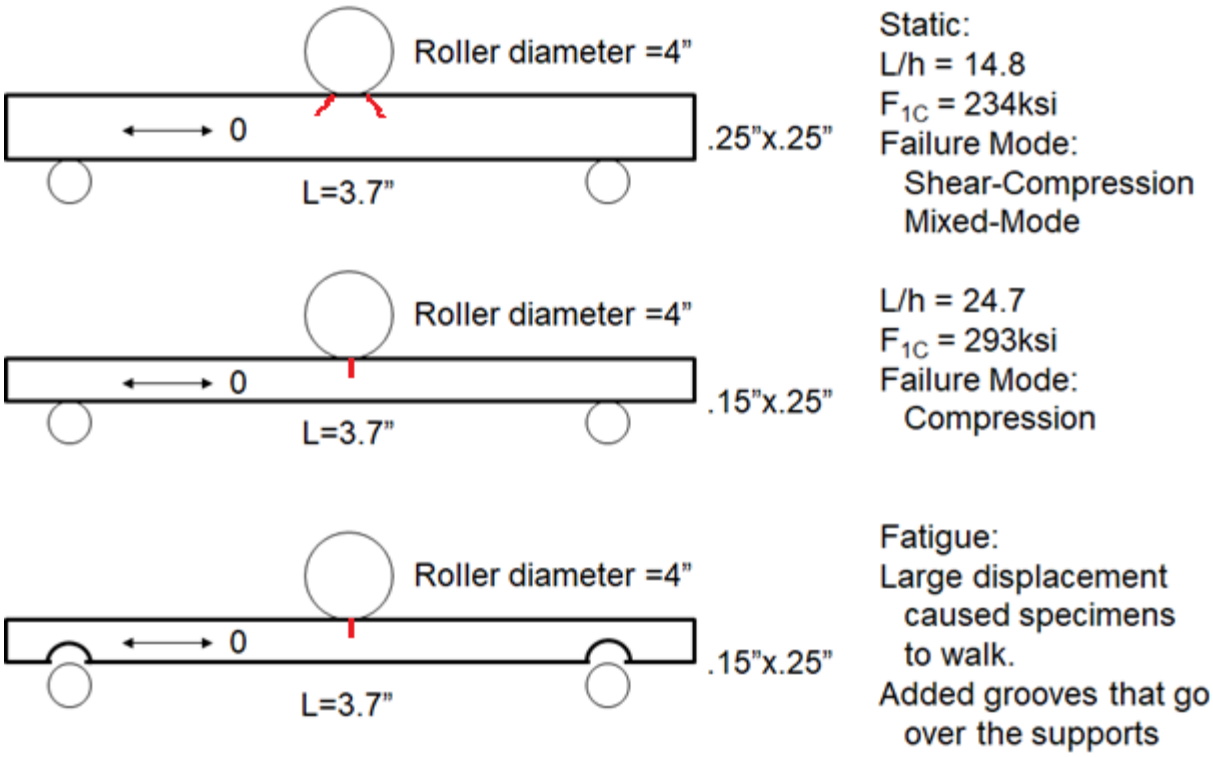

Figure 11. Three-Point Bend (Designed for Compression Strength/Fatigue) Test Results. Red indicates damage at the loading nose.

The long beam (L=3.7in.) is tested in the same way the SBS specimens were tested. The analysis calculates the maximum bending moment at the loading nose at time of failure and, assuming linear axial modulus, calculates the maximum compressive stress at the interface. Unfortunately, shear stresses are also very high at the region of contact, which causes these specimens to crack at a 45 deg angle just offset from the contact area.

Notice that Figure 11 shows a few adaptions to the specimens. By reducing the specimen thickness from 0.25 in. to 0.15in., the span-to-thickness ratio is increased from 14.8 to 24.7. As the second moment of area reduces faster than the cross-sectional area, this increases compressive stresses at the loading nose more severely than the shear stress. Indeed, these specimens fail under pure compression at a higher maximum compressive stress at 293ksi.

DIC data was gathered during these tests. Since the specimens fail early under compressive stress, the shear stress can only be measured during the linear regime. Results are shown in Table 2.

Table 2. Optimized material properties derived from long beam three-point bend test.

	Property	Long Beam	
	Plane	**1-2**	
Axial Modulus [Msi]	**E_{11T} [Msi]**	23.09	(2%)
	E_{11C} [Msi]	20.92	(2%)
	E_{11} [Msi]	22.00	(1%)
Poisson's Ratio [-]	**n_{12T}**	0.37	(14%)
	n_{12C}	0.37	(21%)
Strength [ksi]	**F_{1C} [ksi]**	-293.3	(5%)
	Failure Mode	Compression	
Shear Modulus	**G_{12} [Msi]**	0.711	(2%)
	K_{12} [ksi]	28.87	(2%)
	n_{12}	0.216	(3%)

To measure fatigue strength, only one load ratio was chosen (f = 7Hz, R = 10). By clamping the supports and loading nose, reversible load is possible, but would have caused secondary bending moments as described in the previous section. As these specimens are very compliant, needing high displacements, they would start to move away from their supports during tests. The smooth rollers on smooth specimen surface, along with large stroke displacements and perhaps machine vibrations would shake the specimen off the fixture. The fix is as shown in Figure 9, grooves were added at the support location. Specimens that failed early under mixed shear/compression were discarded from the data. Results are shown in Figure 12.

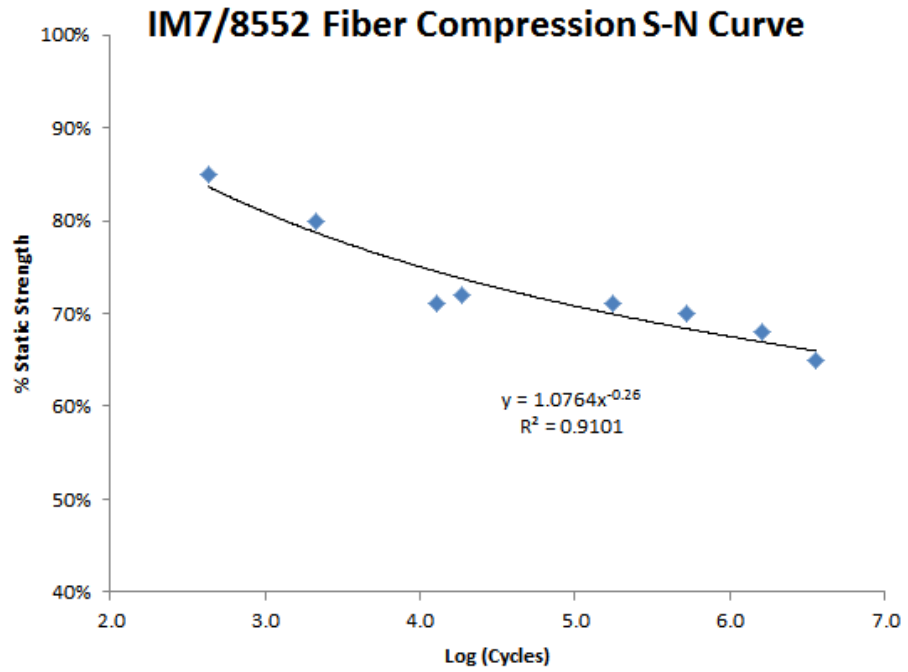

Figure 12. IM7/8552 Fiber Compression S-N Curve, f=10Hz, R = 10

3.1.3. End Notch Flexure Fatigue Tests

The fatigue tests for the ENF specimens do not have a corresponding ASTM standard. Inspiration is drawn from the work by O'Brien, Johnston, and Toland [30] and by Leitao [31], that attempt to measure the incremental crack growth per cycle as da/dN. During the test, the computer that controls the load frame logs a complete cycle load-displacement sweep at set intervals, such that the compliance may be calculated (after carefully subtracting system compliance). This compliance is compared to the compliance curves measured before the fatigue tests. Fracture energy is still given by closed form solution. Knowing the crack length "a", cycle count "N", and fracture energy "J", the da/dN curve is found.

Some modification to this test is the use of optical cameras to track the crack front and displacements at the crack front. Consider the test data in Figure 13, which plot crack length vs cycle count. The very fine data comes from the test frame computer algorithm providing a lot of compliance data. The green diamonds correspond to crack length measurements from the optical camera. The data shows that a slightly higher load leads to a sharply increased crack growth speed. Verification of optical measurements was necessary, as motion blurring makes it difficult to accurately pinpoint the crack tip. From the data in Figure 13, one may assume that optical measurements are approximately accurate to within 1mm.

With 8 specimens available, the intent was to test 4 specimens at R = 10, and 4 at R = -1 (fully reversible). Due to the growing crack, each specimen tests crack growth at a range of fracture

energy, such that there is some overlap between specimens. This has led to the choice of testing the specimens at 20%, 30%, 40%, and 50% of PC fracture toughness.

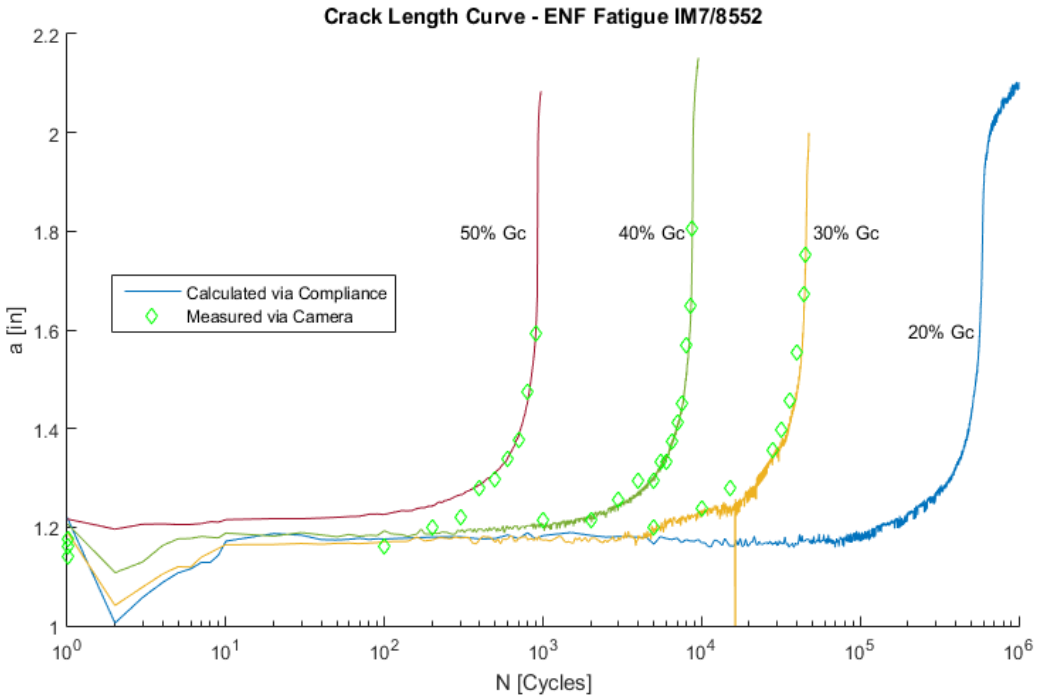

Figure 13. Crack Length Progression during ENF Fatigue Tests, f=3Hz, R = 10

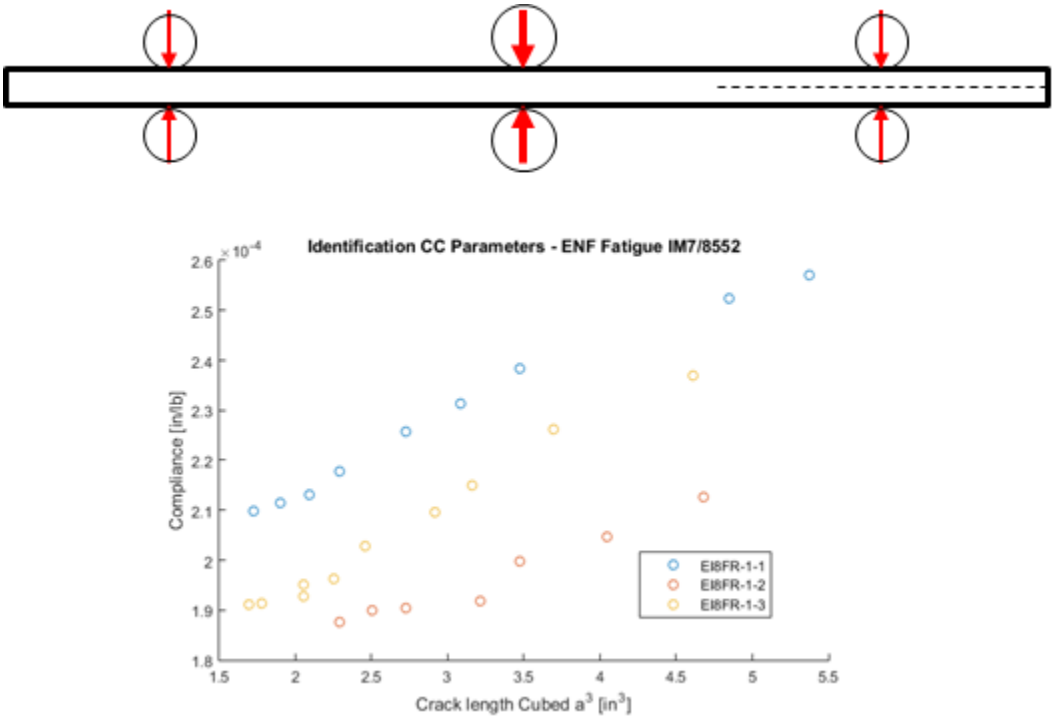

Figure 14. Compliance Curves for Clamped ENF Specimens, as calculated during Fatigue Test.

The aforementioned method works well at R = 10. However, it fails when the test is run fully reversible. When the supports are tightened, the specimen is effectively clamped-clamped between the supports, and thus significantly stiffer. This stiffness depends on how the screws get tightened, so the compliance curves are very inconsistent. Instead, the compliance curves are calculated by the data already being collected as the fatigue test is running: compliance from the test frame, and crack length measurements from optical cameras. Plotting these variables leads to a linear relationship (Figure 14). This compliance curve is necessary for calculating the fracture energy per ASTM standard.

The data for R = 10 (not clamped) is shown in Figure 15. Note that this is data from multiple specimens tested over different ranges, which causes a few series of dots to not quite overlap. The result of this test compares very favorably compared to the reference data [30], but with less scatter. This shows it is very important to accurately measure the crack front (such as with µCT) before running the test.

Since there is third-party agreement in test results, there is confidence in the usefulness of the data. However, the analysis of the clamped-clamped fully reversed ENF specimens was not documented in literature. Therefore, one more specimen was tested at R = 10, but fully clamped. This specimen was much stiffer, and the crack grew at a much higher load. After correcting for

compliance, the da/dN data points fell right on top of the other specimens (included in Figure 15). This means there is a good agreement between clamped and unclamped specimens.

The remaining three specimens were tested at 20%, 30%, 40% PC fracture toughness at R = -1, f = 3-5Hz. Note that $\Delta G = G_{max}$ per ASTM E647. The three specimens are nearly aligned in one line with each other. A slight offset of the one specimen may be caused by a slight misreading of the crack length in the optical field measurements.

The data in Figure 15 and Figure 16 have been plotted on the log-log scale to fit the Paris-Law parameters to the data. The fact that the data is linear implies that the Paris-Law is a useful method for estimate da/dN behavior, although the end behavior is not captured. The coefficient and power parameters of the Paris law indicate that the crack growth at fully reversed loading is much faster compared to single-direction loading R = 10. Indeed, plotting both datasets together on the same plot Figure 17) shows a drastic difference. The following may be visible:

- At ΔG_{II} = 1.2 in-lb/in^2, the crack growth at fully reversed loading is 40x that of single direction loading.
- The fracture energy at da/dN = 3E-7 in/cycles is 4x higher at single direction loading.
- The fracture energy at da/dN = 9E-5 in/cycles is 2x higher at single direction loading.
- The slope of the two data sets is different and seem to converge at $\Delta G_{II} = G_c$.

The trends that are visible during mode II fracture fatigue loading are very similar to that established during shear stress fatigue loading. Fully reversed loading is significantly more damaging that single direction loading. The stress amplitude as well as maximum stress seem to be important life prediction parameters.

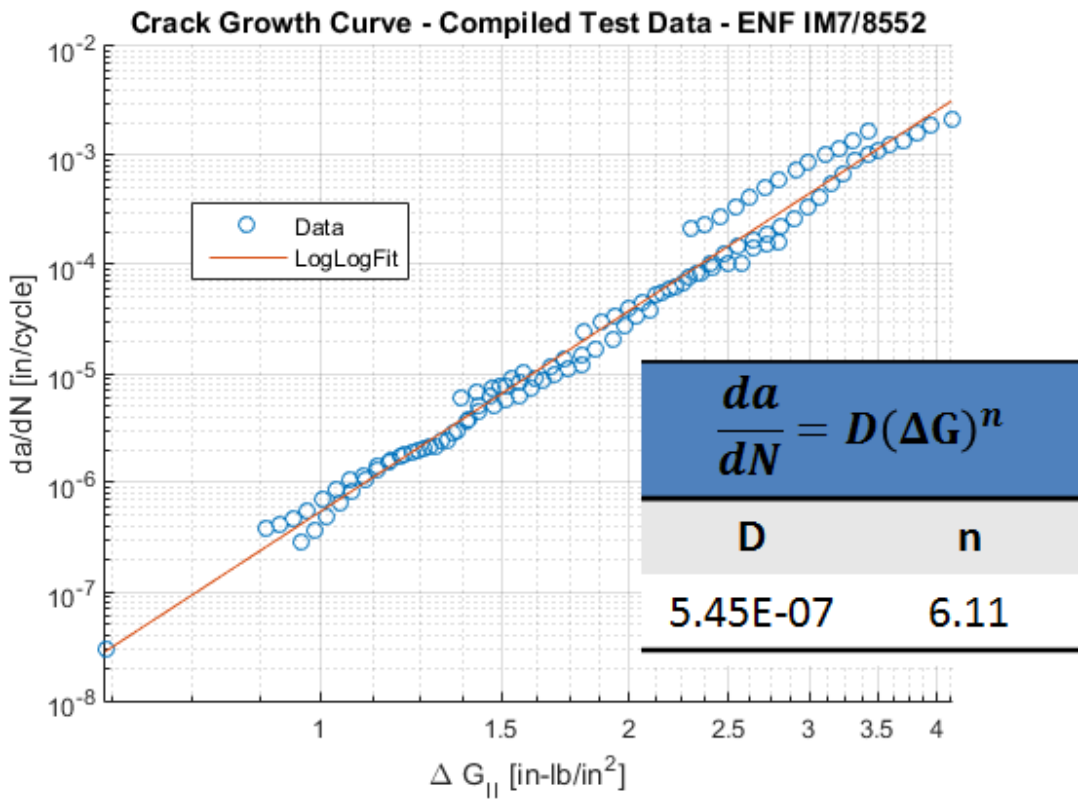

Figure 15: da/dN Curve for IM7/8552, Mode II, R = 10

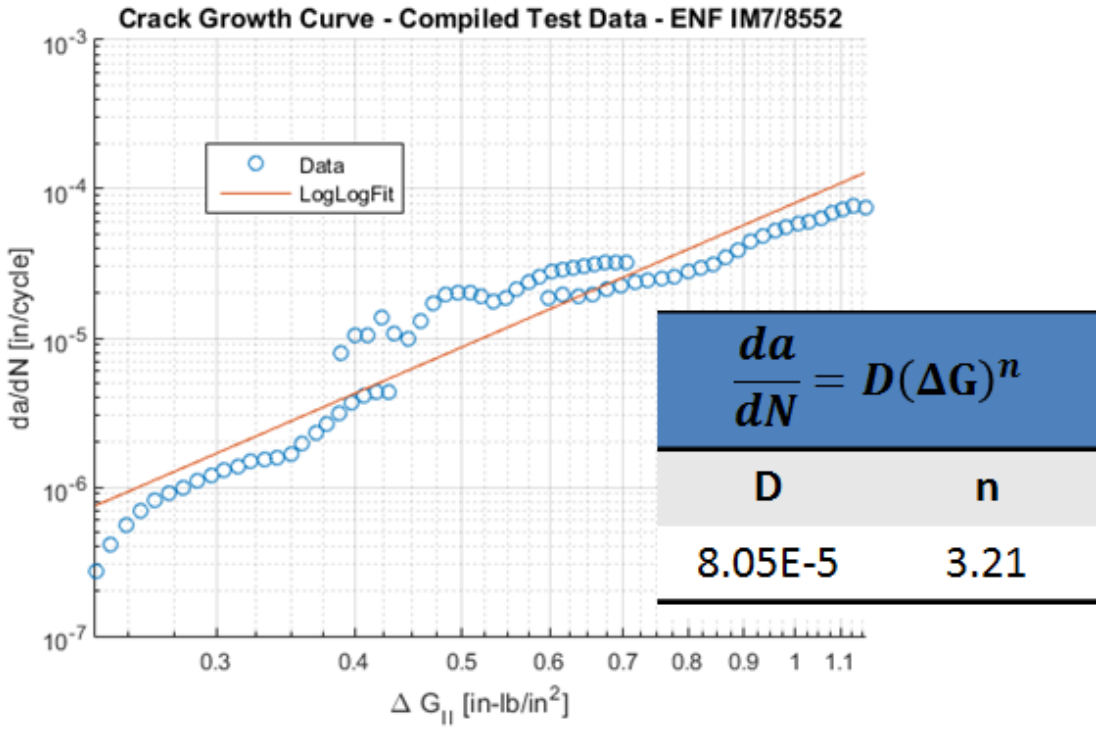

Figure 16. da/dN Curve for IM7/8552, Mode II, R = -1.

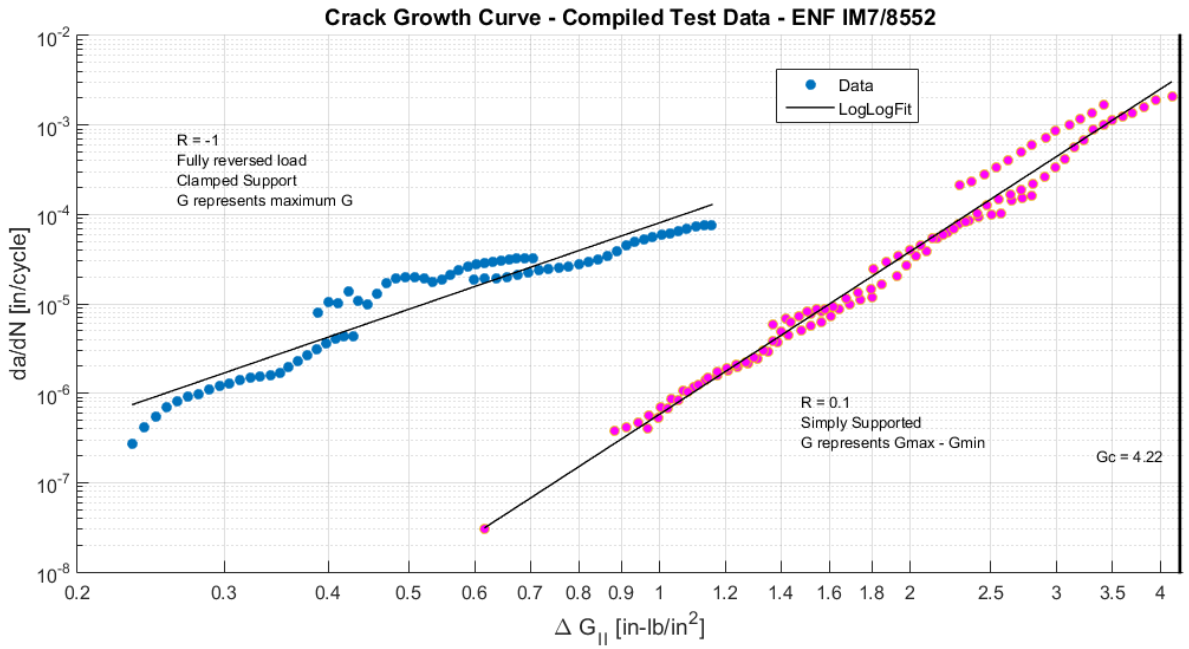

Figure 17. Overlay of da/dN Curves for IM7/8552, Mode II. Fully Reversed (R = -1) in Blue/Left. Single Direction (R = 0.1) in Purple/Right.

4. Stochastic Seeding of Transverse and Fiber Dominated Strength Properties

Laminated composite materials are used in a variety of aerospace, automotive, and sports equipment applications. In designing these parts, coupon tests are performed to determine the material properties to be used in the design. However, manufacturing and material variation cause significant strength variations within a single part in all three material directions. Significant amount of work was devoted to measurement and characterization of variation of basic stiffness and strength properties of tape composites, and in-situ transverse tensile strength in particular. The subject literature is very extensive and the reader is referred to recent experimental work [1] including references. While the mechanism and interlay of strength controlled initiation and fracture mechanics controlled propagation as a function of ply thickness are well understood, it is pointed out that additional brittle strength scaling concepts are required to explain the entire spectrum of results.

Understanding the implications of input property variation and scaling is also critical to application of progressive damage analysis (PDA) to design and certification of composite structures. Thus recently performed simulations of failure initiation and propagation in Clamped Tapered Beam (CTB) specimens [2] showed good agreement with experimental data for ply level transverse strength parameter obtained by using 3 point bend (3PB) test method [3] whereas the results obtained by using an almost two times lower value resulting from tensile testing of 90° coupons [4] resulted in 30% underprediction of the peak load. The goal of the present work is to introduce spatial scatter of transverse strength parameters into simulations and attempt to predict the strength of all categories of coupons. i.e. 90° tension, 3PB and CTB specimens with a single set of input parameters.

The Discrete Damage Modeling (DDM) method utilizing Regularized Extended Finite Element Method (Rx-FEM) was used for simulation [5], [7]. Two aspects of this mesh independent cracking methodology are affected by random distribution of transverse strength. One is the randomization of the crack initiation location, and second is the cohesive zone methodology based propagation with nonuniform variation of release pressure. The fracture toughness in the mode I and II were not varied in the present study. The cohesive zone model response with random seeding of initiation strength was theoretically investigated first and showed that a finite physical dimension based seeding is required to reproduce the Weibull type weak link failure load scaling with the nonuniform field of initiation strength. Namely if the initiation strength is seeded based on the integration point the global behavior is not brittle. Next the minimum dimension of the seed was evaluated by modeling 3PB and standard tensile coupons and finally the CTB revisited.

4.1. Deterministic Cohesive Zone Model

We begin by discussing the mixed-mode cohesive zone interface fracture model proposed by Turon et al. [32]. The brief description below is given for completeness of the present

formulation and the reader is referred to reference [32] for full details. We consider an arbitrary point at the crack interface with a normal vector **n** and a displacement jump vector Δ**u**. Our goal is to describe the fracture energy of separation of an arbitrary interface point.

The cohesive energy can be written in the invariant form as a function of the norm of the displacement jump λ=||Δ**u**|| and a mode mixity parameter, *B*

$$B = 1 - \frac{\langle \Delta u_n \rangle^2}{\lambda^2} \tag{13}$$

where $\Delta u_n = (\Delta \mathbf{u} \cdot \mathbf{n})$ $\Delta u_n = (\ \Delta u \cdot n)$ is the normal, mode I component of the displacement jump, and the brackets $\langle x \rangle = \frac{1}{2}(x + |x|)$ $\langle x \rangle = \frac{1}{2}(x + |x|)$ represent the McAuley operator. The parameter *B* is equal to 0 for mode I propagation and is equal to 1 for mode II propagation. The functional shape of the fracture energy as a function of the displacement gap is defined by the relationship between the cohesive tractions and the displacement jump, which is assumed to have the form:

$$\tau = (1-d)K\Delta u + dK\langle \Delta u \cdot n \rangle \quad \boldsymbol{\tau} = (1-d)K\Delta \mathbf{u} + dK\langle -\Delta u_n \rangle \mathbf{n} \tag{14}$$

where *K* is a high initial penalty stiffness and *d* is the damage parameter. The first term in Equation (14) represents the crack cohesive force, and the second term prevents interpenetration of the crack surfaces. A bilinear relationship is assumed for the magnitude $\tau(\lambda)=|\boldsymbol{\tau}|$ of the cohesive traction vector, defined in (14), such that $d = 0$ if $\lambda < \Delta_0$ and $d = 1$ if $\lambda > \Delta_1$. The initial value of the displacement jump, beyond which the interface failure begins, is defined as

$$\Delta_0 = \tau_0/K, \tag{15}$$

where τ_0 is the cohesive strength. The cohesive strength depends on the mode mixity parameter *B* as

$$(\tau_0)^2 = Y^2 + (S^2 - Y^2)B^\eta, \tag{16}$$

where *Y* and *S* are the interfacial normal and shear strengths, respectively, and η is an experimentally determined influence parameter. The fracture energy density $g(\lambda,B)$ is the area under the $\tau(\lambda)$ curve, so that

$$g(\lambda, B) = \int_{q=0}^{\lambda} \tau(q, B) dq \,. \tag{17}$$

To ensure the correct crack propagation characteristics, the final value of the displacement jump, Δ_1 is defined so that the following condition is satisfied

$$g(\Delta_1, B) = G_c(B), \tag{18}$$

where the critical energy release rate (ERR), G_c, or fracture toughness, is assumed to be a function of the mode mixity as follows [32]

$$\tau = (1\text{-}d)K\Delta u + dK\langle \Delta u \cdot n \rangle \; G_c = G_{Ic} + \left(G_{IIc} - G_{Ic}\right) B^{\eta} \tag{19}$$

and G_{Ic} and G_{IIc} G_{Ic} and G_{IIc} are experimentally measured fracture toughness values. In the case of a bi-linear $\tau(\lambda)$ relationship, the final value of the displacement jump is determined by the initial value of the displacement jump and the fracture toughness as

$$\tau = (1\text{-}d)K\Delta u + dK\langle \Delta u \cdot n \rangle. \tag{20}$$

All parameters entering the analysis, such as the fracture toughness and strength values, are material properties that can be measured by using standard test methods.

4.2. Cohesive Zone Model with Random Distribution of the Cohesive Strength

The material properties such as the cohesive zone strength and fracture toughness are expected to vary spatially in any given material. To characterize such variation *insitu* is a formidable problem whereas this variation will have an effect on failure processes and strength of coupons and structures. In the following we will explore such effects by considering spatial variation of cohesive strength Y and S in CZM described above. In this section we will obtain basic analytical results on an example of Mode I loading and focus on the strength rather than propagation aspects in CZM modeling. We will consider flat surfaces held together in every point with cohesive force (14) as shown in Figure 18. These surfaces are pulled apart by a uniform displacement jump of $\Delta\mathbf{u}$, and $\lambda = \|\Delta\mathbf{u}\|$**.** Each point x along the surface has a value of cohesive strength $Y(x)$ which is a random variable and thus results in cohesive force of $\tau(x)$, which we rewrite for monotonic tensile loading under Mode 1 in simplified form.

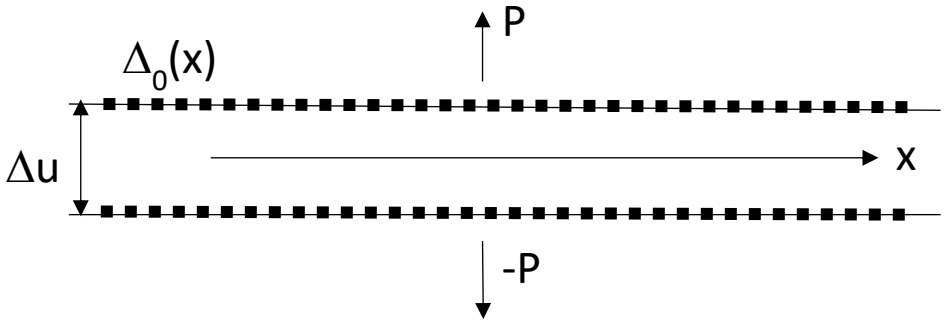

Figure 18. A cohesive surface with constant displacement jump and randomly varying Δ_0 in each point.

$$\tau = \begin{Bmatrix} K\lambda, \lambda \le \Delta_0 \\ Y\dfrac{\Delta_1 - \lambda}{\Delta_1 - \Delta_0}, \Delta_0 < \lambda \le \Delta_1 \\ 0, \lambda > \Delta_1 \end{Bmatrix} \tag{21}$$

In Equation (21) the spatial coordinate is omitted, however, parameters τ, Y, Δ_0 and Δ_1 vary in each point and only the penalty stiffness and the displacement jump are independent of *x*. The displacement jump values Δ_0 and Δ_1 corresponding to damage initiation and failure can be obtained from Equations (15) and (20) and expressed in our simplified case as

$$\Delta_0 = Y/K; \Delta_1 = 2G_c/Y \tag{22}$$

where the penalty parameter K and the fracture toughness G_c are constant. We consider λ to be the loading parameter so that the cohesive force τ(Y, λ) is a function of random variable Y for a given displacement jump. Assume Weibull distribution for Y as following

$$F(Y < y) = 1 - e^{-(y/\beta)^{\alpha}} \tag{23}$$

And the associated probability density function as

$$f(y) = \frac{dF}{dy} = \alpha y^{\alpha-1} e^{-(y/\beta)^{\alpha}} / \beta^{\alpha} \tag{24}$$

where α and β are shape parameters responsible for scatter and mean respectively. One can now calculate basic characteristics of the cohesive force as a function of the displacement jump λ,

$$\begin{aligned} E(\tau) &= \int_0^{\infty} \tau(y,\lambda) f(y) dy \\ E(\tau^2) &= \int_0^{\infty} \tau^2(y,\lambda) f(y) dy \end{aligned}, \tag{25}$$

which provide the average value $\tau_{ave}(\lambda) = E(\tau)$ and variance $\mathrm{Var}(\tau(\lambda)) = \sqrt{E(\tau^2) - (E(\tau))^2}$ of the cohesive force. According to Equation (21) the cohesive force is a piecewise continuous function and the integrals (25) have to be taken over separate integration intervals, i.e.

$$E(\tau) = \int_{K\lambda}^{\infty} (K\lambda) f(y) dy + \int_0^{\min\left(K\lambda, \frac{2G_c}{\lambda}\right)} y \frac{2G_c - y\lambda}{2G_c - y^2/K} f(y) dy \tag{26}$$

The first integral in Equation (26) corresponds to the first $\lambda \le \Delta_0$ interval of (21) and the second integral corresponds to the second $\Delta_0 < \lambda \le \Delta_1$ and third $\lambda > \Delta_1$ intervals. Noticing that the first integral in Equation (26) can be readily calculated in the closed form we obtain the following expression for average value of cohesive traction at which the cohesive zone initiates damage

$$E(\tau_{G_c=0}) = K\lambda e^{-\left(\frac{K\lambda}{\beta}\right)^{\alpha}}, \tag{27}$$

which is similar to the response of an infinite bundle of fibers under uniform strain when an individual fiber strength follows Weibull distribution. Indeed, the term $K\lambda$ in Equation (27) is equivalent to stress carried by a fiber and the exponent is the portion of surviving fibers under this stress, i.e. $1\text{-}F(K\lambda)$, given by Eqn. (23). Such behavior is not brittle. The implication of this

behavior is that the strength is governed by average and not the weak link type behavior of the individual integration points. The only possibility to recover the brittle behavior by using the CZM approach is to have a cluster of integration point seeded with equal strength such that when it is exceeded the size of the cluster is sufficient to activate the fracture mechanics CZM mechanism and lead to catastrophic failure. Even though an analytical approach to this problem is possible, a numerical path will be explored below.

4.3. Discrete Damage Modeling

The simulation begins without any matrix cracking locations built into the model. The loading is applied in incremental way and the stress field at each load step examined through the entire specimen. If a failure criterion, and specifically LaRC04 [33] in the present case, is met an Rx-FEM cohesive zone is inserted and will begin to open under increasing load to form a matrix crack. Thus, the random distribution of strength will affect not only the opening characteristics but the location of the matrix crack.

4.4. Random Spatial Seeding with Volumetric Scaling

Weibull distribution is used to seed the strength in the finite element (FE) models. The smallest volume seed available in a FE formulation is the integration point. The volume which can be associate with it is $V_i=w_iJ_i$, where w_i is the respective Gauss weight and J_i the determinant of the Jacobian matrix. Next volumetric entity will be the finite element and its volume V_e can be calculated as $V_e = \sum w_i J_i$, where the summation is taken over all integration points. In the present analysis larger volumetric seeds are considered in a following manner. A uniform spatial grid with a (l_x, l_y, l_z) spacing is erected and all integration points falling within one grid cell are assigned the same value of the parameter of interest. Consider a material strength parameter X. The discussion below equally pertains to fiber direction strength and/or transverse strength as long as it exhibits Weibull volume scaling. The value of strength is assigned based Weibull distribution (23) updated with volumetric scaling of strength, where

$$F(\mathrm{X} < x) = 1 - e^{-\frac{V_s}{V_0}\left(\frac{\sigma}{\beta}\right)^{\alpha}} \tag{28}$$

and the seed volume is $V_s= l_1\, l_2\, l_3$. The parameters α and β define the scatter and the average value of strength σ_a so that

$$\sigma_a = \beta\Gamma\left(1+\frac{1}{\alpha}\right) \tag{29}$$

A demonstration distribution of strengths is shown in Figure 19. The different colored regions in Figure 19 represent different strength seeds over the highlighted region. The seeding is performed based on a total number of seeds in the model N_s by using uniform distribution of

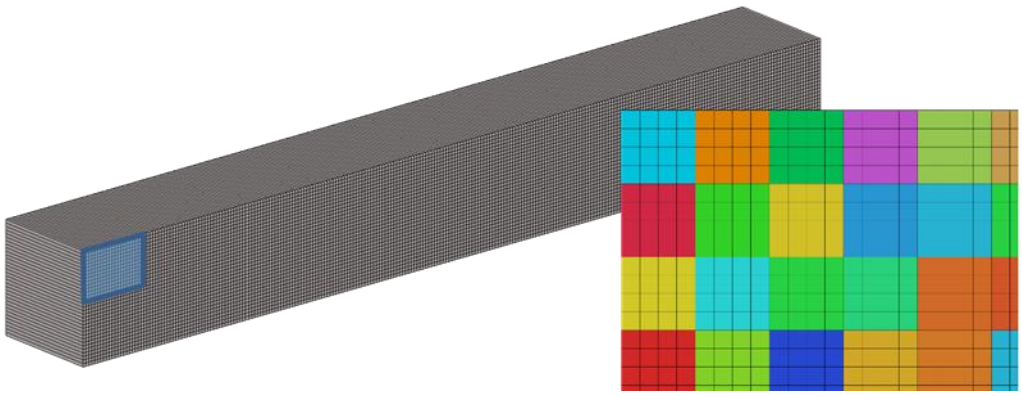

Figure 19. Demonstration of Stochastic Seeding in a Specimen. This solid lines represent element boundaries.

the probability *F* generated by standard random number generator available in the Math Kernel Library. In this case the transverse strength assigned for a seed which was assigned random value of the probability f_s the strength will be as following

$$X = \beta\left(-\frac{V_0}{V_s} ln(1 - f_i)\right)^{1/\propto} \qquad (30)$$

4.5. Deterministic Progressive Fiber Failure (DPFF)

Progressive fiber failure is the only damage mode simulated by using property degradation technique in the present work, so that the stiffness tensor at a given stress level is defined as $\mathbf{C}=(1-d)\mathbf{C}_0$, where $\mathbf{C}_0$ is the initial stiffness. Note that the property degradation is isotropic and a small threshold value 10^{-8} is used to retain nonzero stiffness in the element to avoid convergence issues. The damage variable, *d*, is defined based on the stress strain relationship shown in Figure 20. This curve is characterized by 2 physical quantities, the strength X value and the fracture

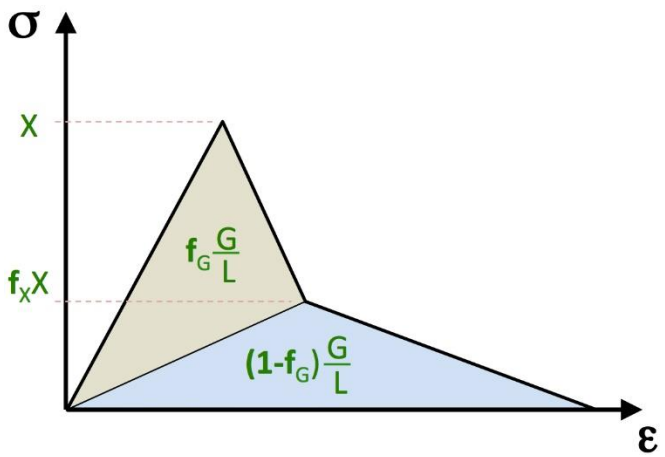

Figure 20: Schematic of the Uniaxial Response in Longitudinal Tension in the Fiber Direction Described in Maimi et al. [34], [35]

toughness G. In the present work we are using this model both for tension and compression failure modeling and in the latter case $X=X_c$. The fracture toughness value is obtained from Ref. [25] for IM7/8552 to be $G=G_{XC}=25.9$ N/mm. Compression failure mode is kinematically accompanied by material self-interpenetration. This phenomena occurs in the surface contact based constitutive models as well and is prevented by McAuley operator term in Eqn (31). A similar modification is required for volumetric stiffness reduction based failure modeling. The dilatational strain tensor invariant is used to accomplish this objective as in Ref. [6] in a way similar to the displacement jump in Eqn. (14). The following penalty term R_c is added to the element strain energy balance to prevent material self-interpenetration

$$R_c = rE_{11}\int_{V_e} d\left\langle(\varepsilon_{11}+\varepsilon_{22}+\varepsilon_{33})+\varepsilon_{kink}\right\rangle^2 dV \tag{31}$$

Expression (31) has energy dimension and penalizes the volume change if the material is in compression when $d>0$. At the same time it does not restrict shape change and allows for shear band like behavior. Coefficient $r=1$ and $\varepsilon_{kink}=0$ in the present study. Various refinements to (31) can be foreseen in the future, i.e. a threshold value $\varepsilon_{kink}>0$ to account for kink band collapse width, and $r>1$ for material hardening in the incompressible mode maybe introduced based on experimental measurements.

4.6. Stochastic distribution of fiber direction properties

The process of defining the random value of strength assigned to a volume seed based on Eqn. (28)-(30) was described above. The random string generator is part of MKL and uses initiation value for generating the quasi random string. The quasi –randomness of the string is best illustrated by the fact the same value of the generator will always lead to the same "random"

string. The input block for the statistical distribution is shown on Figure 21. Note that previous versions of BSAM did not contain a separate block for statistical property input. Instead the statistical parameters were part of a material. The new approach is more general and allows to describe different sub-regions within the same cluster with different property distributions as well as different distributions of different parameters at the same time. The block begins with assigning an ID, in this case uniXt; the type =3, corresponding to coordinate based seeding and the approximation (FE model), in this case approx=1. A new parameter is introduced seed_window_section, which defines the section required in the FE model which defines the constitutive law and the element set where the distribution will be applied. Next parameter seeding = {fibers, coordinates} can have two values depending on the spatial direction of the seeding bricks. If seeding = coordinates then the axis 1,2,3 of seeding bricks are aligned with global coordinate axis x,y,z. If seeding = fibers then the seeding blocks are aligned with the fiber direction. Next line defines the size of the seeding brick l_i=, i=1,2,3. It should begin with a key word coordinates if seeding = coordinates.

```
STATISTICAL DISTRIBUTIONS

stat-uniXt

type = 3

approx = 1

seed_window_section=1

   seeding = fibers

   fibers = 0.9769230800001, 0.9769230800001, 0.2108200001
```

Figure 21. Statistical variation INPUT BLOCK

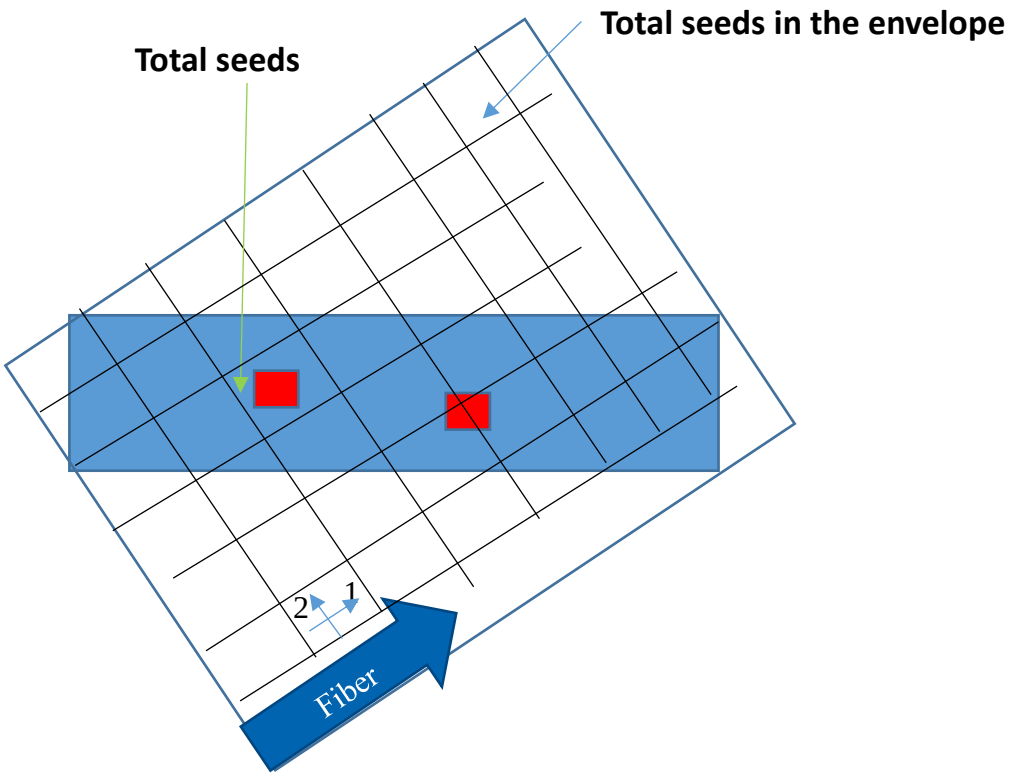

Figure 22. Illustration of the spatial seeding process for arbitrary fiber orientation

Next lines define the Weibull shape parameter α, the control volume V_0 and the generator value as described above.

The seeding process for arbitrary fiber orientation is illustrated on Figure 22. A virtual seeding envelope is generated so that the seeding brick axis 1,2,3 are aligned with the fiber orientation vectors defined for each element. In this case the axis 1is oriented in the fiber direction shown by arrow in the bottom left corner. As seen, the virtual seeding envelope contains a number of seeding bricks outside the actual specimen. An algorithm is created to identify the center of each element with a particular brick and discard the ones, where no elements were found and thus compute a number of seeding bricks Ts, covering the cluster and more specifically the element set defined in the section command. The volume of each seed V_s is calculated by summing up the volumes of elements populating the brick rather than using its nominal volume.

The fiber direction strength distribution generated by using different sizes of the seeding window length are shown in Figure 23. As one expects the range of the strength distribution is similar and with increasing the size of the window in fiber direction the fiber oriented seeding becomes apparent.

(a)

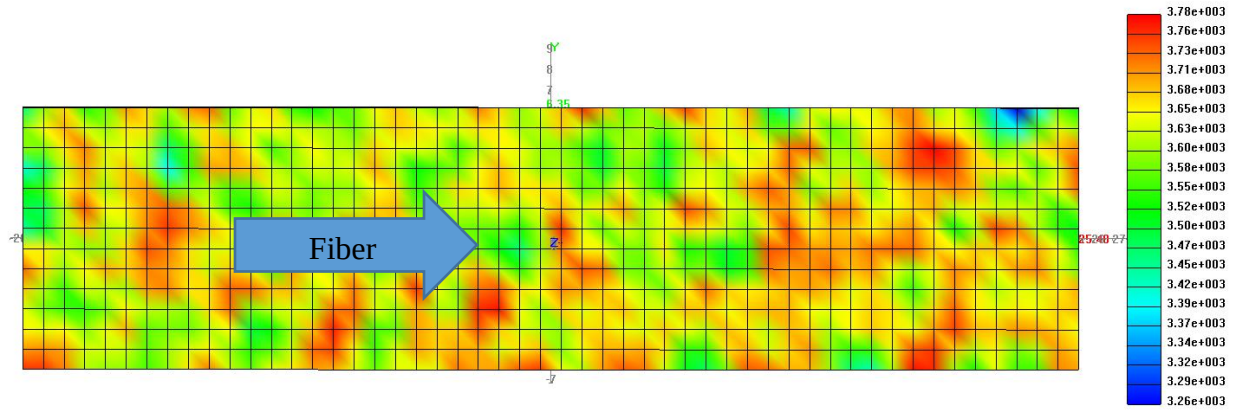

(b)

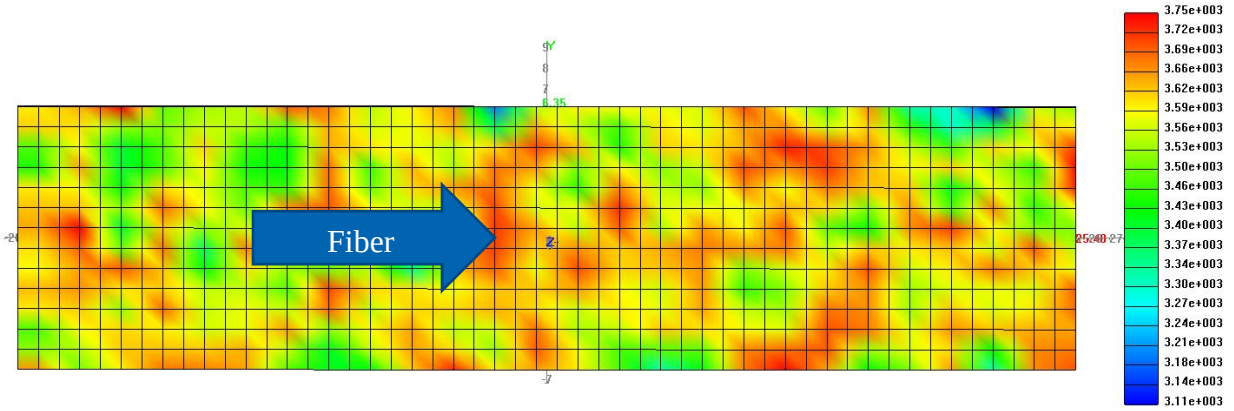

(c)

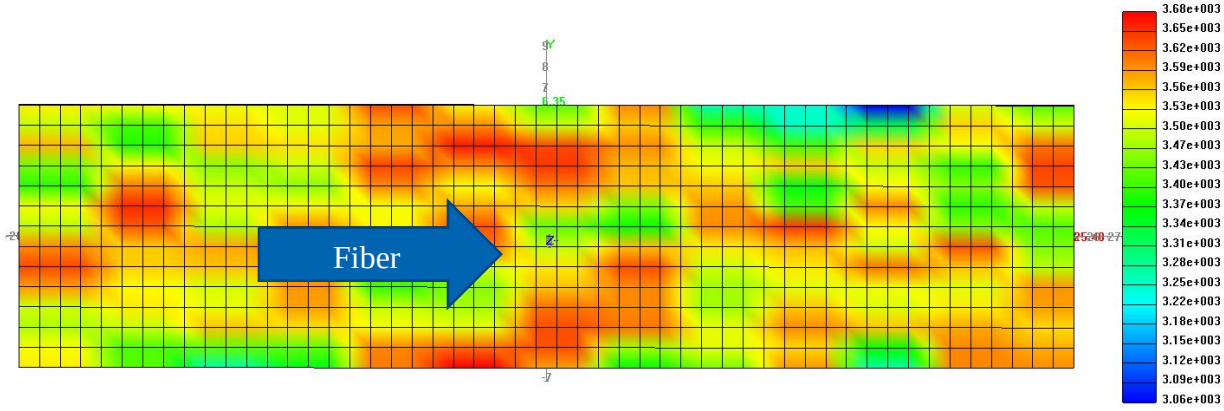

Figure 23. X_T distribution in a 0° ply for different seed sizes. (a) 1 by 1 mm, (b) 2 by 1 mm and (c) 4 by 1 mm

4.7. Open Hole Tension Prediction by Using Stochastic Field of X_T

Size effect of fiber direction tension strength (X_T) in unidirectional composites has been established and measured by using specially tapered unidirectional coupons shown in Figure 24. This effect is critical for accurate prediction of the open hole strength of composite laminates. Due to unstable fiber failure mode in quasi-isotropic and fiber dominated laminates it is possible to predict OHT strength by using appropriate failure criteria, such as the Critical Failure Volume (CFV) criterion [6], which take the scaling effect into account. It is, however, not the case with deterministic CDM methods described in the DPFF section. Despite the presence of the second parameter, namely the fracture toughness in the fiber direction G_{XT} the predictions where the tensile strength X_T is not scaled up to smaller volumes under predicts the OHT strength. The results of such prediction are shown in Table 3 and compared to both the CFV prediction and the experiment. These simulation results are comparing to matching experiments performed in [6] using the updated mesh that will be discussed later in this section.

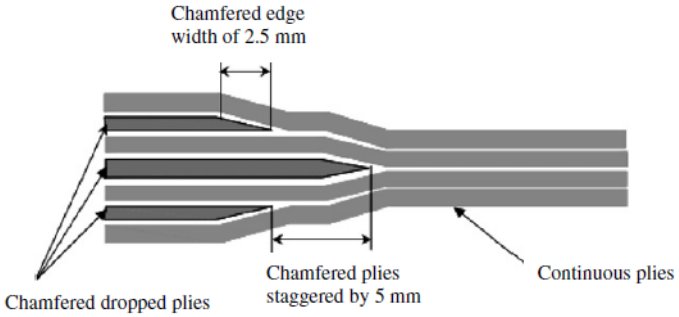

Figure 24. Specially tapered coupons for fiber direction tensile strength size effect measurement from [36]

Table 3. Comparison of deterministic and statistical OHT strength prediction.

	Experiment	CFV	Normal Strength CDM
N	3	1	1
Input X_T (MPa)	---	2905	2905
Strength (MPa)	554	544	427
% Error from Experiment	---	-1.8%	-23.0%

The capability of introducing random distribution of fiber direction strength which is scaled according to Weibull distribution in the manner consistent with CDM provides a possibility to effectively apply volume strength scaling to CDM simulation. Spatial distribution of the tensile strength X_T for two different seed sizes randomized according to Eq (30) is shown in Figure 25. The colors in the two different plots in Figure 25 represent a relative strength scaling factor that is also relative to the individual special distribution. Red indicates higher strength while green represents lower strength. As expected, the distribution with smaller seed size appears less structured.

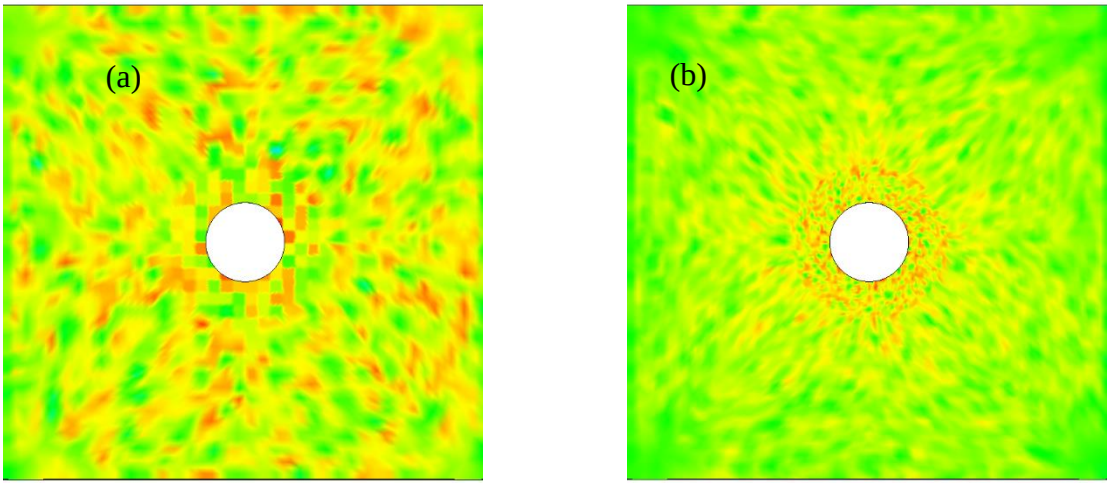

Figure 25. Stochastic seeding of fiber direction strength, 1 mm x 1 mm x 0.127 mm (a), 0.27 mm x 0.27 mm x 0.127 mm (b) seed size.

An example of two different realizations of the fiber-direction tensile strength is shown on Figure 26. The realizations are visually very similar, and it illustrates the quasi-random nature of computer-generated random number strings. While these may appear quite similar, the resulting failure patterns and strengths may be quite different. The failure patterns for the plies shown in Figure 26 are shown in Figure 27. In Figure 27, blue areas represent CDM fiber failure while the thin orange lines represent mesh-independent cracks. Realization A and B produce different failure patterns for CDM, with Realization B having a more-tortured fiber failure path and higher strength. In both cases, CDM tends to stall at areas seeded with high strength and uses the matrix cracks to move the CDM path away from a stronger area. The typical fiber failure in quasi-isotropic laminates loaded in tension is generally not visible until just before or at final failure. However, in these simulations, quasi-stable fiber failure growth was observed on one side of the hole of realization A and on both sides of the hole on realization B and well before final failure.

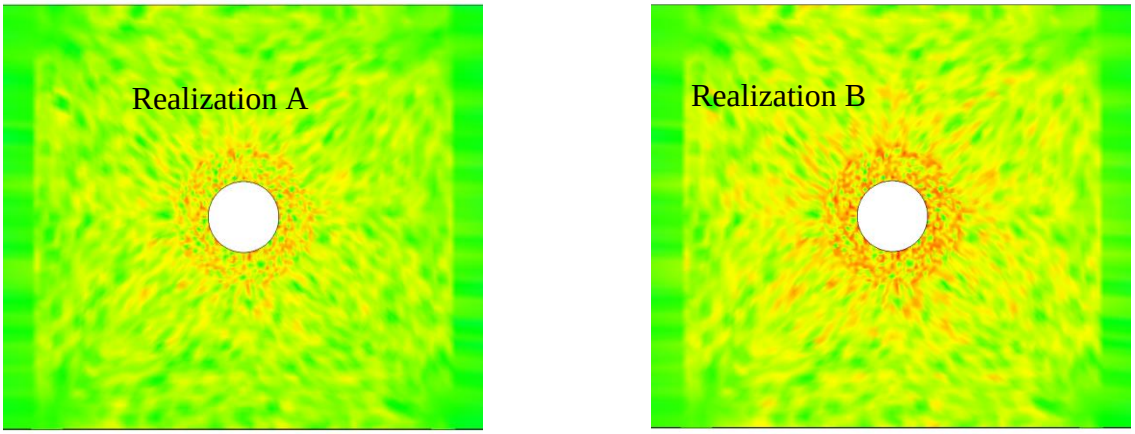

Figure 26. Two different seeding realizations with 0.27mm x 0.27mm x 0.127mm seed size.

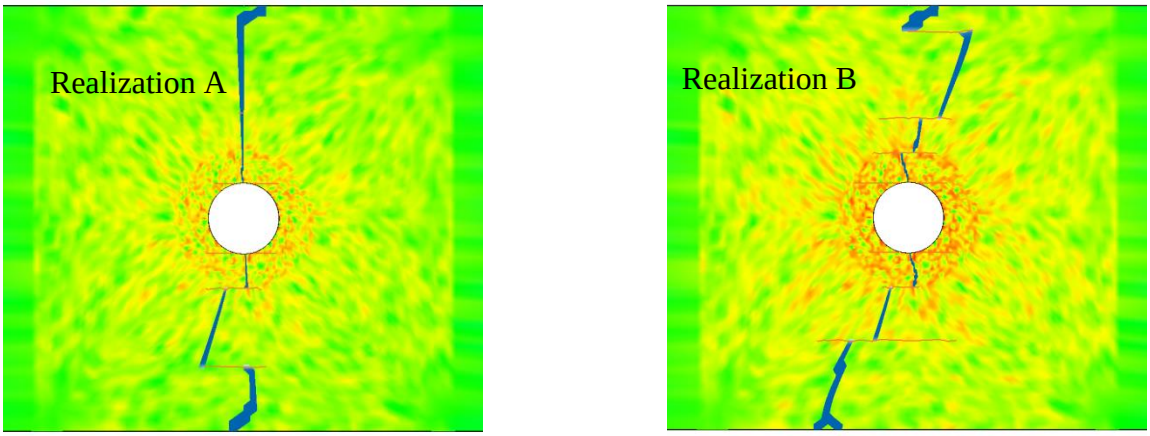

Figure 27. Failure patterns for realizations A and B using the small seeding window, corresponding to 457 MPa and 503 MPa tensile strength respectively.

An attempt was made to reproduce an accurate prediction of the experimental average strength using two different seed volumes. The finite element mesh for these OHT simulations is shown in Figure 28. Element sizes range from approximately 0.1 mm near the hole edge up to over 6 mm at the ends of the specimen. These simulations utilized properties and boundary conditions as described in [6] but using a different mesh. To reduce the model size, mid-plane symmetry was used to reduce the number of modeled plies from 16 to 8. Since the finite element mesh is different and much development work has occurred since [6] was published, a CFV and deterministic CDM model were developed and simulated. Those results are shown in Table X. Two sets of 5 stochastic models were simulated using different seed volume sizes. Both volumes used the ply thickness of 0.127 mm as the seed thickness and otherwise had a square cross-section with side lengths of 0.27 mm and 1.00 mm, respectively. The two different seed volumes were chosen to see if there were size effects at those scales. It should be noted that 0.27 mm is very close to the characteristic length of 0.266 mm used by the CFV method for failure initiation.

A second deterministic CDM model was performed as well that used Weibull's scaling of strength equation to the smallest volume size used in the stochastic models and specified that strength as X_T.

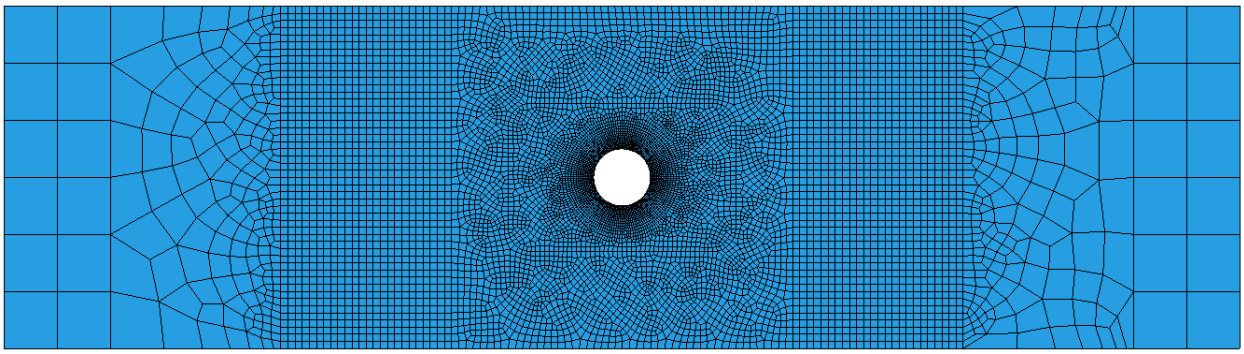

Figure 28. Finite Element Mesh used for deterministic and stochastic OHT strength predictions.

The results from the simulations described previously as well as the experiment strength are shown in Table 4. The input fiber-direction tension strength is included to indicate the scaled strength value in the Scaled Strength CDM case. The Strength value is either the mean value from multiple simulations or experiments (N > 1) or the resulting strength from a single prediction (N = 1). By taking the Weibull-scaled strength based on equation (9) in [3] and using it as the input strength, the CDM prediction improved significantly and was just over 5% less than the experiment value. This seems to indicate that simple strength scaling improves the prediction but is not as capable of predicting failure as the CFV method. Compared to deterministic CDM with the nominal X_T the stochastic methods indeed significantly increase the mean predicted strength. These strengths are still significantly less than the CFV predicted strength. The CDM and matrix crack patterns for all five realizations of the small seed size are shown in Figure 29. These damage patterns demonstrate the different damage patterns produced through the stochastic CDM method.

Table 4. OHT strength prediction by using uniform and stochastic X_T distribution

	Experiment	CFV	Normal Strength CDM	Scaled Strength CDM	Stochastic CDM, 0.27 mm seed size	Stochastic CDM, 1.00 mm seed size
N	3	1	1	1	5	5
Input X_T (MPa)	---	2905	2905	3936	2905	2905
Strength (MPa)	554	544	427	526	478	468
% Error from Experiment	---	-1.8%	-23.0%	-5.1%	-13.7%	-15.5%

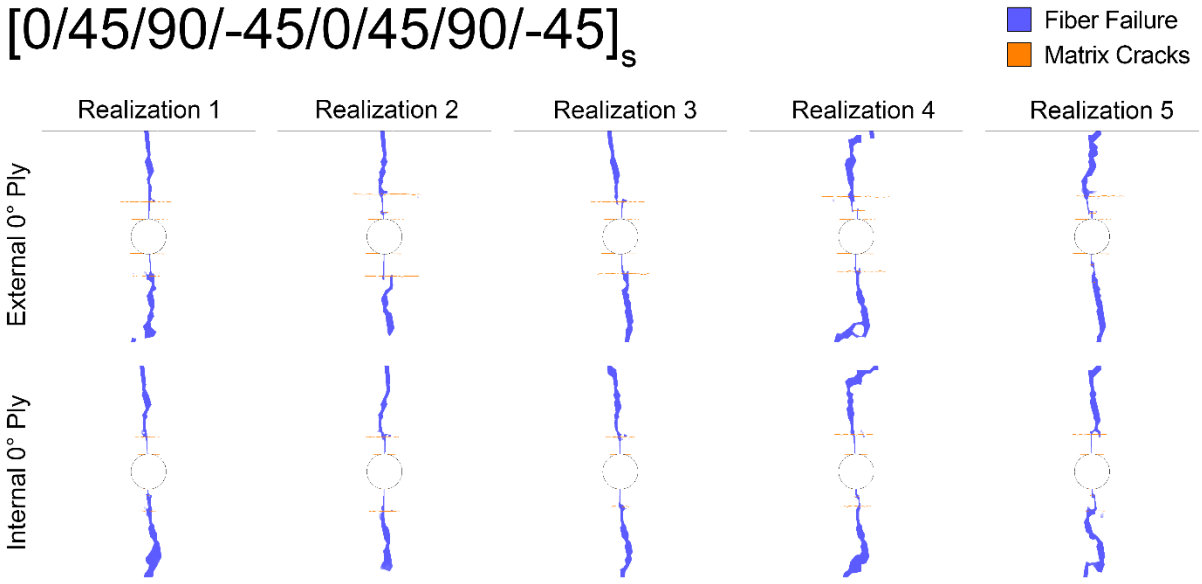

Figure 29. Failure patterns for the external and internal 0° plies for the small seed size simulations.

5. Development of the measurement and analysis technique characterize input parameters governing compression fiber failure

5.1. Notched Four Point Bend Tests

The notched four-point bending test is a pure bending test of a uni-directional beam of 0.5 in. thick by 6 in. long. At the gauge section, the specimen has a notch of depth 0.25-0.26 in. The notch is produced with a grinder using decreasing wheel tip sizes. See Figure 3 for overall specimen dimensions. The crack tip is shown here under a microscope, magnification x1000. The notch radius is approximately 11 μm for each specimen. This sharpness is known to give good results [25].

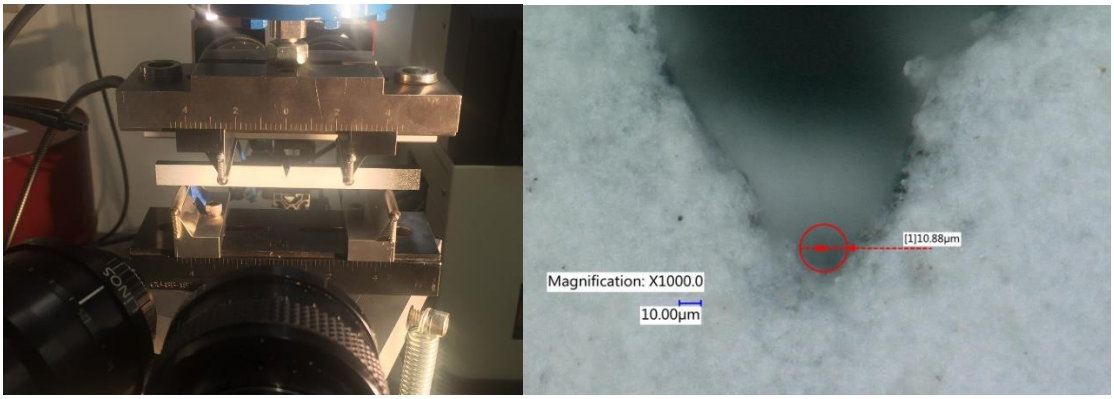

Figure 30: Notch Tip for Notched Four-Point Bending Specimen

By loading the specimen this way, the damage starts right at the crack tip. It starts with an initial visible surface crack, well before a load drop is seen. Later, audible cracks hint at internal damage. The surface crack goes straight down from the crack tip but is paired with delamination of the surface plies. The load drop comes much later. CT-reconstructions taken at every 50 lbf reveal that there are significant 3D effects into play. The outer plies fail under pure compression but also completely delaminate from the inner plies. The inner plies develop a shear crack at a 45° angle. Final failure comes early due to global buckling, as the entire specimen bends out of plane. Figure 33 shows how compressive stresses are very high at the crack tip, but shear stresses are very high at a 45° angle.

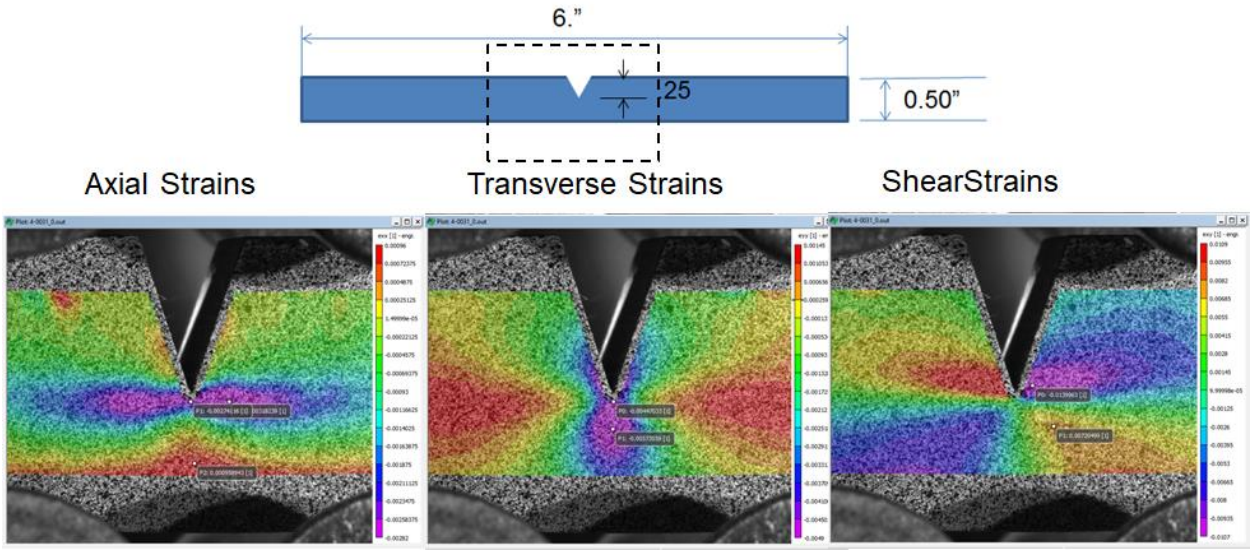

Figure 31. Strain Fields at the Notch Tip as Measured by DIC

The goal is to isolate ply compression cracking. Due to the many facets of this type of failure, the test was redesigned, such that each specimen was cut into very thin slices approximately 0.015 in. wide. This removes plane strain effects to create a 2D stress field and removes the possibility of creating delaminations or crack variations through the width. The difficulty with thin slices is that they cannot be loaded on their thin sides. The newly designed specimens have Plexiglas skins bonded to the specimen for stability, as shown in Figure 32. These Plexiglas skins are not connected in the gauge section – load transfer can only go through the specimen. To prevent the out-of-plane buckling, two layers of Plexiglas front and back act as a clamp to hold the left and right halfs in-plane. This greatly increases stability. The screws are tightened loosely, but potentially increase the overall specimen stiffness.

The test of the new thin specimens has very straight-forward results. CT-reconstructions show the crack grows straight down the cross-section under pure compression, and there is no variation across the width of the specimen. The growth of the crack is also clearly visible on the load-displacement graph. Due to small variations in width, the hand tightening of the clamp, and slight misalignments in the Plexiglas skins, the load-displacement curves show a lot of scatter between the specimens.

High-magnification X-ray CT reconstructions show detail on the failure phenomena in compression. Figure 33 shows two planes of the reconstruction, in which a kink band is visible. The kink band is a complex shear-compression failure and appears to be only a few microns wide. Better understanding of this failure mode could prove meaningful in developing more accurate failure prediction tools or better composite materials for high strength.

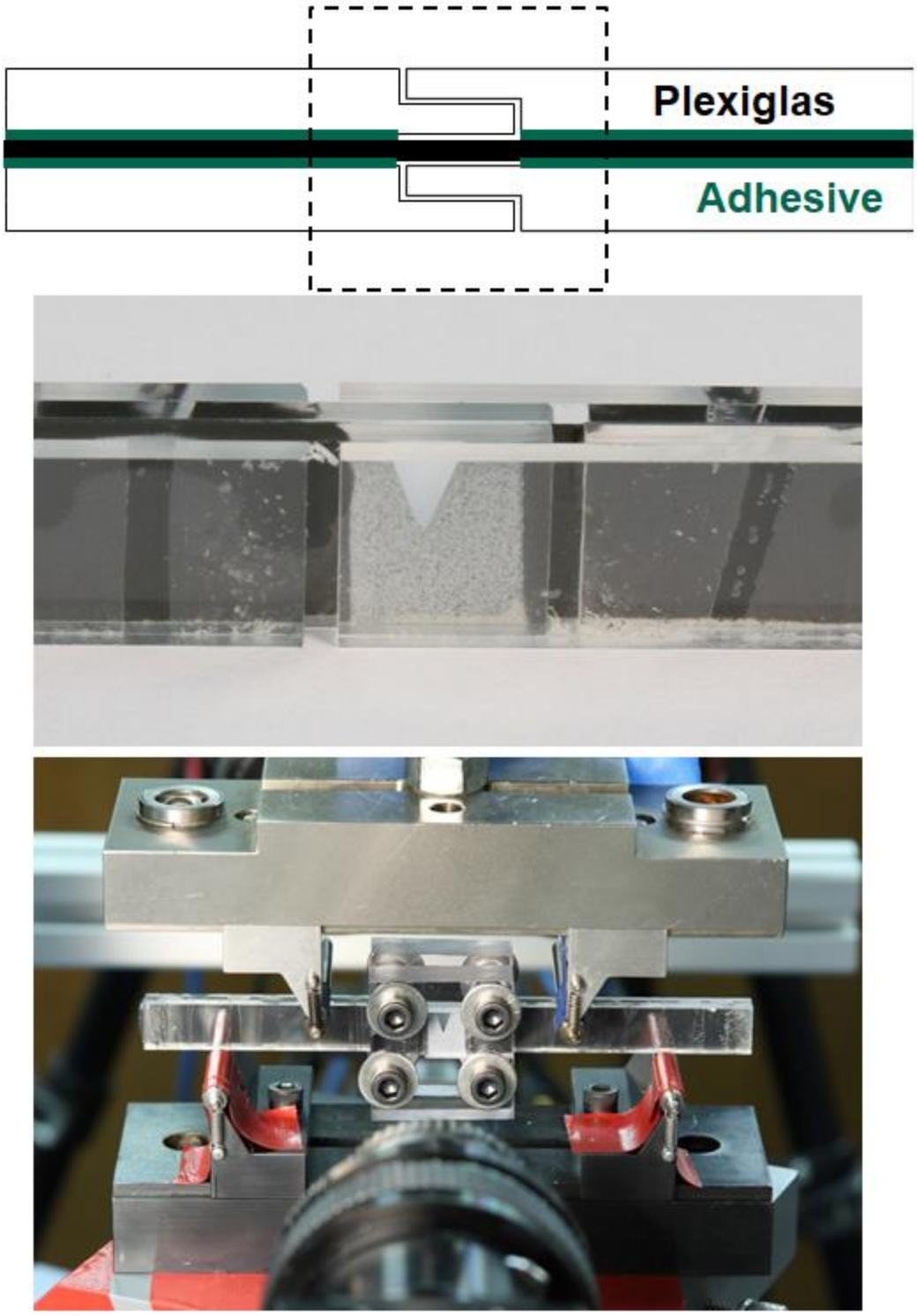

Figure 32. Thin Slice Notched Four-Point Bend Specimen Design and Test Configuration, including Plexiglas Clamp

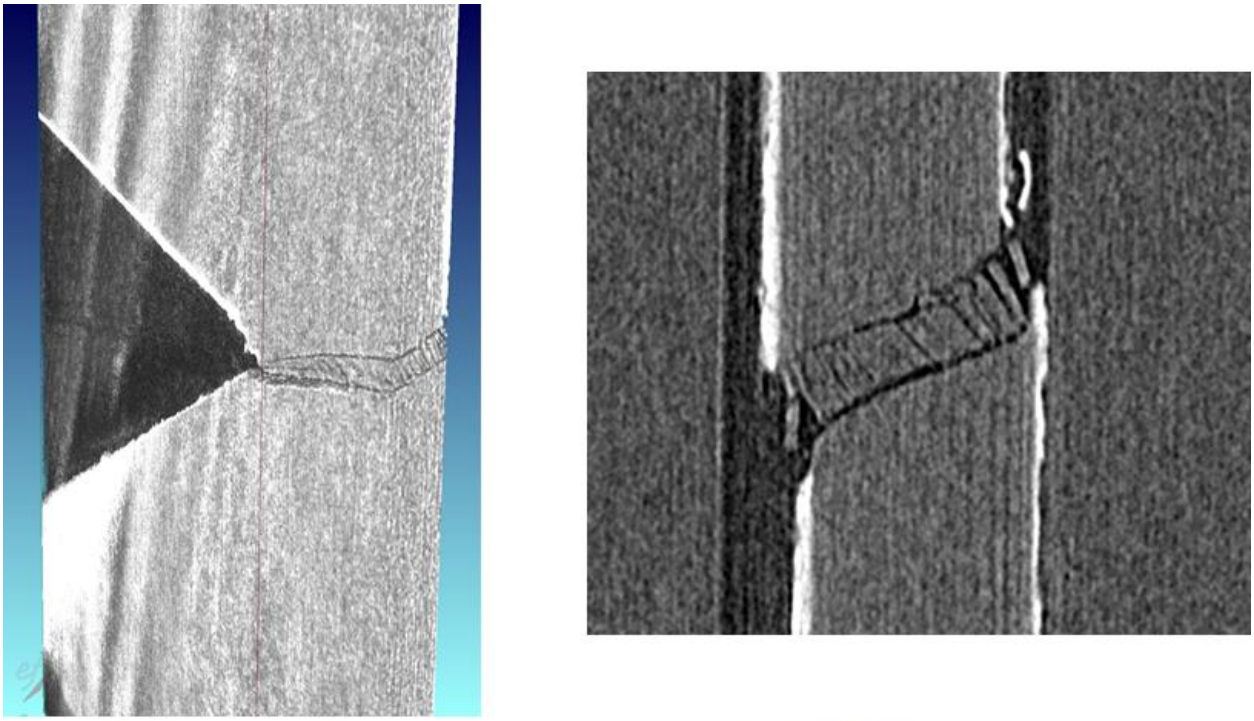

Figure 33. Kink Band Visualization by CT Reconstruction in Notched Four-Point Bend Specimen

5.2. Four Point Bend (4PB) Simulations for Compression Fiber Failure

5.2.1. Initial Thick Specimen Modeling

Model & Boundary Conditions

The initial specimen boundary conditions are shown in Figure 34. The simulation represents a notched four-point bend (4PB) specimen with 36 plies through the thickness for a nominal thickness of 0.26 inches. The simulation was slightly larger than the large span size of 4.6 inches and modeled only 18 plies. The simulation assumed that the specimen was perfectly square and the specimen midplane would not change appreciably during the experiment. The specimen height is 0.5 inches. A triangular notch is cut approximately 0.25 inches into the specimen. The notch has a radius of 11 µm. To accurately model this notch radius, a highly refined mesh is required at the notch as seen in Figure 34. These elements near the notch can be as small at 2.4 µm along the notch edge.

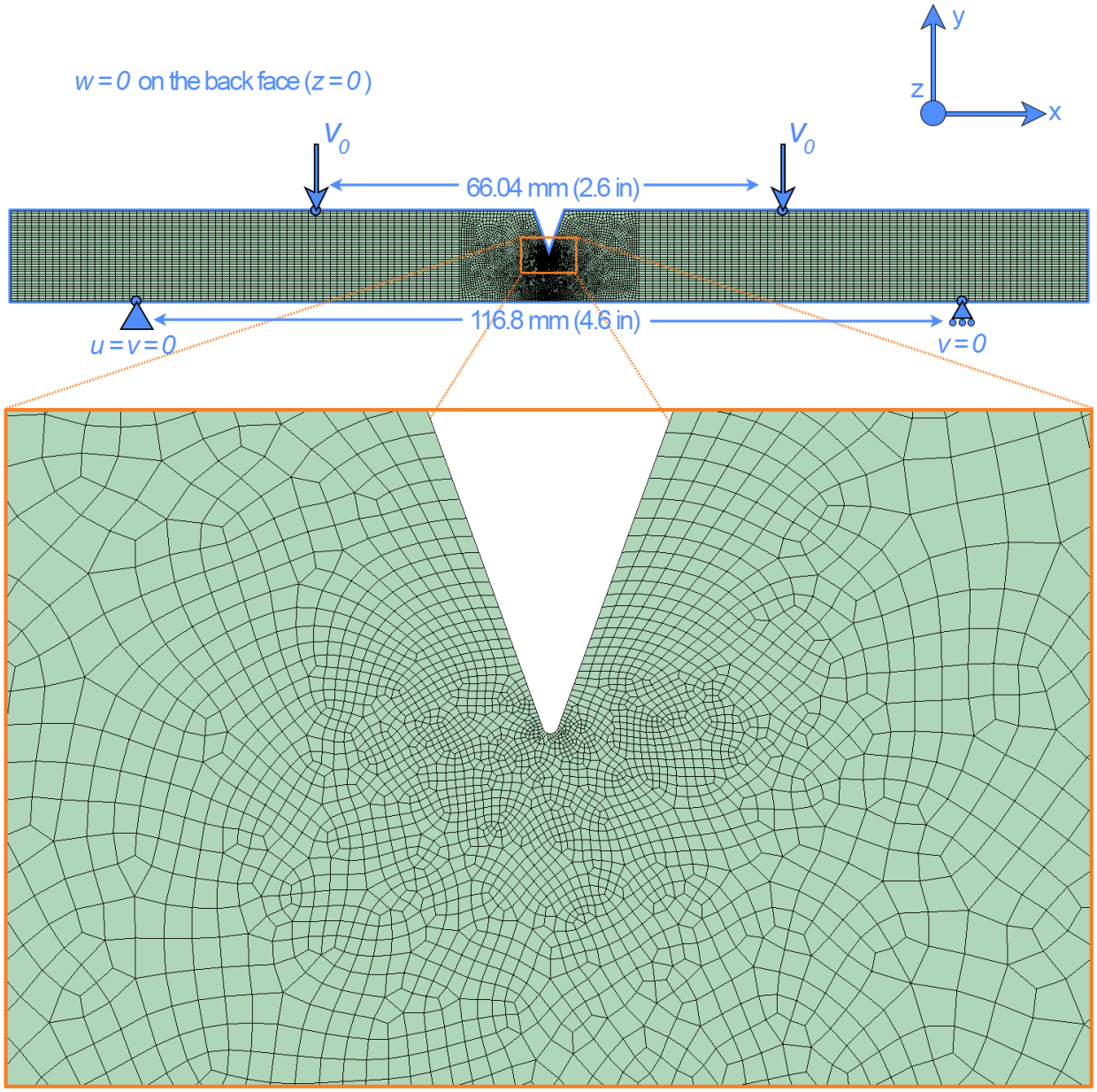

Figure 34. Initial 4PB configuration, boundary conditions, and mesh refinement.

Initial Results & Discussion

Preliminary results from the thick notch specimen are shown in Figure 35. There are many issues with these initial models. There were several attempts at modeling the experiment shown here, but the two simulations shown are bounding cases for the data. It is important to not conclude that some results fell in-between these two and accurately represented the experiment; rather, the results were either near the "BSAM-No Cracks" or "BSAM Geometric Nonlinearity". The sharp increase in load seen in the BSAM no cracks is due to a large, diffuse region of fiber failure truncating growth. This occurred in every version of the model that used the geometrically linear

formulation of BSAM. Up to 1100 lbf, the standard BSAM model behaves as expected. Adding geometric nonlinearity into the model causes fiber damage to localize as expected from experimental results, but this occurs at a much lower load. Upon further inspection of the experiment it was determined that this configuration did not produce the desired result. This configuration was abandoned and a new configuration was developed.

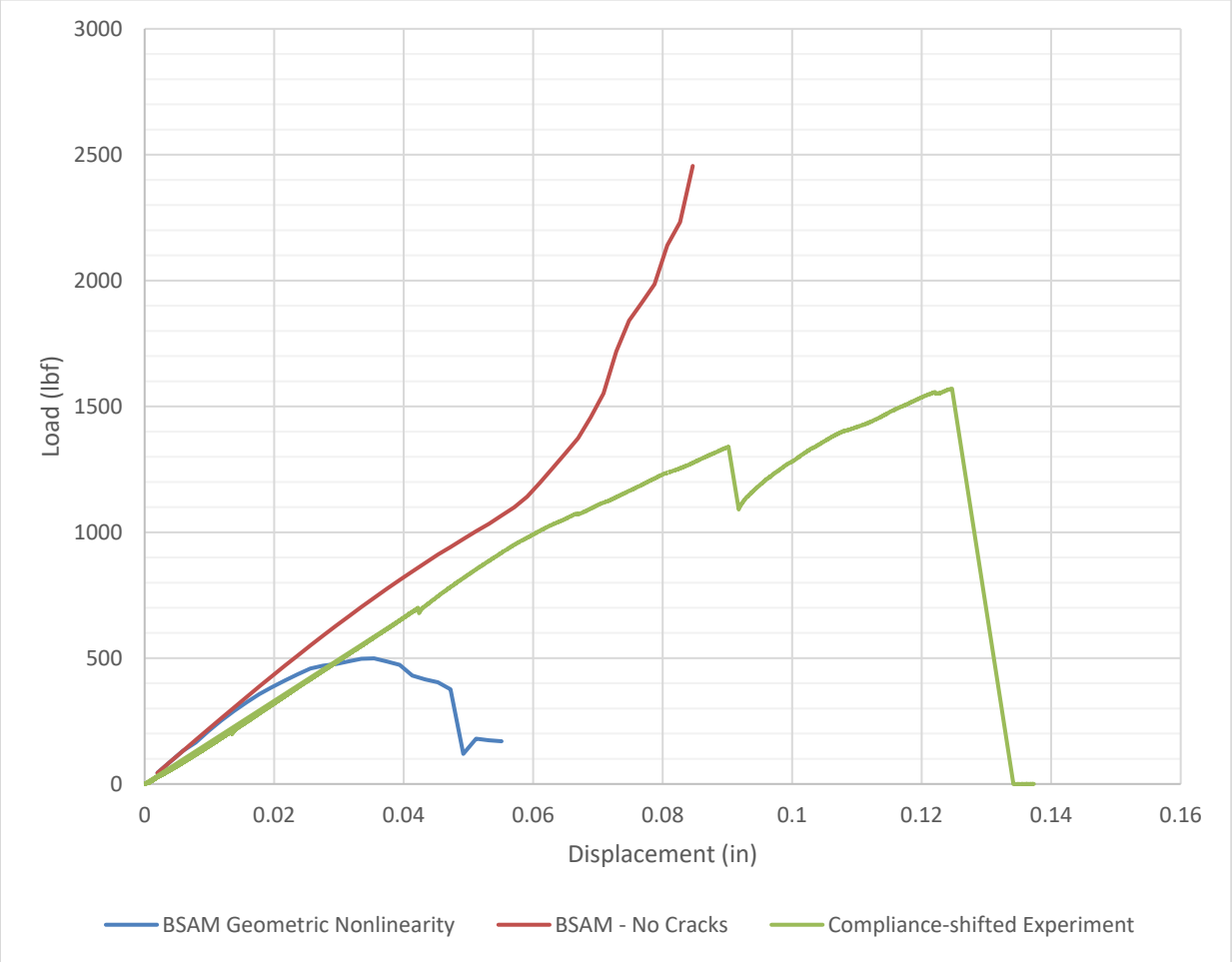

Figure 35. Initial thick specimen experiment and simulation results.

5.2.2. Initial Thin Specimen Modeling

Model and Boundary Conditions

The new specimen utilized thin slices of unidirectional specimens. Nominally, the specimen was the same as the thickness as far as specimen dimensions other than specimen thickness. Nominally, the new specimen is 0.015 in thick. Figure 36(a) shows a top-down view of the specimen configuration. Since the specimen is very thin, Plexiglas guides were bonded onto the thin specimen surfaces away from the central notch region. The guides are still present in the

notch region, but the guides are not bonded to the specimen. Figure 36(b) shows the test specimen in the loading fixture. A Plexiglas clamp is applied across the central unbonded region to increase specimen stability.

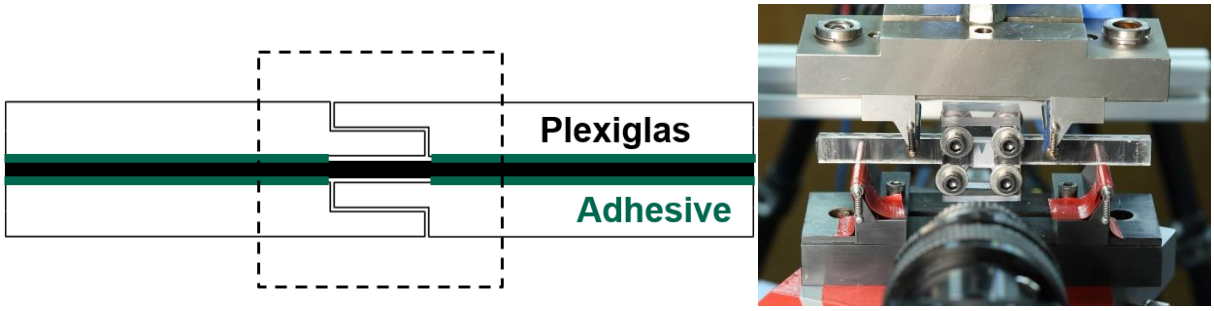

Figure 36. (a) Cross-section diagram of the new specimen configuration and (b) new configuration in the test fixture.

While this configuration produced the desired experimental result, the boundary conditions for the experiment is very complicated. While it would be possible to model the Plexiglas plates on the outside of the specimen it would also be computationally expensive to use a similar mesh to the specimen with many elements through the thickness of each piece of Plexiglas. A further complication is any contact interactions between the Plexiglas and specimen in the notch region. BSAM is capable of modeling contact only using weak cohesive zone surfaces between parts in the model, only if these parts start the simulation in contact, and only in the area where these parts start in contact. This becomes an issue if there are large out-of-plane deformations in the notch region that would interact with the Plexiglas guides. The boundary conditions and whole model is shown in Figure 37. The model uses z-displacement boundary conditions to replicate the behavior of sections where the Plexiglas is bonded to the composite. The specimen is loaded in simply supported four point bending to approximate the roller boundary conditions seen in the experiment.

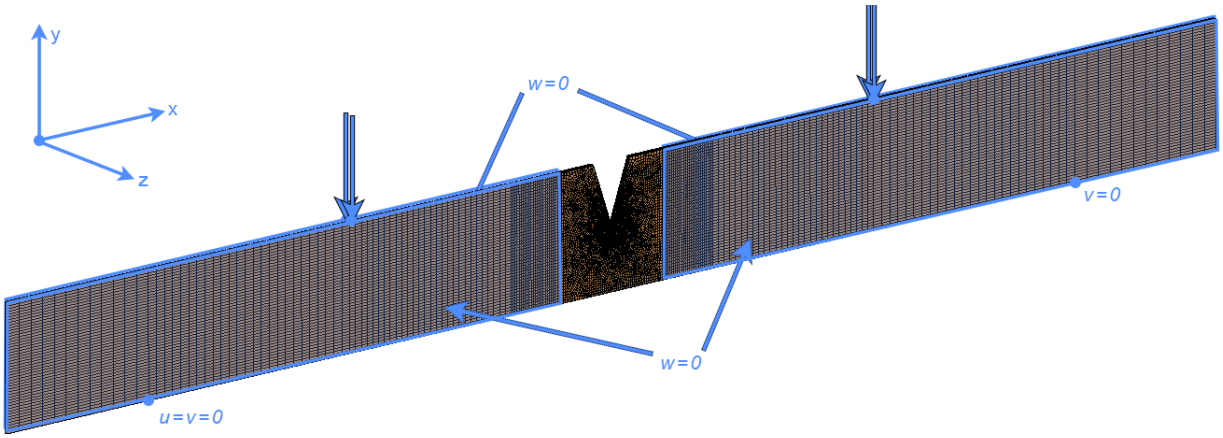

Figure 37. Finite element model and boundary conditions for the thin specimen configuration.

Initial Results & Discussion

The initial simulation used geometric nonlinearity, shear nonlinearity, and continuum damage mechanics for fiber failure with the model above. The load-displacement plot for this compared to an estimated plot of the initial experiment are shown on Figure 38. The experiment response is estimated based on a picture of the load-displacement curve and matches fairly well. The simulation diverged within the first few steps and prior to reaching any kind of interesting behavior from the experiment. After reviewing the file and testing a few different material parameters to see if the behavior could be corrected it became clear that some sort of interaction was occurring within BSAM between the geometric nonlinearity (NLG), the nonlinear shear (NLS), and the Continuum Damage Mechanics (CDM).

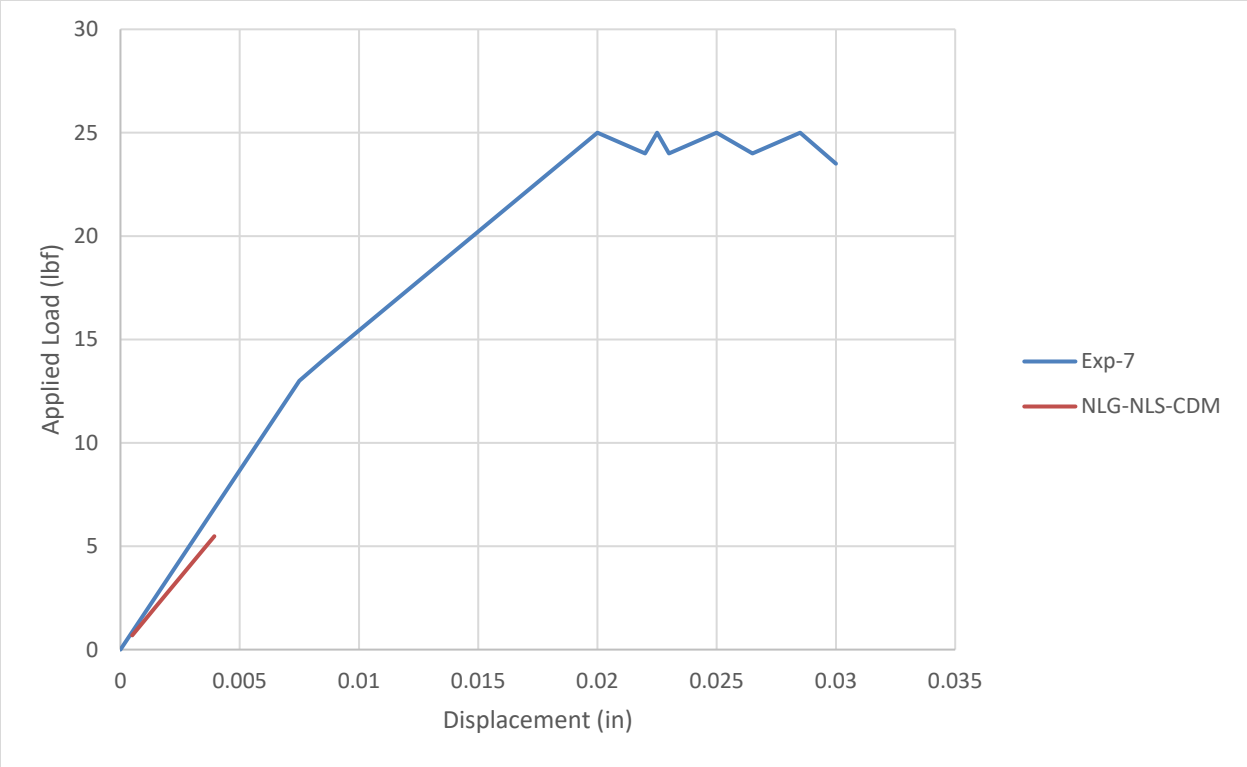

Figure 38. Initial experiment results and first model result for thin slice configuration.

5.2.3. Study of Nonlinear Shear, Continuum Damage, and Geometric Nonlinearity Settings

To study the interactions between these three features within BSAM, three different simulations were performed using different settings for continuum damage mechanics (CDM), geometric nonlinearity (NLG), and nonlinear shear (NLS). The goal was to find a combination of settings that might replicate the experimental behavior that was observed. The results from these three simulations are shown in Figure 39. The first simulation performed was using geometric linearity, linear shear, and continuum damage (LG-LS-CDM). This simulation ran through the specified steps without failure and significantly overpredicted the maximum applied load. The second simulation performed used geometric linearity with nonlinear shear and continuum damage (LG-NLS-CDM). This simulation also overpredicted the strength significantly but did reduce the final load from 62 lbf to 57 lbf.

The third simulation removed the continuum damage but used geometric nonlinearity and nonlinear shear (NLG-NLS). This combination of settings produced a result with a maximum load of 30 lbf and had similar behavior to the initial experiment based on load-displacement behavior. Figure 40 shows the results from the final simulation load step on the left and the last experiment image prior to stopping the experiment on the right. In-plane shear strain is used to visualize failure, with the bounds of the shear strain contour at -50% and +50%. The behavior is similar with the experiment producing a larger crack at a lower applied displacement.

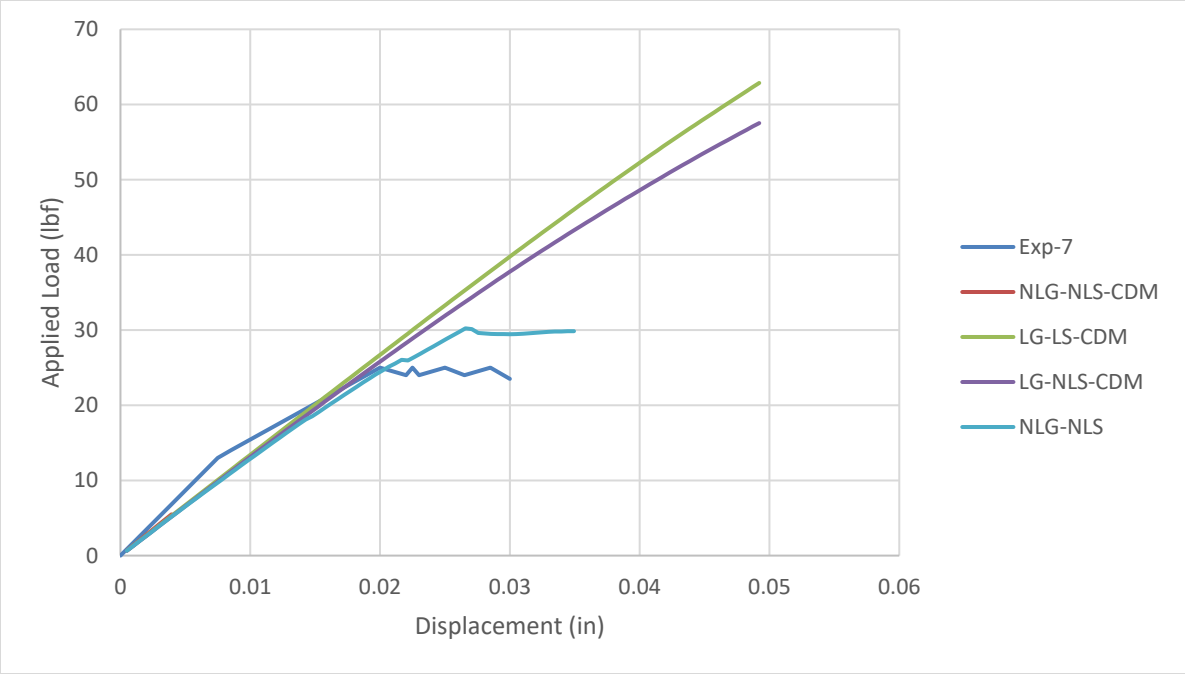

Figure 39. Load-displacement results for different settings of nonlinear shear, continuum damage, and geometric nonlinearity compared to initial experiment.

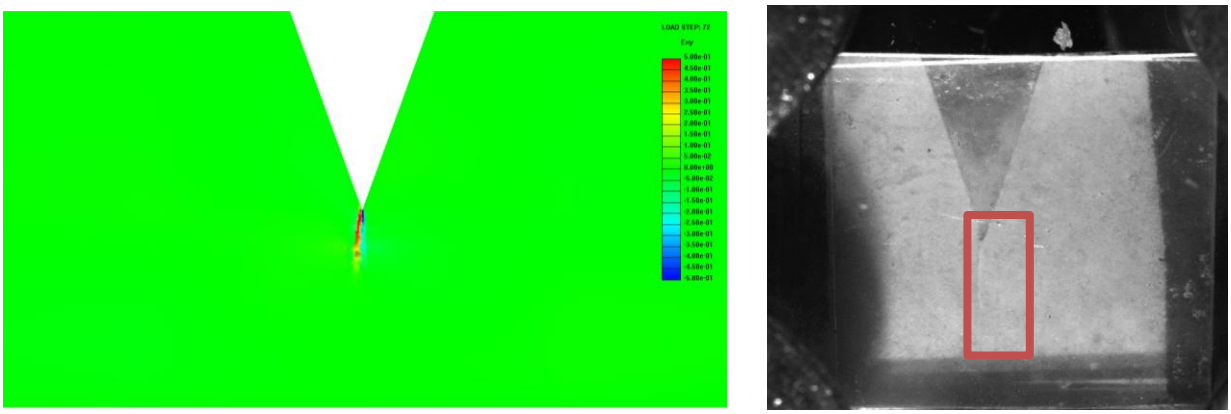

Figure 40. (a) final "crack" shown from simulation and (b) final crack in experiment prior to failure (highlighted in orange box).

5.2.4. Effects of Fiber Orientation

One potential source for differences between the experiments and simulation is the fiber angle in the specimen. The assumption in the simulation is that the x-axis is the 0° fiber direction and the fibers are all oriented in that direction. It is possible that the experiment may have global rotations as well as local waviness within the carbon fibers. To interrogate this possible difference, the fiber orientation in the model will be rotated about the y-axis and z-axis as defined in Figure 37. The most likely rotation in the experiment would be about the y-axis since

the y-axis is parallel to the stacking direction of the specimen. Variation of Z-axis rotation would occur based on variation of ply thickness and would likely be small. The fiber orientation within the model were rotated by values of 1, 2, and 5 degrees about those two axes.

Fiber Rotation Results

The results from rotating fiber orientation about the y- and z-axis are shown in Figure 41. Simulations are labeled by the x-axis rotation, y-axis rotation, and z-axis rotation using the notation (x-axis, y-axis, z-axis). Thus, a simulation labeled (0,2,0) represents a simulation with a rotation of 2° about the y-axis from the x-axis. The results indicate that a rotation of 5° was sufficient to produce a significant difference in stiffness and response. A rotation of 5° is quite large in practice, and micrography of the specimen indicate that any rotation is less than 5°. An example micrograph is shown in Figure 42.

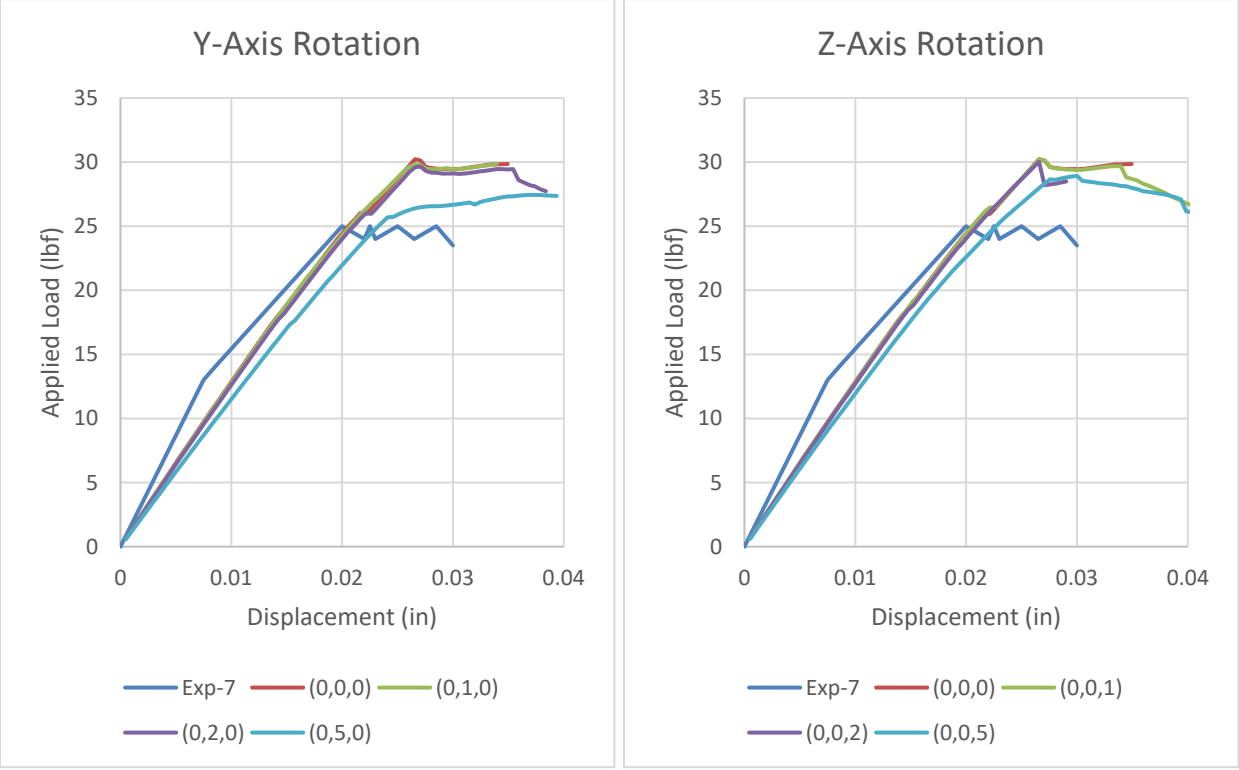

Figure 41. Simulation results for (a) y-axis rotation and (b) z-axis rotation of fiber orientation compared to experiment.

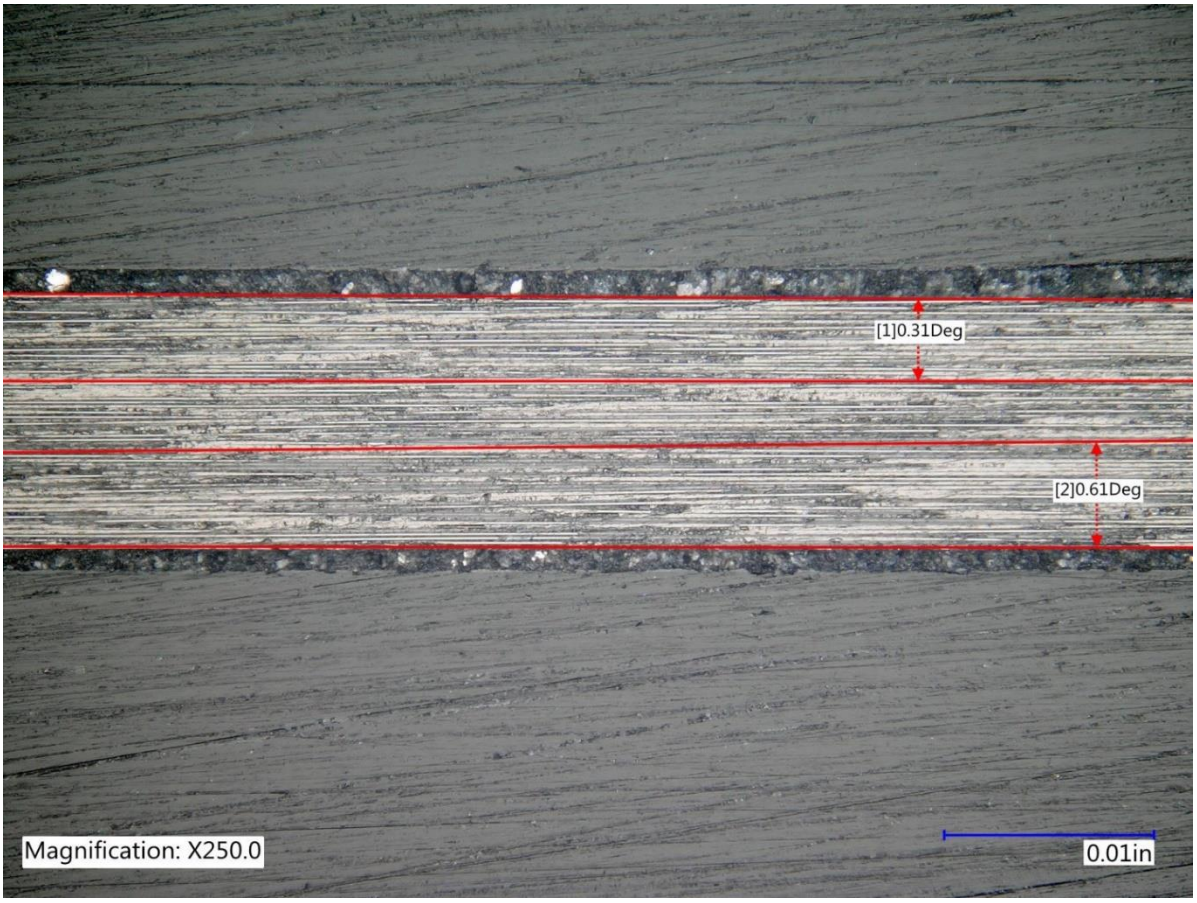

Figure 42. Photomicrograph of fibers in specimen showing alignment with nominal orientation.

5.2.5. Varying simulation thickness to match individual experiments

Other experiments were performed beyond the initial experiment. Measurements of these other specimens indicated a significant variation in the specimen thickness. Beyond just variation in the average thickness of each specimen there is a significant variation of thickness within each specimen. For modeling these other specimens it is necessary to modify the thickness of the mesh. Three different methods are used for modifying the mesh to match the specimen thickness: one is to use the specimen nominal thickness, one is to use the average thickness measured across the gauge (or non-bonded) section, and finally using measured points on the specimen to taper the specimen both along the length and through the height of the specimen. The models used to represent these variations are identical to Figure 37 in boundary condition and mesh with the exception of the z coordinate position of the nodes within the model. For models that utilize the nominal thickness the specimen thickness will be identical across the entire simulation but is an average of the entire specimen. Models that use the gauge thickness will likewise have an identical thickness across the entire specimen. Models using the individual measurements around the specimen will have thickness specified by 9 measurement points across the specimen and use

2-D linear interpolation between points. The modification of these models was performed using a Python script.

For this analysis, the experiment specimens were down-selected from nine experiments down to four. Each of these four specimens may not be used in each section for comparison. Three of the specimens are removed due to lack of data in certain aspects: 7, 11, and 12. Specimen 7 was used for comparison earlier and exhibited different behavior than all other specimens discussed from here forward. Specimens 11 and 12 lacked any thickness data beyond the nominal thickness information and thus were not analyzed. The remaining six specimen results are plotted in Figure 43. Figure 43(a) is a plot of the raw load-displacement data. The stiffnesses vary based on the variation in the thickness of the specimen. To account for this thickness difference, the values were normalized based on the nominal thickness of each specimen as a selection criteria. Figure 43(b) shows the plots of load-displacement when the load is normalized based on thickness. This normalization is performed by taking the load and dividing by the ratio of the nominal thickness to the maximum nominal thicknesses of all specimens. There is a group of four specimens that show similar behavior, and two specimens that behave similar to each other but different from the other four. These two specimens (18 and 25) are excluded from this analysis. There is a possibility that there is some other experiment factor that caused 18 and 25 to differ from the other four specimens.

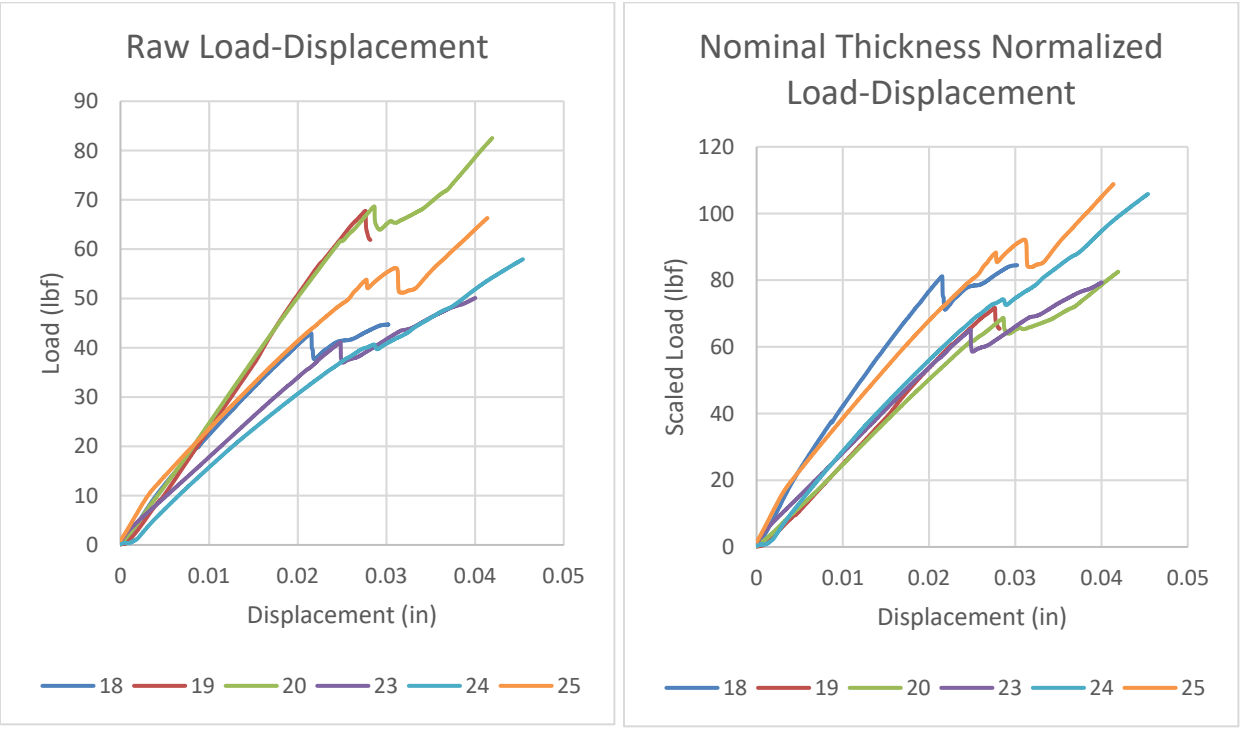

Figure 43. (a) Plot of all 6 experiments with complete data and (b) same results as (a) with normalized load data.

Simulation Results and Discussion

The four remaining specimen configurations (19, 20, 23, and 24) were modeled using at least one of the thickness specifications mentioned previously. Specimen 19 and 23 were modeled using gauge thickness average and taper, Specimen 20 was modeled using nominal thickness and taper, and Specimen 24 was modeled using taper only. The results from the simulations compared to experiments are shown in Figure 44. Simulations are noted using the prefix "BSAM". The type of simulation is specified based on the suffix: "G" for average gauge thickness, "N" for nominal thickness, and "T" for taper. For example, in Figure 44(a) "19" refers to the experimental result for specimen 19, "BSAM19G" corresponds to the gauge average thickness model simulation for specimen 19, and "BSAM19T" refers to the tapered model simulation for specimen 19. For each plot, the solid line is the experiment data, the dashed line is either the gauge or nominal thickness simulation, and the dotted line corresponds to the tapered simulation. In all cases, the experiment appears to be stiffer than the simulations. This was expected given the differences between the experimental setup and the boundary conditions of the model. In most cases, the first peak load of the simulation accurately predicted the experiment first peak load. Post-peak load behavior was similar between model and experiment except for specimen 24 shown in Figure 44(d).

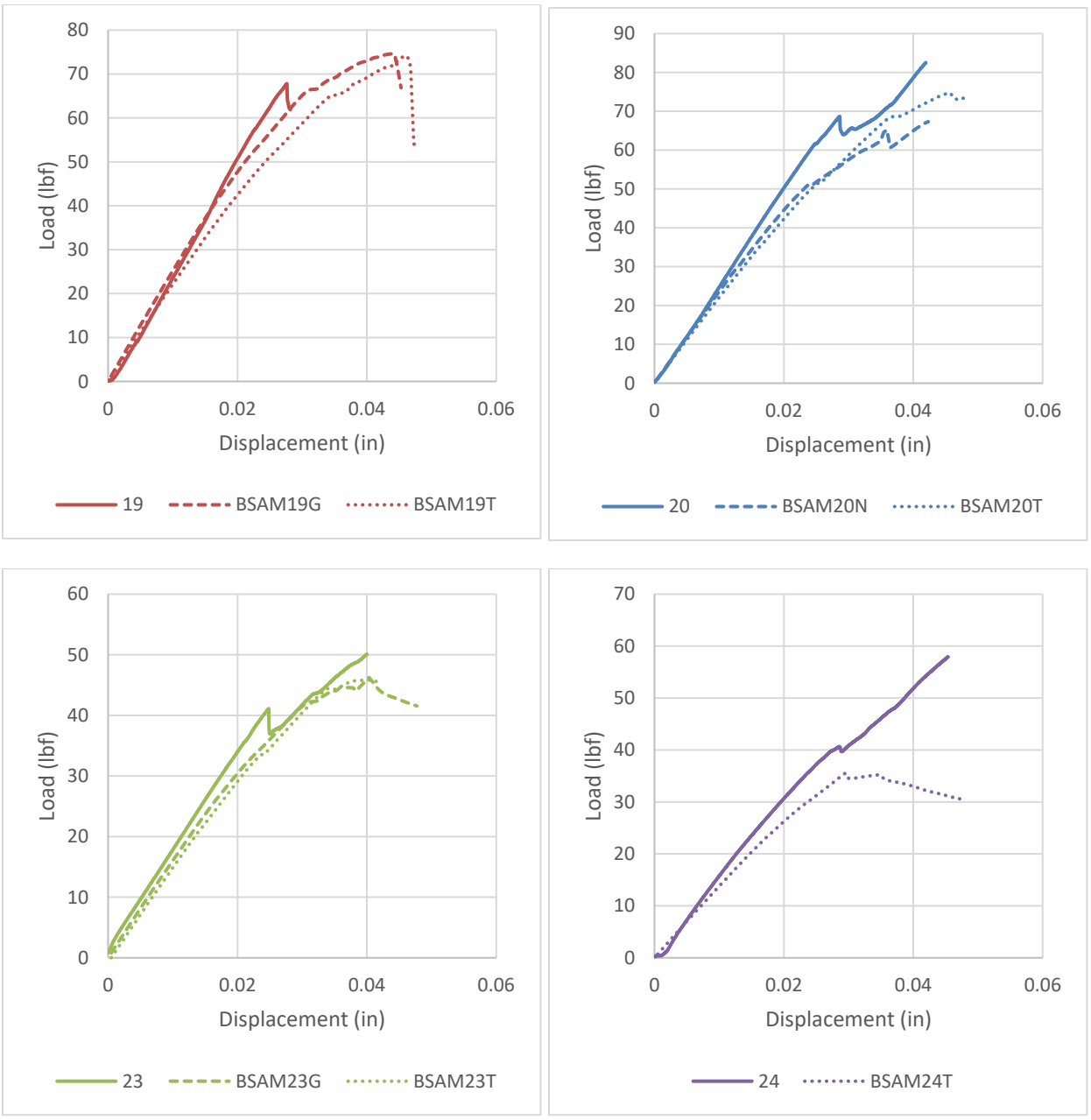

Figure 44. Load-displacement comparisons for specimens (a) 19, (b) 20, (c) 23, and (d) 24.

For specimen 20, the crack length was measured at various times during the experiment. Attempts were made to replicate this measurement in BSAM using the tapered model and those results are shown in Figure 45. The crack length was measured for the model using modeler interpretation of displacement discontinuity in the model. Since nonlinear shear produced the "fiber failure" observed in the models here, there is no definitive damage variable or threshold that specifies failure objectively. The model predicts the crack growth accurately up until the first load drop in the experiment around 68 lbf, where the model does not replicate this large unstable growth.

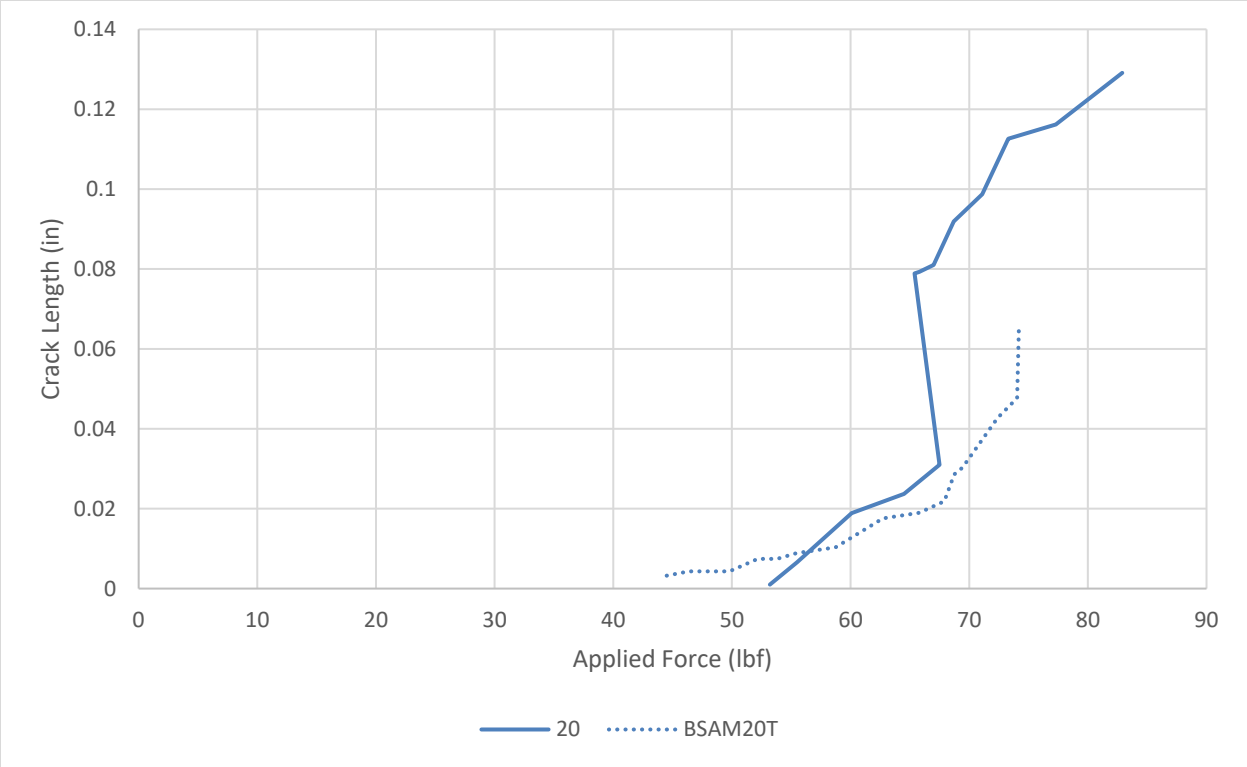

Figure 45. Crack length - load comparison between experiment and simulation for specimen 20.

REFERENCES

[1] T. A. Sebaey, J. Costa, P. Maimí, Y. Batista, N. Blanco, and J. A. Mayugo, "Measurement of the in situ transverse tensile strength of composite plies by means of the real time monitoring of microcracking," *Compos. Part B Eng.*, 2014, doi: 10.1016/j.compositesb.2014.02.001.

[2] H. K. Adluru, K. H. Hoos, and E. V. Iarve, "Discrete damage modelling of delamination migration in clamped tapered laminated beam specimens," in *32nd Technical Conference of the American Society for Composites 2017*, 2017, vol. 2, pp. 917–930, doi: 10.12783/asc2017/15240.

[3] T. K. O'Brien, A. D. Chawan, K. DeMarco, and I. Paris, "Influence of specimen configuration and size on composite transverse tensile strength and scatter measured through flexure testing," *J. Compos. Technol. Res.*, 2003, doi: 10.1520/ctr11003j.

[4] ASTM, "D3039/D3039M-17: Standard Test Method for Tensile Properties of Polymer Matrix Composite Materials," *Annual Book of ASTM Standards*, vol. 15. 2017.

[5] E. V. Iarve, M. R. Gurvich, D. H. Mollenhauer, C. A. Rose, and C. G. Dávila, "Mesh-independent matrix cracking and delamination modeling in laminated composites," *Int. J. Numer. Methods Eng.*, vol. 88, no. 8, pp. 749–773, 2011, doi: 10.1002/nme.3195.

[6] K. Hoos, E. V. Iarve, M. Braginsky, E. Zhou, and D. H. Mollenhauer, "Static strength prediction in laminated composites by using discrete damage modeling," *J. Compos. Mater.*, vol. 51, no. 10, pp. 1473–1492, 2017, doi: 10.1177/0021998316651986.

[7] M. J. Swindeman, E. V. Iarve, R. A. Brockman, D. H. Mollenhauer, and S. R. Hallett, "Strength prediction in open hole composite laminates by using discrete damage modeling," *AIAA J.*, 2013, doi: 10.2514/1.J051773.

[8] E. V. Iarve and K. H. Hoos, "Simulating Fatigue Damage in Laminated Composite Structures," 2014.

[9] E. V. Iarve, K. Hoos, M. Braginsky, E. Zhou, and D. H. Mollenhauer, "Progressive failure simulation in laminated composites under fatigue loading by using discrete damage modeling," *J. Compos. Mater.*, vol. 51, no. 15, pp. 2143–2161, 2017, doi: 10.1177/0021998316681831.

[10] A. Makeev, G. Seon, Y. Nikishkov, D. Nguyen, P. Mathews, and M. Robeson, "Analysis methods for improving confidence in material qualification for laminated composites," *J. Am. Helicopter Soc.*, vol. 64, no. 1, 2019, doi: 10.4050/JAHS.64.012006.

[11] G. Seon, A. Makeev, J. Cline, and B. Shonkwiler, "Assessing 3D shear stress-strain properties of composites using Digital Image Correlation and finite element analysis based optimization," *Compos. Sci. Technol.*, vol. 117, pp. 371–378, 2015, doi: 10.1016/j.compscitech.2015.07.011.

[12] A. Makeev, G. Seon, J. Cline, and B. Shonkwiler, "In quest of methods for measuring 3D mechanical properties of composites," *Compos. Sci. Technol.*, vol. 100, pp. 105–112, 2014, doi: 10.1016/j.compscitech.2014.05.026.

[13] G. Seon, A. Makeev, Y. Nikishkov, and E. Lee, "Effects of defects on interlaminar tensile fatigue behavior of carbon/epoxy composites," *Compos. Sci. Technol.*, vol. 89, 2013, doi: 10.1016/j.compscitech.2013.10.006.

[14] Y. Nikishkov, G. Seon, A. Makeev, and B. Shonkwiler, "In-situ measurements of fracture

toughness properties in composite laminates," *Mater. Des.*, vol. 94, pp. 303–313, 2016, doi: 10.1016/j.matdes.2016.01.008.

[15] A. Makeev, "Interlaminar shear fatigue behavior of glass/epoxy and carbon/epoxy composites," *Compos. Sci. Technol.*, vol. 80, 2013, doi: 10.1016/j.compscitech.2013.03.013.

[16] G. Seon, A. Makeev, B. Van Der Vossen, J. Schaefer, and B. Justusson, "DIC data driven methods to verify simplifying assumptions and increase confidence in material properties of laminated composites," in *32nd Technical Conference of the American Society for Composites 2017*, 2017, vol. 2.

[17] S. Ghaffari, A. Makeev, G. Seon, D. P. Cole, D. J. Magagnosc, and S. Bhowmick, "Understanding compressive strength improvement of high modulus carbon-fiber reinforced polymeric composites through fiber-matrix interface characterization," *Mater. Des.*, vol. 193, 2020, doi: 10.1016/j.matdes.2020.108798.

[18] B. C. W. Van Der Vossen and A. Makeev, "Characterization of cohesive zone laws using digital image correlation," in *33rd Technical Conference of the American Society for Composites 2018*, 2018, vol. 2, doi: 10.12783/asc33/25977.

[19] ASTM D2344, "ASTM D2344/D2344M: Standard Test Method for Short-Beam Strength of Polymer Matrix Composite Materials and Their Laminates," *Annu. B. ASTM Stand.*, vol. 3, no. 2, 2003.

[20] ASTM D5528-01, "Standard test method for mode I interlaminar fracture toughness of unidirectional fiber-reinforced polymer matrix composites," *Am. Stand. Test. Methods*, vol. 03, no. Reapproved 2007, 2014.

[21] ASTM D7905, "Standard test method for determination of the mode II interlaminar fracture toughness of unidirectional fiber-reinforced polymer matrix composites," *ASTM*, 2014.

[22] W. P. Seneviratne and J. S. Tomblin, "Adhesive characterization using NIAR-modified KGR extensometer," *SAMPE J.*, vol. 47, no. 5, 2011.

[23] A.-A. S. for T. and Materials, "ASTM D6484: Standard Test Method for Open-Hole Compressive Strength of Polymer Matrix," *Annu. B. ASTM Stand.*, 2014.

[24] A. S. E647, "ASTM Standard Test Method for Measurement of Fatigue Crack Growth Rates," *ASTM Stand.*, vol. 14, no. 2, 2017.

[25] M. J. Laffan, S. T. Pinho, P. Robinson, L. Iannucci, and A. J. McMillan, "Measurement of the fracture toughness associated with the longitudinal fibre compressive failure mode of laminated composites," *Compos. Part A Appl. Sci. Manuf.*, vol. 43, no. 11, 2012, doi: 10.1016/j.compositesa.2012.04.009.

[26] C. G. Dávila, "From S-N to the Paris law with a new mixed-mode cohesive fatigue model for delamination in composites," *Theor. Appl. Fract. Mech.*, 2020, doi: 10.1016/j.tafmec.2020.102499.

[27] R. C. Juvinall and H. Saunders, "Fundamentals of Machine Component Design," *J. Mech. Transm. Autom. Des.*, 1983, doi: 10.1115/1.3258522.

[28] W. Seneviratne, J. S. Tomblin, and S. Kariyawasam, "Analytical Fatigue Life Determination based on Residual Strength Degradation of Composites," in *FAA Joint Advanced Materials and Structures*, 2018.

[29] G. Sendeckyj, “Fitting Models to Composite Materials Fatigue Data,” in *Test Methods and Design Allowables for Fibrous Composites*, 2009.

[30] T. K. O’Brien, W. M. Johnston, and G. J. Toland, “Mode II Interlaminar Fracture Toughness and Fatigue Characterization of a Graphite Epoxy Composite Material,” *Nasa/Tm–2010-216838*, 2010.

[31] A. C. C. Leitão, R. D. S. G. Campilho, and D. C. Moura, “Shear Characterization of Adhesive Layers by Advanced Optical Techniques,” *Exp. Mech.*, vol. 56, no. 3, pp. 493–506, 2016, doi: 10.1007/s11340-015-0111-4.

[32] A. Turon, P. P. Camanho, J. Costa, and C. G. Dávila, “A damage model for the simulation of delamination in advanced composites under variable-mode loading,” *Mech. Mater.*, 2006, doi: 10.1016/j.mechmat.2005.10.003.

[33] S. T. Pinho, C. G. Dávila, P. P. Camanho, L. Iannucci, and P. Robinson, “Failure Models and Criteria for FRP Under In-Plane or Three-Dimensional Stress States Including Shear Non-linearity,” *Nasa/Tm-2005-213530*, 2005, doi: NASA/TM-2005-213530.

[34] P. Maimí, P. P. Camanho, J. A. Mayugo, and C. G. Dávila, “A continuum damage model for composite laminates: Part I - Constitutive model,” *Mech. Mater.*, 2007, doi: 10.1016/j.mechmat.2007.03.005.

[35] P. Maimí, P. P. Camanho, J. A. Mayugo, and C. G. Dávila, “A continuum damage model for composite laminates: Part II - Computational implementation and validation,” *Mech. Mater.*, 2007, doi: 10.1016/j.mechmat.2007.03.006.

[36] M. R. Wisnom, B. Khan, and S. R. Hallett, “Size effects in unnotched tensile strength of unidirectional and quasi-isotropic carbon/epoxy composites,” *Compos. Struct.*, vol. 84, no. 1, 2008, doi: 10.1016/j.compstruct.2007.06.002.

[37] A. Makeev, Y. He, P. Carpentier, and B. Shonkwiler, “A method for measurement of multiple constitutive properties for composite materials,” *Compos. Part A Appl. Sci. Manuf.*, vol. 43, pp. 2199–2210, 2012.

[38] Y. He, A. Makeev, and B. Shonkwiler, “Characterization of nonlinear shear properties for composite materials using digital image correlation and finite element analysis,” *Compos. Sci. Technol.*, vol. 73, pp. 64–71, Nov. 2012, doi: 10.1016/j.compscitech.2012.09.010.

[39] B. Van Der Vossen and A. Makeev, “Characterization of interface shear stress-strain and mode II fracture properties using DIC in thick adherent shear tests,” in *Proceedings of the American Society for Composites - 34th Technical Conference, ASC 2019*, 2019, doi: 10.12783/asc34/31315.

[40] S. Rajan, M. A. Sutton, R. Fuerte, and A. Kidane, “Traction-separation relationship for polymer-modified bitumen under Mode I loading: Double cantilever beam experiment with stereo digital image correlation,” *Eng. Fract. Mech.*, vol. 187, pp. 404–421, 2018, doi: 10.1016/j.engfracmech.2017.12.031.

APPENDIX

Short Beam Shear Static Tests

Test was run on a Shimadzu electromechanical load frame with a 2 KIP load cell. An ASTM D 2344 standard Wyoming Test Fixtures SBS test fixture was used with a 1.2-inch span between the supports. This gave a 4.8 span to thickness ratio which historically gives us optimal data. A custom 4-inch diameter loading nose and 0.125-inch diameter supports were utilized. The tests were conducted at 72°F room-temperature ambient conditions. Test speed was 0.05 in/min. One surface of the specimens was speckled to give a full strain field using DIC. A stereo vision camera set of two 16-megapixel Prosilica cameras were used.

The SBS DIC data-driven experimental method was proposed in [37], [38] and uses the full-field measurements of surface deformation in the specimen to derive the parameters of the constitutive stress-strain equations. It supplements the analysis as prescribed in ASTM D2344, which can only calculate the Short Beam Shear strength as 0.75P/A.

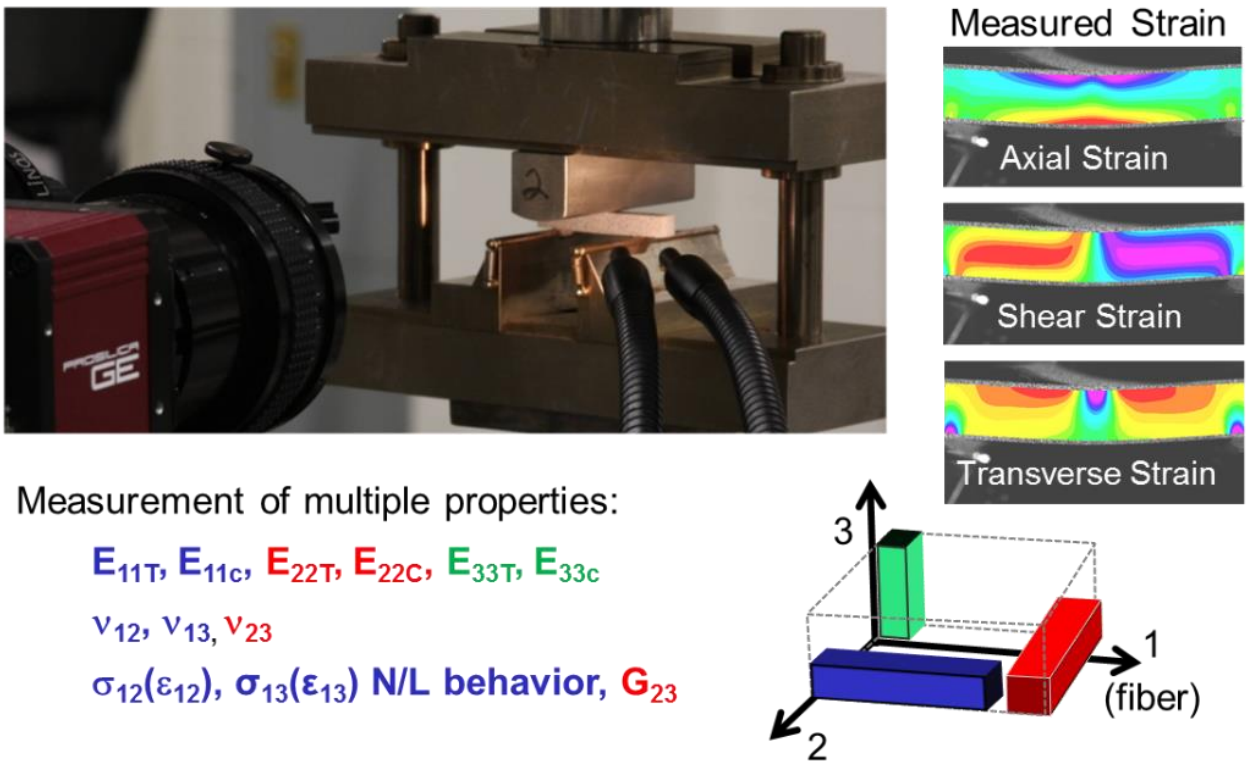

Figure A 1. Testsetup, DIC-measured strains and specimen configurations for the Short Beam Shear (SBS) method allowing measurement of multiple constitutive properties of composites in one single experiment.

By taking measurements of the full-field deformations, the strain components in the longitudinal (1)- direction and transverse (2) or (3)-direction can be quantified. As such, this test method allows for quantification of the tensile/compressive axial modulus, Poisson's ratio, the shear nonlinear stress-strain relationship and the shear strength as well, which are summarized in this report.

For analysis, the area of interest in the DIC full-field measurements is away from the loading nose and supports. In this region, the normal strain components are small enough to be comfortably within the linear regime. By observing a linear distribution of axial strains through the thickness, simple closed-form solutions for the axial moduli and Poisson's ratio are derived [37].

The shear stress-strain behavior away from the contact surfaces is highly nonlinear in the Short Beam Shear specimens. This nonlinear behavior causes a material-dependent solution of stresses within the specimen, for which no closed-form solution is available. In fact, it has been observed that the closed-form stress solution of 0.75P/A significantly overestimates the peak shear stress within the specimen [12], [16], [37], [38]. For common CFRP specimens, this may be as much as 25%. As such, iterative data-driven analysis methods are required to achieve a more accurate solution. The need for an objective and accurate nonlinear stress-strain response is of high importance. From the geometric stress solution combined with DIC shear strain measurements, the initial stress-strain relationship was developed. This approximation was used as a starting point for further refinements using FEA-verified stress correction methods. This leads to a material shear stress-strain relationship which is free of ad hoc assumptions [11].

Error! Reference source not found.A-2 plots the shear stress-strain data for all tested specimens in the 1-2 and 1-3 plane on top of each other. Two of the data sets represent the initial stress-strain approximation using the geometric stress assumption 0.75P/A. The other two data sets represent strain data from the same specimens but are derived from data-driven analysis as per reference [12].

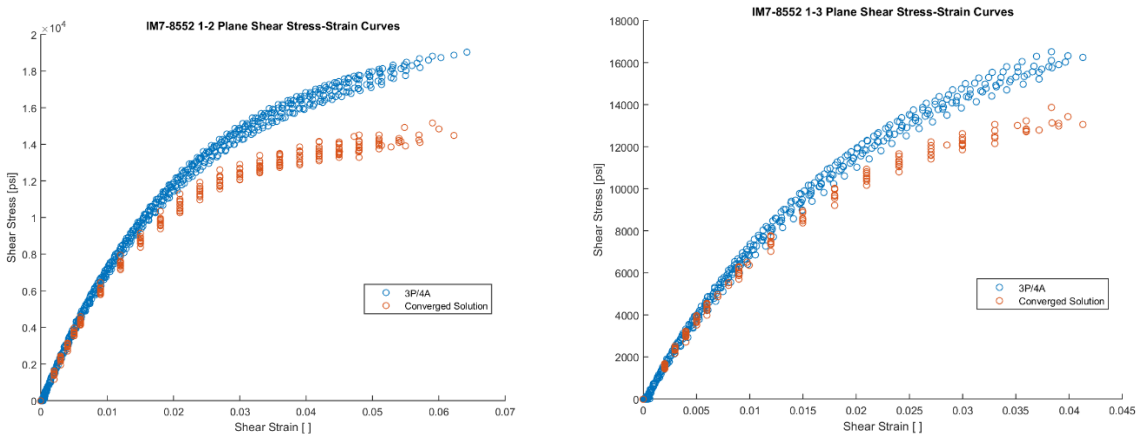

Figure A 2. Shear stress – shear strain data for short beam shear testing in the 1-2 and 1-3 material planes.

A nonlinear least-squares regression analysis is performed to fit the data to the Ramberg-Osgood equation for use in simulations,

$$\gamma = \frac{\tau}{G} + \left(\frac{\tau}{K}\right)^{1/n}$$

Where γ is strain, τ is stress, G is shear modulus, and K and n are material constants. Figure A-3 shows the fit of the regression parameters. Note that the regression analysis is limited to the average shear strength. Even though some specimens exceed that average strength, the Ramberg-Osgood fit is not extended.

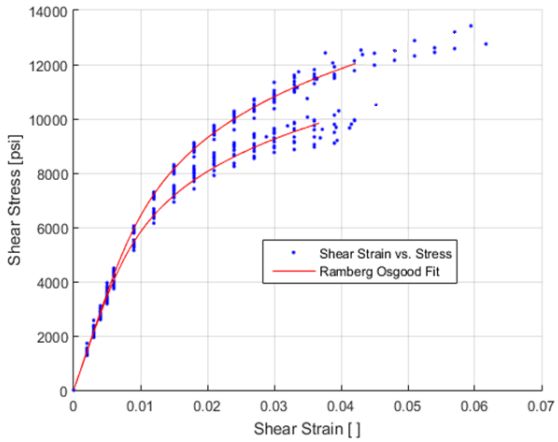

Figure A 3. Shear stress – shear strain data for short beam shear testing. Regression line is plotted up to average value of shear strength

Error! Reference source not found.A-1 provides a summary of the material properties as quantified using the data from the SBS test specimens. The COV values show a modest spread in value. Note that specimens in the 1-3 plane failed under a pure shear failure mode. The specimens in the 1-2 plane failed under mixed-mode failure under the loading nose. The shear

strength *S* noted in this table is the maximum value of shear stress at the failure load and limits the usefulness of the shear stress-strain curve to not exceed that value.

Table A 1. Optimized material properties derived from SBS test.

	Property	SBS	(COV)	SBS	(COV)
	Plane	**1-2**		**1-3**	
Axial Modulus [Msi]	E_T	23.89	(1%)	22.39	(3%)
	E_C	19.13	(3%)	17.51	(2%)
	E_{AVG}	21.51	(2%)	19.95	(2%)
Strength [ksi]	**S**	14.3	(4%)	11.7	(24%)
	Failure Mode	Mixed-Mode		Shear	
Ramberg-Osgood Shear Parameters	**G [Msi]**	0.793	(4%)	0.809	(4%)
	K [ksi]	28.85	(6%)	37.22	(4%)
	N [-]	0.205	(10%)	0.267	(4%)

Note: Shear failure mode in 1-3 plane coupons and mixed-mode failure in 1-2 plane coupons. For mixed mode failures, noted strength S is shear stress at failure load

Verification by Small Plate Twist Tests

The SPT test is the only test method currently available that allows for full accurate characterization of all 3D shear stress-strain constitutive components for laminated composites, well within the nonlinear regime. Results from analysis from SPT test data was compared to SBS test data in Ref. [16] for IM7/8552 with good agreement.

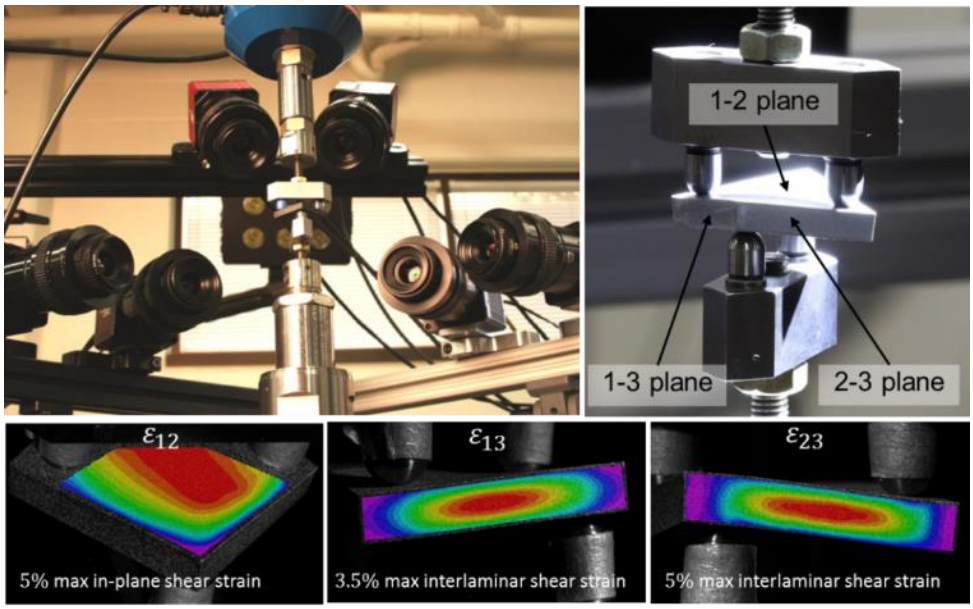

Figure A 4. Three synchronized stereo camera system, test setup, and DIC-measured shear strains in for the Small Plate Twist (SPT) method allowing simultaneous measurement of shear stress-strain properties of composites in all three principal material planes.

Consider the small plate twisting in **Error! Reference source not found.**A-4, which applies a shear strain in each material plane. The three synchronized DIC systems measure this strain in each material plane at the same time, from which the three stress-strain curves are calculated. The analysis method involves an iterative method that updates a high-fidelity Finite Element Model. The specifics may be found in Ref. [11]. As a conclusion, the shear stress-strain curves are compared to that from the SBS test and the comparison is shown in **Error! Reference source not found.**A-5. Note that the agreement as shown confirms that the shear stress-strain adjustment to the SBS data is a necessary part of analysis.

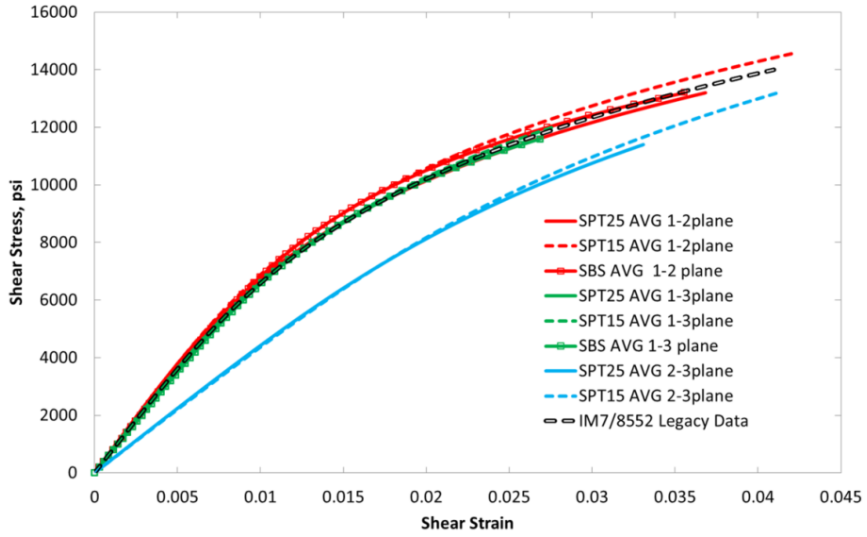

Figure A 5. Average shear nonlinear stress-strain curves in all material principal planes obtained in the SBS method and SPT method using 1.5 inch square (SPT15) and 2.5 inch square (SPT25) specimens for IM7/8552 material.

Measurement of Cohesive Laws

On the Need of Direct Measurement of the Cohesive Laws

Bi-linear and tri-linear cohesive laws are currently used in the embedded and cohesive approach, respectively. These models require strength properties, fracture toughness properties, and fitting parameters characterizing mode mixity typically obtained from ASTM standard tests. DIC-based methods developed at UTA [18] could be used for direct measurement of traction-separation laws without *ad hoc* assumptions on the shape of the cohesive laws for increased accuracy. Measured cohesive laws can be implemented within the user-defined cohesive model developed in CDMat.

Cohesive Zone Modeling (CZM) has been used to model debonding/delamination failure of composites. The constitutive model defined by a traction-separation (cohesive) law which relates interlaminar tractions/stresses to separation displacements (zero-thickness cohesive elements) or interlaminar strains (finite-thickness cohesive elements)

A feasibility study has been completed into the direct measurement of traction-separation cohesive laws in opening (Mode I) and shear (Mode II) dominated ILF [18]. Suitability of DIC and CT based methods to characterize cohesive behavior has been demonstrated. Work started with adhesive bond and continues with solid laminates. Progress on this topic has been presented at the ASC 34th technical conference in Atlanta, September 23-25, [39].

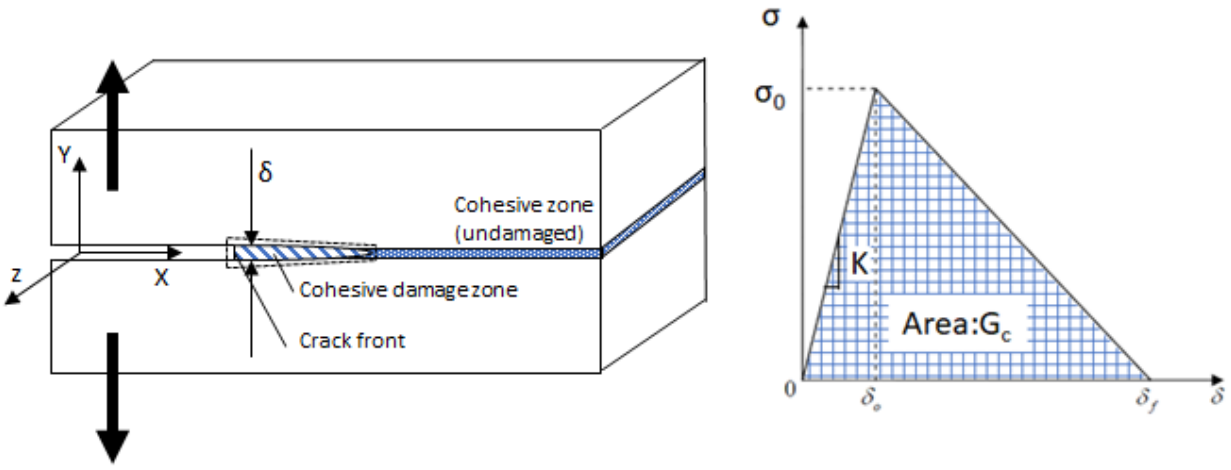

Figure A 6. Schematic of traction-separation relationship

A simple example of a Mode I DCB model for a IM7/8552 uni-tape is used to illustrate some of the challenges in FE-based Cohesive Zone Modeling, including:

- Sensitivity of global response to size of the cohesive mesh
- Sensitivity to *numerical* parameters (penalty stiffness, viscous regularization)
    - DCB mode I load-displacement response is strongly sensitive to the CZM mesh size, viscous regularization parameter and initial cohesive penalty stiffness parameters
- Sensitivity to *physical* parameters (cohesive strength, fracture energy)
    - DCB load-displacement response is strongly sensitive to strength and fracture toughness parameters that characterize the bi-linear Mode I traction-separation law

Results from a simple DCB simulation in **Error! Reference source not found.**A-7 shows that model behavior depends strongly on interface properties. It not only affects the peak load, but also the model stiffness and stability of the model during crack growth. Ironically, a Finite Element Updating method could optimize a triangular traction-separation model to fit the analysis tool to the measurement, without a basis on physics or measurement. Therefore, the direct measurement of cohesive law parameters is needed, if only to verify the shape of the cohesive law.

The DCB, ENF, and TA specimens were created using IM7 8552 tape with Hysol EA 9690-006 film adhesive. The lay-up was chosen to be $[0_{16}/3_2/\text{FilmAdhesive}/\text{-}3_2/0_{16}]_T$. The mismatched plies at the interface prevent fibers mixing through the interface, without sacrificing significant specimen stiffness. This ultimately acts to prevent fiber-bridging. Refer to Figure 4 for specimen geometry. Specimens were pre-cracked and the crack front measured using micro-computed tomography (μCT). Inspiration was drawn from work by Sutton [40]. The mode II cohesive law measured in TA specimens was static only, and these results can be found in Ref. [39]. As the focus is on fatigue, the newly generated ENF results are shown in this report.

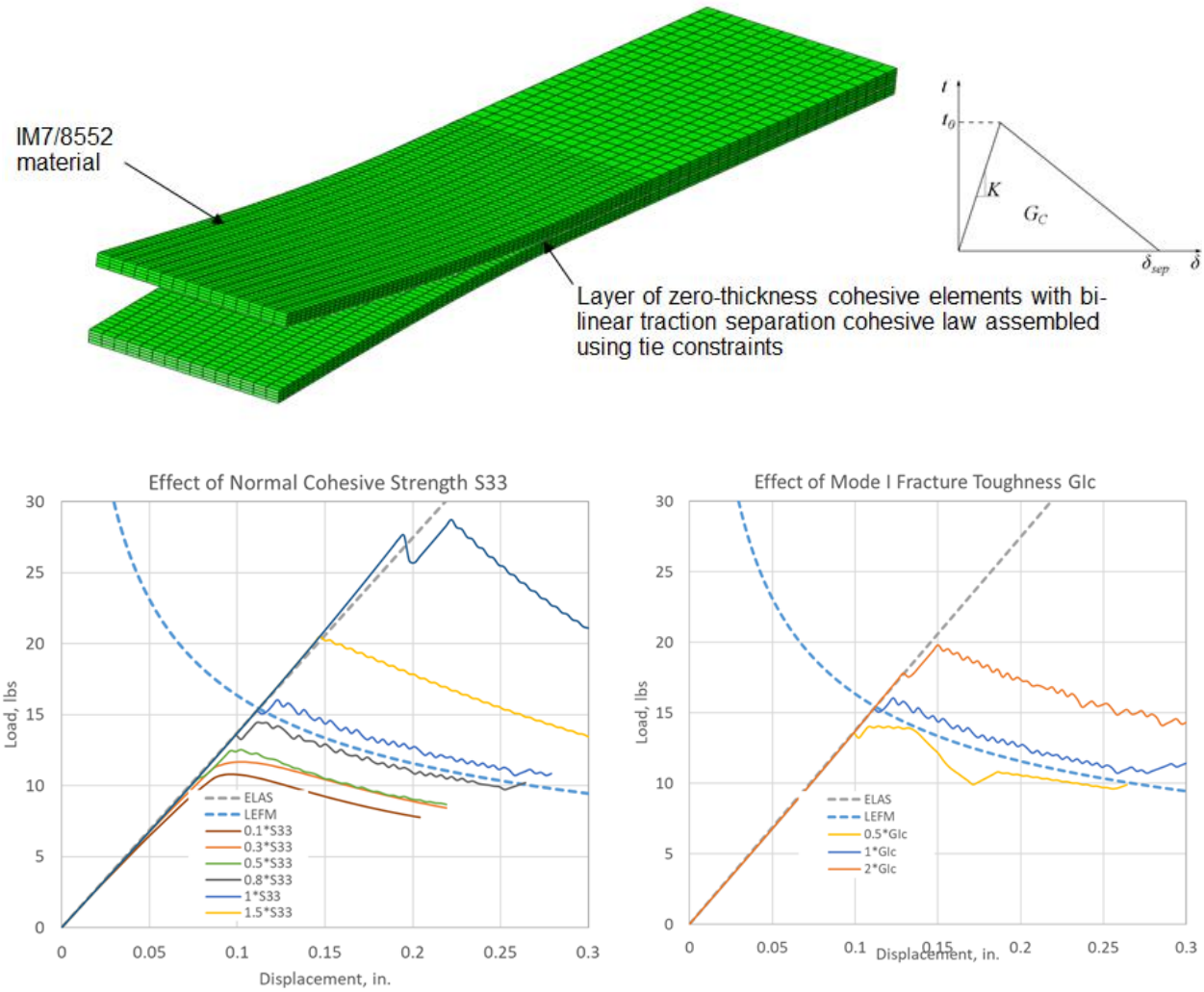

Figure A 7. Simulation of a DCB Model shows high Sensitivity of Global Response to Cohesive Law

Double Cantilever Beam Tests

Specimens were tested in a 2kip capacity Shimadzu electromechanical load frame. All specimens were painted white on both sides. The DIC side was speckled, while the other side was used for optical crack tracking and kept white for visual contrast. All cameras have 16MP resolution. DIC cameras have pixel pitch of 5 µm. DCB tests were performed at 0.02 in/min. Crack tip opening displacements were derived from DIC.

$$\delta = \left|V_{upper} - V_{lower}\right|$$

Measurement nodes are indicated in **Error! Reference source not found.**A-8, 0.5mm above and below crack tip. J-integral calculated using equation:

$$J = \frac{12(Pa_0)^2}{E_d h_d^3} + P(w_1' - w_2')$$

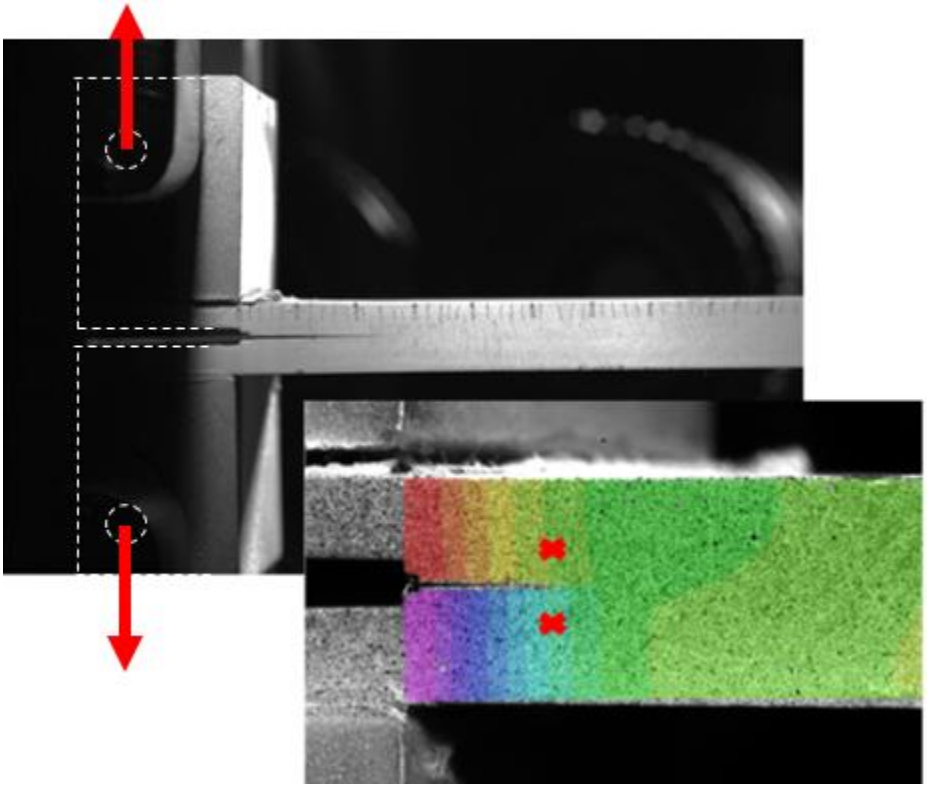

Figure A 8. DCB Data. Crack Tip Location and Vertical Displacement Field. The red crosses indicate where crack tip displacements are measured.

Derivation of the Cohesive Traction-Separation Law in DCB Specimens is shown in **Error! Reference source not found.**A-9. The area under the traction separation curve is by definition equal to the energy until fracture (fracture toughness). Therefore:

$$G = J = \int_0^{\delta_t} \sigma(\delta) d\delta \, \sigma(\delta) = \frac{\partial J}{\partial \delta}$$

$$\sigma(\delta) = \frac{\partial J}{\partial \delta}$$

Indeed, **Error! Reference source not found.** shows a plot of fracture energy against crack tip opening. The first derivative of this plot is the cohesive law as measured. Visible is a near-triangular shape of the cohesive law. By using this traction separation behavior in the FEA model, the simulation matches the experiment very well. It is not optimized to match peak load exactly, but one could slightly alter total fracture toughness to match peak load [18] (see **Error! Reference source not found.**A-10).

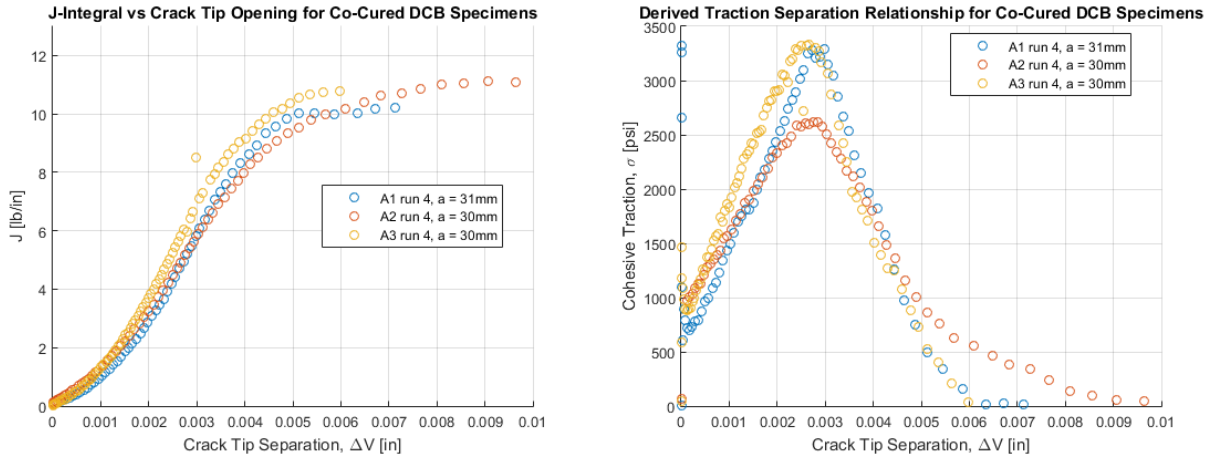

Figure A 9. Left: J-integral vs Crack Tip Separation. Right: Traction-Separation Curves.

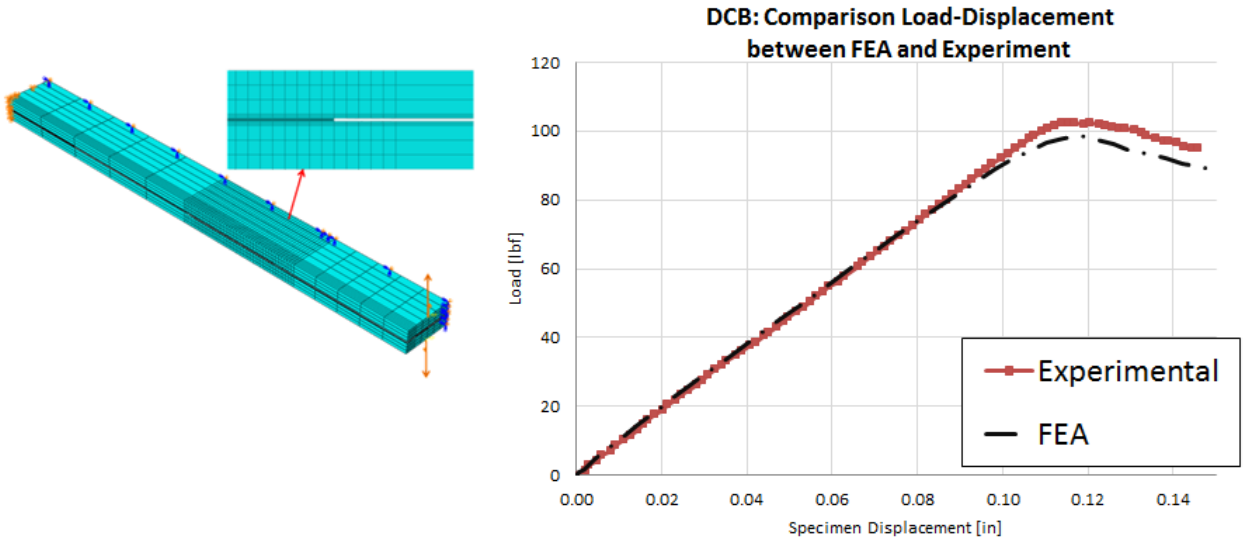

Figure A 10. Comparison FEA-Simulated and Measured Load-Displacement in DCB Specimen

End Notch Flexure Static Tests

The discussion on DCB analysis is pertinent to the ENF analysis method. The development of the methodology to measure the cohesive law is common between mode I and mode II. The test program for mode II will include similar items from the SBS tests as well. The static tests' objective is to verify mode II cohesive traction-separation law. The objective of fatigue testing is to measure and demonstrate the effect of R-ratio (fully reversible) on crack growth under fatigue.

Please refer to **Error! Reference source not found.**A-11 for an illustration of a new custom 3-point bend fixture for ENF specimens. As the ENF specimens are larger than the SBS specimens, they needed their own fixture. The counter-direction or opposite loading noses are held in place by screws. When tightened, these supports create a strong grip on the specimen such that there is no rattling during reversible load fatigue testing.

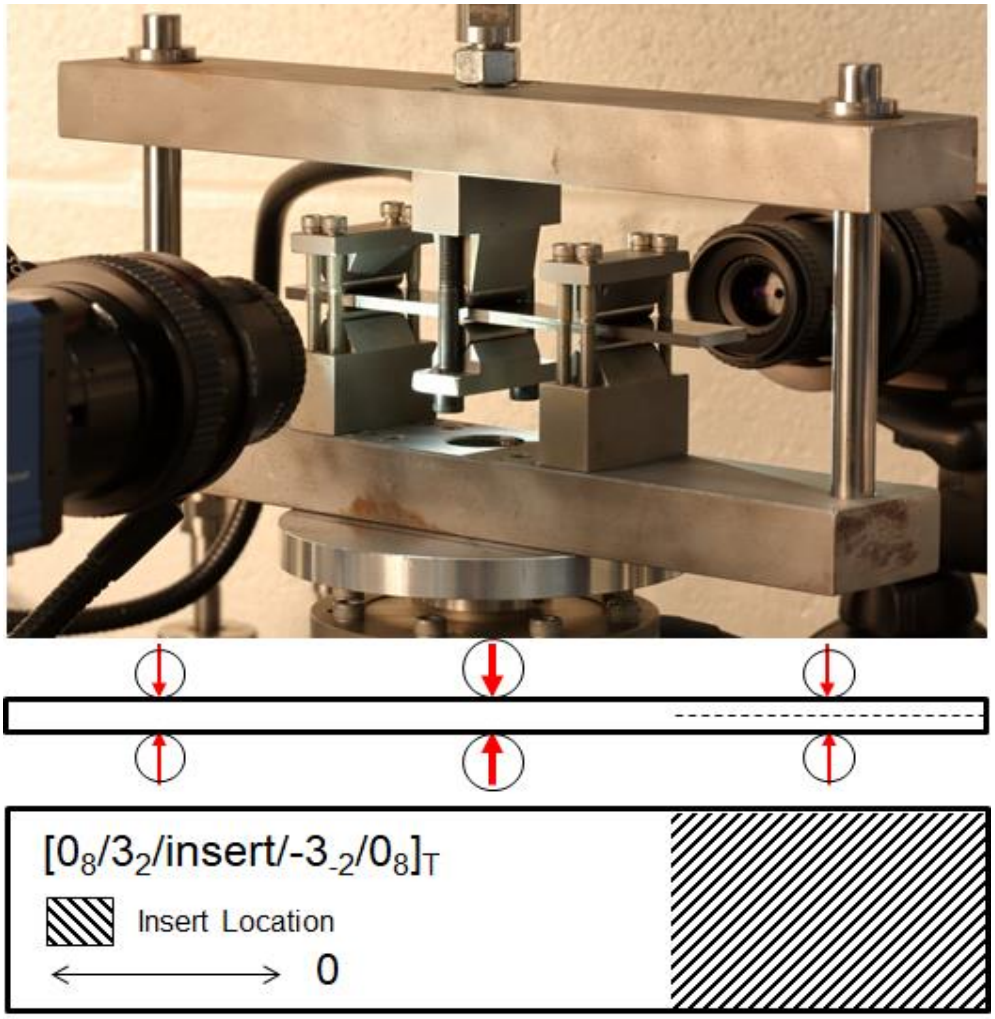

Figure A 11. Custom 3-Point Bend Fixture for Measuring Reversible Fatigue ENF Data

The ENF test strictly adheres to the ASTM D7905 standard [21]. Specimens as manufactured were run after compliance measurements and then tested again in pre-cracked configuration. As with the DCB specimens, the precise location of the crack front is very important, so the crack front is visualized with the µCT facility. A representative CT reconstruction is shown in **Error! Reference source not found.**A-12. The image on the left is a reconstruction of the crack front after mode I pre-cracking. The image on the right is an ENF specimen with roughly straight crack front. The ENF crack front is not always a straight line and is sometimes curved like the DCB crack. Note the measurements are taken from a specific marked line on the specimen which corresponds to an external reference feature. Some of the delamination is not quite visible, as the delamination is not in a perfect 2D plane. Therefore, some of the delamination is just out of the selected plane.

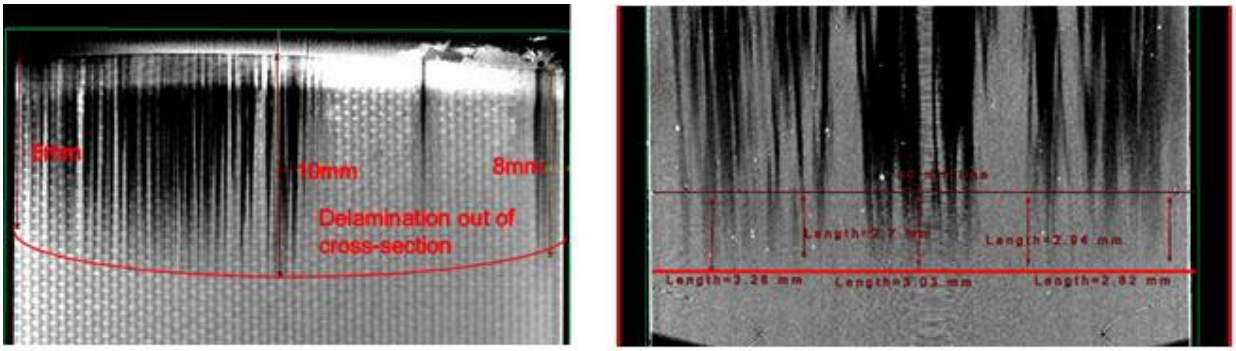

Figure A 12. CT Reconstruction of Pre-Cracked Crack Front in DCB (Left) and ENF (Right) Specimens

Analysis of the ENF specimen with manufactured crack (NPC) and with pre-crack (PC) follows the same procedure using the compliance method. The fracture toughness results are given in **Error! Reference source not found.**A-2. These results are very close to those from O'Brien [30], who used the same test and material to mode II properties. Note that the NPC toughness is much higher than the PC toughness. The difference is partly because the natural crack has a different geometry than the fabricated crack, and partly because the PC specimen has a process zone ahead of the crack front. This difference is very significant for fatigue testing as well.

Table A 2. Static ENF Results, Fracture Toughness in US units.

	GIIC	
SPECIMEN	Non-Precracked	Precracked
EI8S-1	6.50	4.70
EI8S-2	7.06	4.09
EI8S-3	7.41	3.85
Mean	6.99	4.22

COV	6.6%	10.4%

The measurement of the traction-separation law is done with the same method as for the DCB specimens. At the crack tip, the DIC cameras measure local deformations. The top surface of the interface moves opposite to the bottom surface in a sliding motion. This can be measured, and the difference between the two relative motions is the slip. More aptly, the mode II cohesive law measures traction-slip.

The fracture energy is calculated by close-form solution and plotted against crack front slip in **Error! Reference source not found.**A-13. The first derivative is calculated as the cohesive law. Note again, it is somewhat triangular, but with a rounded peak. Marked in this graph is shear strength in 1-2 and 1-3 plane. The data provides evidence that the peak traction stress is close to the interlaminar shear strength. Note this is PC ENF data. The measurements at the NPC crack front measurements have much higher scatter and higher toughness.

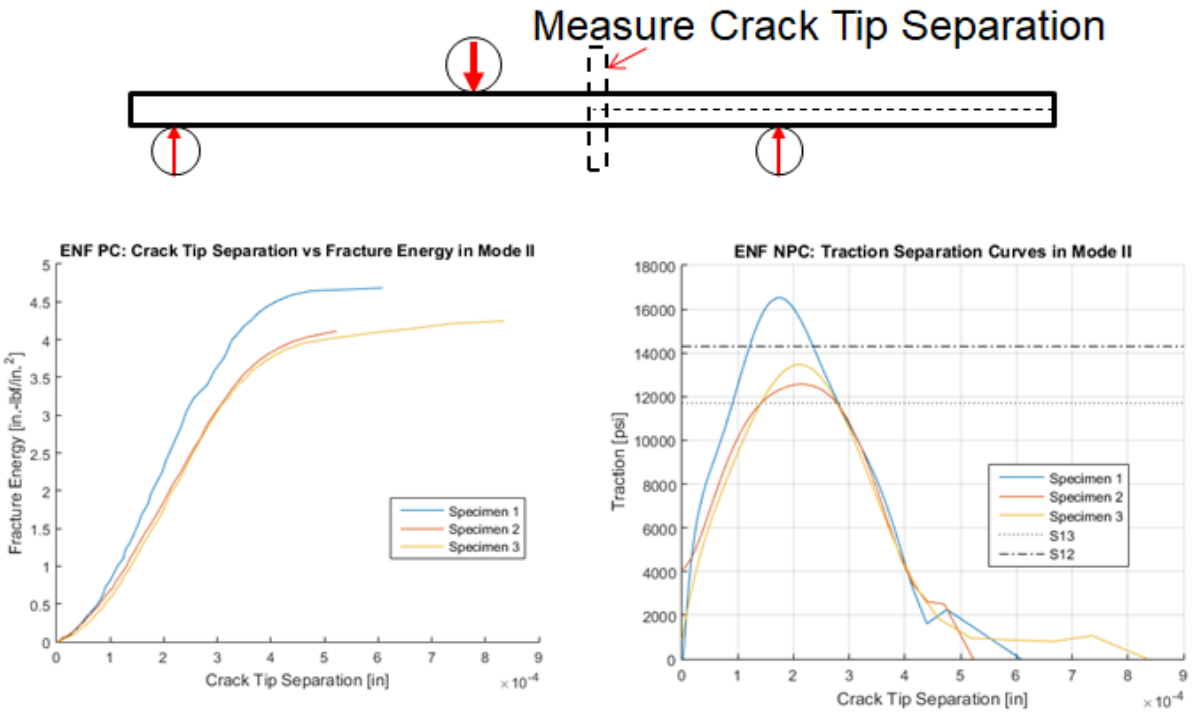

Figure A 13. Left: J-integral vs Crack Tip Separation. Right: Traction-Separation Curves.

Measurement of compression fracture behavior

Open Hole Static Tests

The objective of this experimental work is to determine the input parameters that govern fiber failure progression, specifically fiber-compression ply cracking. This is notably different from the long beam 3-point bend test from before, in which the maximum stress exceeds the material strength and leads to unstable failure. Ply cracking is associated with energy dissipation which may be the driving parameter for modeling this failure.

Key to this work is the capability of performing *in situ* CT, in which specimens may be loaded and scanned at the same time. This is accomplished by integrating an 11kip (50kN) load frame within the CT machine. By applying a tensile (or compressive) load, cracks and delaminations tend to open and reveal failure modes otherwise hidden. This is key to understanding what failure mechanisms are in effects and provides a more accurate estimate of the size of the damage [14].

The first set of specimens tested were the Open Hole Compression (OHC) $[90/0]_{2s}$ laminates per ASTM D6484. Static test OHC specimens exhibit unstable crack growth and sudden failure. Fixture selection is critical; Specimen is likely to buckle and/or fail at the grips. The fixture finally chosen has a small unsupported section to allow the material to fail at the hole. With the failure mode consistently happening in the area of interest, several post-test scans were made (between 80-95% of max load), but no crack development was evident before final failure. As such, no fracture toughness could be established.

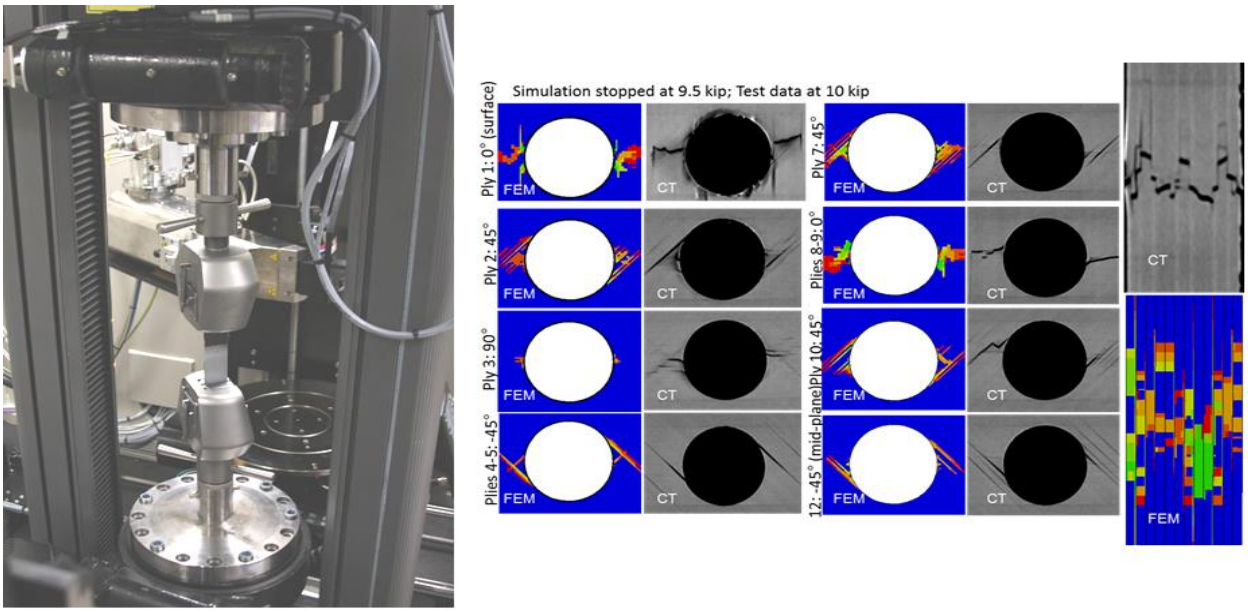

Figure A 14. Integrated Load Frame within the CT Cabinet. In situ CT allows for accurate Damage Characterization [14]

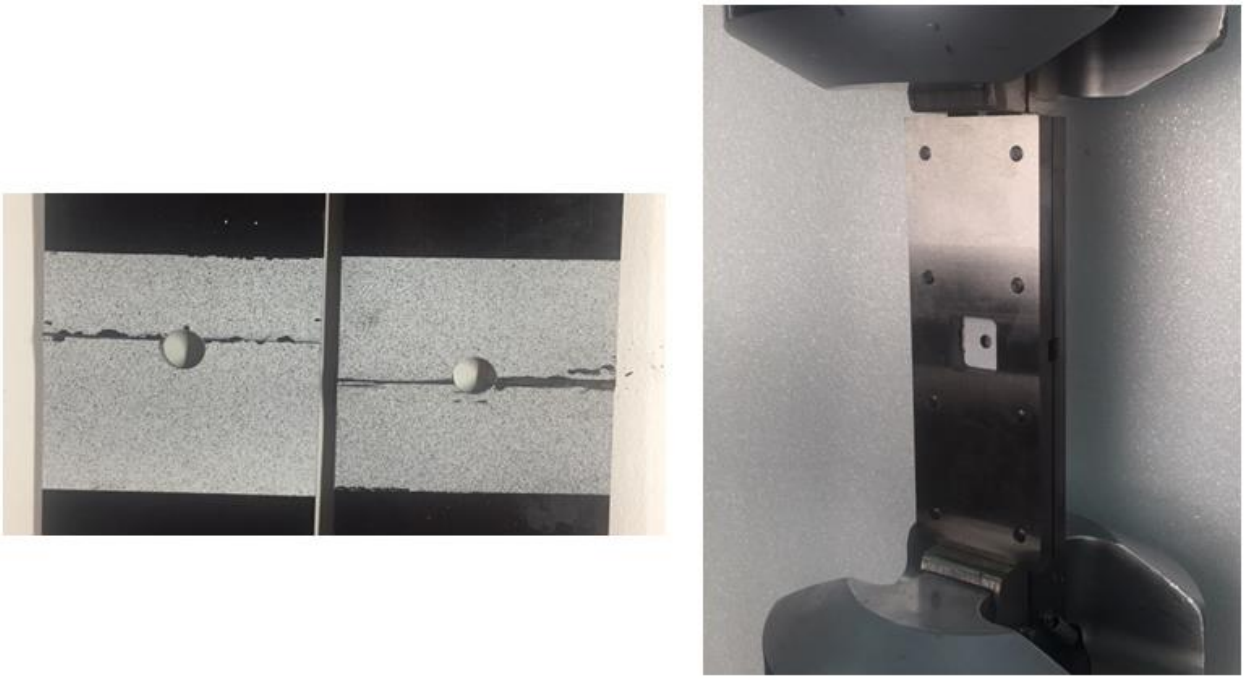

Figure A 15. Static Test Results from OHC tests, $[0/90]_{2S}$

Open Hole Fatigue Tests

The fatigue data for the OHC coupons were run at 10Hz, R = 10. These specimens did not prove to be appropriate to test for fiber compression ply-cracking. When the specimens are tested at 75% static strength, the specimen appears to become a runout. The specimens at 85% and 95% also did not fail under more than 200,000 cycles. The specimen tested near 100% did fail immediately. When scanning the specimen three fatigue specimens, they all exhibited the same failure mode. Fiber splits in the 0 deg reach away from the hole. 90deg compression cracks arise but halt at the fiber splits. This effectively removed (or isolated) the hole from the rest of the specimen, leaving a very high fatigue life, even at 95% max load.

The implication of this steady damage mode, which happens early and stabilizes, is that it was not possible to determine at what load the crack will grow stable. Again, this test is not suitable for measuring fracture toughness or crack growth parameters, due to the layup $[0/90]_{2s}$ chosen.

Static strength = 3900lbf

75% Static Strength	Cracks in 90deg plies are visible, as well as fiber splits in 0deg plies. Damage develops early and is stable. It appears unlikely compression cracks will form. Fatigue life exceeds 3M cycles.
85% Static Strength	Failure mode is identical. Fatigue life exceeds 2M cycles.
95% Static Strength	Failure mode is identical. Fatigue life exceeds 0.2M cycles.

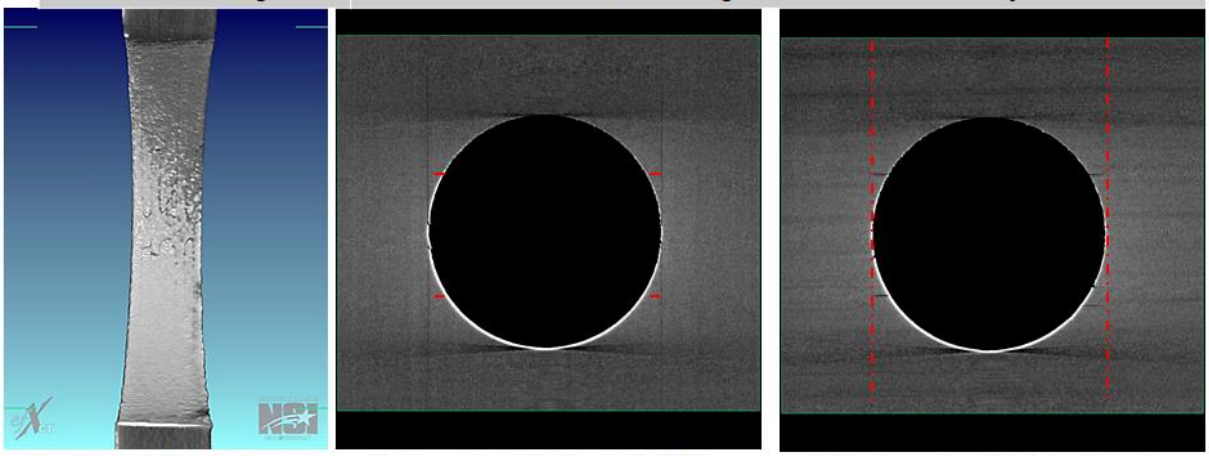

Inside of the hole | 0 deg ply- Vertical Splitting | 90 deg ply - Matrix Cracks

Figure A 16. Failure Modes in OHC Failure for $[0/90]_{2S}$

The second test proposed was a 24-ply $[45/90/-45/0]_{3s}$ laminate to ASTM D6484 specs. The quasi-isotropic laminate has shown to develop some stable cracking under a compressive load. It is possible to derive data-driven models from these reconstructions to calculate the energy going into these cracks [14]. Due to constraints on resources and an abundance of complexity, preference was given to pursue the notched four-point bend test.

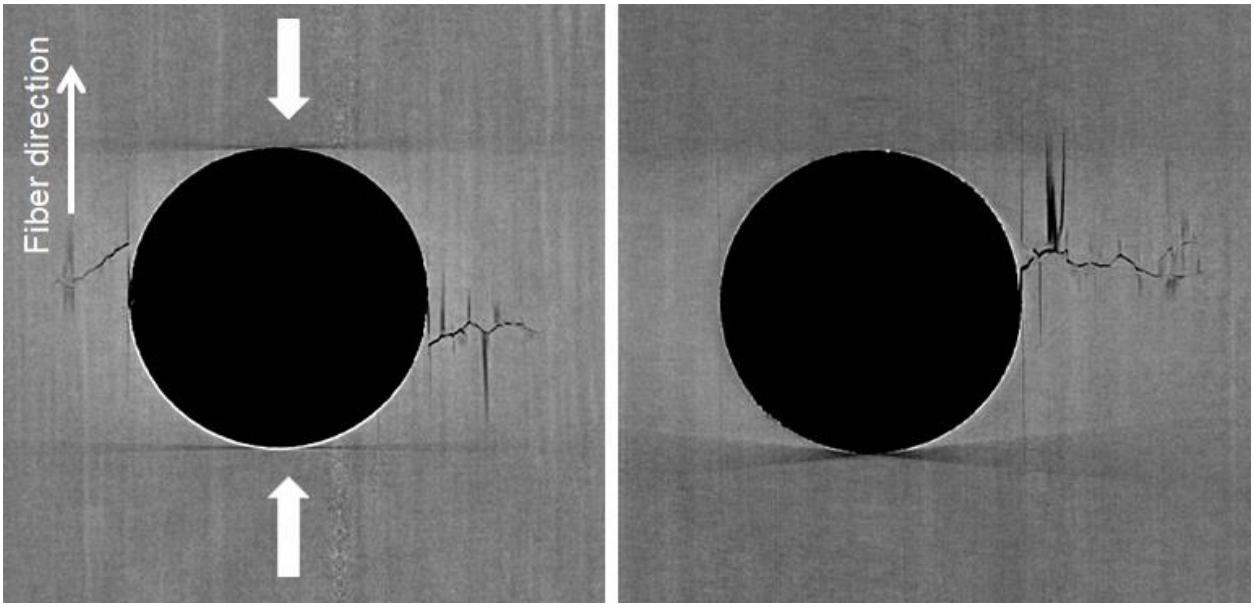

Figure A 17. Failure Modes in OHC Failure for $[0/90]_{2S}$. Left: IM7/PMT-F3GHT, 24 ply CA OHF R10 7,703 lbs peak load, 70K/95K cycles. Right: AFRL CALE 1, 24 ply CA OHF R10 6,722 lbs peak load, 95K cycles

LIST OF SYMBOLS, ABBREVIATIONS, AND ACRONYMS

AFRL	Air Force Research Laboratory
AMSL	Advanced Materials and Structures Lab
ASTM	American Society for Testing and Materials
BSAM	Rx-FEM Software
CDM	Continuum Damage Mechanics
CFV	Critical Failure Volume
CTB	Clamped Tapered Beam
CZM	Cohesive Zone Modeling
DCB	Double Cantilever Beam
DDM	Discrete Damage Modeling
DIC	Digital Image Correlation
DPFF	Deterministic Progressive Fiber Failure
ENF	End Notch Flexure
ERR	Energy Release Rate
G_{Ic}	Mode I Energy Release Rate
G_{IIc}	Mode II Energy Release Rate
HLM	High, Low, Medium loading sequence
ILF	Inter Laminar Fracture
IM7/8552	A type of Carbon Fiber composite
MKL	Math Kernel Library
NLG	Non-linear Geometry
NLS	Non-linear Shear
OHC	Open Hole Compression
OHT	Open Hole Tension
PDA	Progressive Damage Analysis
Rx-FEM	Regularized Extended Finite Element Methodology
RXCC	Composites Branch, Structural Materials Division, Materials and Manufacturing Directorate
SBS	Short Beam Shear
SPT	Small Plate Twist
S-N	Stress vs Cycles to failure
TA	Thick Adherend
V&V	Verification and Validation
X_T	Tensile Strength
3PB	Three-point Bend
4PB	Four-point Bend
µ	Micro
µCT	Micro-X-Ray Computed Tomography
WPAFB	Wright Patterson Air Force Base